OPTIMIZATION OF YIELD FOR CIRCULATING TUMOUR CELL SEPARATION USING INTEGRATED DIELECTROPHORETIC-MAGNETOPHORETIC TECHNIQUE

LOW WAN SHI

FACULTY OF ENGINEERING
UNIVERSITY OF MALAYA
KUALA LUMPUR

2017

OPTIMIZATION OF YIELD FOR CIRCULATING TUMOUR CELL SEPARATION USING INTEGRATED DIELECTROPHORETIC-MAGNETOPHORETIC TECHNIQUE

LOW WAN SHI

DISSERTATION SUBMITTED IN FULFILMENT OF THE REQUIREMENTS FOR THE DEGREE OF MASTER OF ENGINEERING SCIENCE

FACULTY OF ENGINEERING
UNIVERSITY OF MALAYA
KUALA LUMPUR

2017

ABSTRACT

Cell based cancer analysis is an important analytic methods to monitor cancer progress on stages by detecting the density of circulating tumour cells (CTCs) in the blood. Among the existing microfluidic techniques, dielectrophoresis (DEP), which is a label-free detection method, is favoured by researchers. However, because of the high conductivity of blood as well as the rare presence of CTCs, high separation efficiency is difficult to be achieved in most DEP microdevices. Therefore, this study was conducted with the aim of improving the isolation performance of a DEP device, as such by integrating with magnetophoretic (MAP) platform. Several important aspects to be taken into MAP design consideration, such as permanent magnet orientation, magnetic track configuration, fluid flow parameter and separation efficiency, are discussed. The design was examined and validated by numerical simulation using COMSOL Multiphysics v4.4 software, mainly presented in three form: surface plot, line plot and arrow plot. The simulation results showed that the use of single permanent magnet coupled with an inbuilt magnetic track of 250μm significantly strengthens the magnetic field distribution within the proposed MAP stage. Besides, in order to improve dynamic pressure without compromising the uniformity of fluid flow, a wide channel inlet and a tree-like network were employed. When the cell trajectory within a finalized MAP stage is computed with a particle tracing module, a high separation efficiency of RBC is obtained for blood sample corresponded up to a dilution ratio of 1:10. Moreover, a substantial enhancement of CTCs recovery rate was also observed in the simulation when the purposed platform is integrated with a planar DEP microdevice.

ABSTRAK

Analisis kanser berasaskan cell merupakan kaedah analisis yang penting dalam peringkat permantauan kanser dengan mengesan ketumpatan sel-sel tumor beredar (CTC) dalam darah. Di kalangan teknik mikrofluidik yang sedia ada, kaedah pengesanan label bebas seperti dielectrophoresis (DEP) adalah digemari oleh kebanyakan penyelidik. Namun, kekonduksian darah yang tinggi dan ketumpatan CTC yang rendah telah menyebabkan peralatan mikrofluidik yang beraplikasi DEP berkecekapan rendah. Sesungguhnya, haruslah diingatkan bahawa kecekapan permisahan merupakan parameter yang penting dalam penilaian fungsi peralatan pengasingan CTC. Oleh yang demikian, tesis ini adalah bertujuan untuk meningkatkan kecekapan pengasingan DEP dengan mengintegrasikan teknik magnetophoretik (MAP) dengan peranti DEP. Terdapat beberapa aspek penting yang perlu dititikberatkan dalam pertimbangan reka-bentuk MAP, seperti orientasi magnet kekal, tatarajah litar magnet, parameter aliran bendalir dan kecekapan pemisahan peralatan mikrofluidik. Parameter tersebut telah diperiksa dan disahkan oleh simulasi berangka melalui COMSOL Multiphysics v4.4. Keputusan simulasi telah dibentangkan dalam tiga jenis plot: plot permukaan, plot galisan dan plot anak panah. Kajian ini telah menunjukkan bahawa penggunaan magnet kekal tunggal bersertakan dengan trek magnet (250μm) dapat mengukuhkan pengedaran medan magnet dalam peringkat MAP, sepertimana yang dicadangkan. Di samping itu, dalam usaha untuk meningkatkan tekanan dinamik tanpa mengkompromi keseragaman aliran bendalir, channel luas berangkaian pokok telah diaplikasikan dalam reka bentuk saluran mikrofluidik. Apabila trajektori sel dalam peringkat MAP dikaji dengan modul pengesanan zarah, kecekapan pemisahan RBC yang tinggi telah diperolehi daripada sampel darah dengan nisbah pencairan 1: 10. Selain itu, peningkatan kadar pemulihan CTC telah diperhatikan dalam simulasi apabila platform MAP disepadukan dengan peranti DEP.

ACKNOWLEDGEMENT

The accomplishment of this thesis work came on the back of the concerted efforts contributed by a number of people around me. By virtue of their constant companion, I did not have to experience solitary walk in completing my thesis.

First and foremost, I would like to deliver profound acknowledgement to my dedicated dissertation supervisor, Assoc. Prof. Dr. Nahrizul Adib Kadri, for being a great mentor throughout my dissertation writing journey. Hereby, I would like to thank him for lending me a helping hand and sharing many pieces of useful advice during the dissertation process. It was definitely my honour to have benefited from his first-hand experience and knowledge. Under his valuable and relentless guidance, I have deepened my understanding and comprehension toward the crux of matter. The new insight gained has subsequently smoothed the path for my thesis.

By the same token, I would also like to express my sincere gratitude to my beloved family and fellow friends for backing me through thick and thin while I was making gradual headway with my thesis. Their endless encouragement and on-going advocacy served as the pivotal motivational factors in driving me to hold on my steely determination in finishing my dissertation.

In fact, I am truly blessed and fortunate to be granted so many helpful and supportive people along my dissertation journey. Thank you!

TABLE OF CONTENTS

LIST OF FIGURES

LIST OF TABLES

LIST OF SYMBOL AND ABBREVIATIONS

AC	alternating current
cDEP	contactless dielectrophoresis
CK	cytokinetin
CT	computed tomography
CTC	circulating tumour cells
DEP	dielectrophoresis
EDL	electric double layer
EPCAM	epithelial cell adhesion molecule
LOC	labarotory on a chip
MAP	magnetophoresis
MET	mesenchymal-to-epithelial transition
MRI	magnetic resonance imaging
nDEP	negative dielectrophoresis
NiFe	Nickel Ferrite
nMAP	negative magnetophoresis
pDEP	positive dielectrophoresis
pMAP	positive magnetophoresis
RBC	red blood cell
WBC	white blood cell

CHAPTER 1:

INTRODUCTION

1.1 Background

Cancer is a disease of cells which happens when the rapid creation of abnormal cells that uncontrollably grow beyond their usual boundaries and invade adjoining parts of the body. Although this disease which was once rare and was considered as the diseases of western country, new alarming trends in cancer rates have already emerged in economically transitioning countries, such as Malaysia. According to the GLOBOCAN database in 2012, the number of new cancer cases has increased by 70% (37400 cases) as compared to the projection in 2006 (Gaudin & Terrasse, 2013). Of these, more than half of the patients who were diagnosed with cancer eventually die from it. For male and female combined, the five most frequent causes of cancer death in Malaysia were lung (4134 cases), breast (2572 cases), colorectum (2300 cases), cervix uteri (2145 cases) and nasopharynx (2030 cases). These cancers might become predominately a problem for people in this country when Malaysia National Cancer Society reported that the cancer mortality rate could further increase by 40% in the year of 2018 (Lin Loo *et al.*, 2013). Though individual's risk of developing cancer can be substantially reduced by healthy lifestyle, regular health screening is a necessary impetus for detecting tell-tale signs of sickness thus increase the chance of successful treatment. The importance of early screening is augmented when Abdullah *et al.*(2013) reported that the 5-years relative survival rate for patients in Malaysia, whose cancer is treated at an early stage before it has spread is greater than 70%.

In clinical practice, cancer diagnostics are commonly performed through radiological imaging modalities such as traditional radiography (X-ray), magnetic resonance

imaging (MRI), computed tomography (CT), positron emission tomography (PET) or ultrasound (Maryam *et al.*, 2013). These techniques allow visualization of internal body structure, thus enabling physicians to delineate the group of tumour cell colonization. However, there are some drawbacks in these techniques. For instance, the deficiencies of resolution in imaging modalities have precluded them to image small numbers of cancer cells before angiogenic switch, which in turn limit the detection sensitivity (Thiery, 2002; Frangioni, 2008). Furthermore, most of the cases are normally diagnosed at advanced stages where patients often relapsed within 24 months of therapeutic intervention (Husemann *et al.*, 2008; Gerges, Rak, & Jabado, 2010).

The discovery of circulating tumour cell (CTC) as a precursor for the formation of secondary tumours has shed some new light in the clinical prognosis. There is a growing evidence about the presence of a significance correlation between the number of CTCs and patients survival rate (Michaelson *et al.*, 2005; Dalum, Holland, & Terstappen, 2012). Its clinical significance is further augmented when a study conducted by Husemann *et al.* (2008) highlighted that CTCs can be found in patients even before a primary tumour is detected with conventional clinical screening methods. As a result, the enumeration of CTC from blood of a cancer patient can be served as an important biomarker for real-time prognosis thus preclude recurrences and metastatic relapses. Despite this clinical relevance, the detection of CTCs are difficult due to their rare appearance in blood as well as their heterogeneous features (Harouaka, Nisic, & Zheng, 2013; Jin *et al.*, 2014). Therefore, a highly sensitive detection device is needed to help accurately characterize and enumerate CTCs.

In literature, numerous academic and technology platforms for isolation of CTCs have been reported. Among all, the application of mico-total-analysis-system or so-called laboratories-on-a-chip (LOC) for CTCs separation have become an attractive

alternative due to its ability to integrate laboratory functions into miniaturization reaction platform (Jin *et al.*, 2014). This system not only offers a better control of the microenvironment during separation but also facilitates integration and automation for high throughput sample processing (Bhagat *et al.*, 2010; Cima *et al.*, 2013). Notably, the selection of microfluidic sorting system can be divided into two broad categories: the biochemical-enhanced method and the label-free method. A biochemical-enhanced method differentiated CTC from other blood cells based on their immunoaffinity properties (Antolovic *et al.*, 2010). However, as the knowledge of specific and unique antigens that can distinguish CTC from hematopoietic stem cells is limited, this technology may potentially miss CTCs that have undergone a transition to less-expressive or completely lose certain antigens (Gerges, Rak, & Jabado, 2010). Meanwhile, the label-free method isolates cells mainly based on their intrinsic bio-physical properties (Cima *et al.*, 2013). Since CTCs are unmodified by physical separation, cells separated using these techniques are compatible with a wider range of downstream phenotypic and genotypic analyses, including those requiring viable cell. This can be achieved by using the electrokinetic technique such as dielectrophoresis, which will be the main focus in this study.

Generally, dielectrophoresis (DEP) refers to a net force on the dielectric particles in response to a spatially non-uniform electric field. Two types of forces can be exerted in the process: positive DEP (pDEP) and negative DEP (nDEP). pDEP causes particles to be pulled toward locations with maximum electric field, while nDEP pushes them toward locations of minimum electric field. Since cancer cells consist of electrical properties associated with their shapes and surface polarity, DEP is widely used in literature as the label-free CTC isolating method (Khoshmanesh *et al.*, 2009; Leu & Liao, 2012). However, in practice, most of the reported on-chip DEP separation

microfluidic devices require the use of low conductivity medium in order to generate pDEP force to trap cell of interest. Note that blood is a high conductivity medium. Such a condition has caused cells to experience nDEP most of the time and thus influence the separation performance of a DEP platform. For example, the achievable recovery rate for cancer cells in majority of the studies is less than 80%, which is relatively low for clinical application (Huang et *al*., 2012; Fabbri et *al*., 2013). Furthermore, the overloading cell issues within a DEP platform was reported to result in cells to be directed toward the collection port without undergo DEP motion (Gascoyne & Shim, 2014). From a CTC standpoint, such a condition is undesirable as it shows the isolation efficiency of CTCs is independent of their concentration. In this case, tackling these problems has provided continued impetus for my research. To circumvent DEP limitation in CTC isolation, an emerging technique named magnetophoresis will be employed in this study as pre-enrichment stage of DEP separation system. Due to this technique applies force on micro-scale, it is able to integrate seamlessly with microfluidic.

For the proposed device application, the generation of magnetic and electric field gradient in microfluidic channel is a key element to control the efficiency of cell separation. Besides, a uniform velocity flow distribution within the microchannel is required to enhance the continuous cell isolation process. Due to the complexity of separation processes and numerous variables that contribute, computational models will be useful to set up and augment a proposed microfluidic device before performing them in a laboratory setting. In order to ensure the model accurately represents the process, it is crucial to capture a sufficient amount of the system's physics, which includes the flow characteristics and external influences contributing to the separation. By

assembling these parameters in an algorithm, a separation can be tested and calibrated to achieve optimal fractionation of target cells.

In a nutshell, this study by means of numerical simulations using finite element method aims to enhance the CTC separation efficiency within a DEP device, in particular through integrating a magnetophoresis stage as the pre-enrichment stage. A computational model, which primarily focusing on design consideration of MAP stage has been generated with COMSOL Multiphysics v4.4 (COMSOL Inc., Burlington, MA, USA) to assist the design choices and to confirm the analytical results by gaining a further insight on the produced magnetic field phenomena within the proposed microfluidic platform.

1.2 Thesis Objectives

The research objectives of this work are summarised as below:

- To solve cell overloading issue within a DEP device by integrating it with a MAP force.
- To examine various design considerations of the proposed MAP stage which might affect the separation efficiency via computational models.
- To develop a uniform velocity flow within the microfluidic channel that improves cell distribution for integrated MAP and DEP application.
- To validate the feasibility of separating blood cells in a continuous flow environment via Lagrangian-Eulerian numerical approach.
- To outline the best geometrical design of MAP stage which able to facilitate CTC separation for downstream DEP analysis.
- To validate the functionality of the proposed method by performing a complete cell trajectory analysis on the integrated MAP-DEP device, whereby the DEP platform design is adopted from study conducted by Moon et *al.* (2012)

1.3 Thesis Outline

This thesis will include the following topics:

a) A concise literature review on the topics of CTCs; the challenge in CTC detection; the use of AC electrokinetics in cancer cell electrophysiological analyses, particularly DEP; and an introductory note on MAP.

b) A description of the design and development of MAP system, including permanent magnet orientation, the architecture of magnet track, flow parameter analysis within MAP micro-chamber, and separation efficiency vs dilution ratio.

c) A description of work undertaken in COMSOL Multiphysic software to compute the developed system, including magnetic field module, electric field module, Navier-Stoke module, and particle tracing module.

d) A discussion on the development outcome of the proposed MAP platform attained from numerical analysis. The final integration of MAP-DEP separation forces will too be studied.

e) An overall conclusion based on the work undertaken for the project, including a brief summary of future work that needs to be completed.

CHAPTER 2:

LITERATURE REVIEW

2.1 Introduction

This section will cover background information that relates primary aspects of the study which is clinical implication of circulating cancer cells (CTCs) and its challenges, technologies of CTC separation, followed by the concise review of dielectrophoresis (DEP) and magnetophoresis (MAP) techniques. The clinical and technological finding are consolidated from the vast majority of published paper in CTC domain.

2.2 Clinical Implication of CTCs

Circulating tumour cells (CTCs) were first discovered in 1869 by an Australia Physician, Thomas Ashworth, after observing them microscopically in the blood of a man with metastatic cancer. Upon comparing those cells' morphology to tumour cells from different lesions, he surmised that CTCs may shed some light upon the mode of origin of multiple tumours present within the patient (Alix-Panabieres & Pantel, 2014). In 1889, an assistant surgeon, Stephen Paget, had postulated the visionary 'soil and seed' hypothesis of metastasis after analysing 735 case histories of fatal breast cancer. His discovery supported Ashworth's proposal by suggesting that CTCs (the 'seed') were the precursors for the formation of secondary tumours (the 'soil') which flow within the human circulatory system (Paget, 1889). Despite such a discovery, CTC was not a widespread topic in the earlier stage of cancer research due to the absence of technology to conduct further analysis. The topic was not brought up for many years until 1980, when a significant milestone in CTCs was achieved by Hart and Fidler while revisiting Paget's theory (Hart & Fidler, 1980). By injecting the radioactive labelling of melanoma cells into mice capillaries and examining the landing tissue, their study

verified the "seed and soil" concept, thus unravelling the importance of CTCs in promoting metastases. Following this discovery, several studies have been undertaken to decipher the molecular mechanism of CTCs in the formation of metastases. For example, an animal model study conducted by Luzzi et *al.* (1998) in which tumour cells were directly introduced into the mouse systemic circulation, has suggested that CTCs possess clonal capacity to initiate growth in a distant organ. In their study, approximately 2.5% of CTCs was found to give rise to micrometastases while 0.01% of them proliferated into macrometastasis within 13 days of observation. This experimental study appears to be in agreement with the model calculation done by Michaelson *et al.* (2005), which revealed that the probability of the spread of 0.1mm CTC was relatively high such that there's ~1 event of spread for every 500 cells. Furthermore, the clinical data concerning patients with breast cancer and colon cancer has indicated that 20-30% patients were diagnosed with macrometastases at a distant organ (Paguirigan & Beebe, 2009; Loutherback *et al.*, 2012). Note that it has been demonstrated that CTCs harbour a gene-expression signature matching that is observed in the metastatic colony (Antolovic *et al.*, 2010). These findings have thus confirmed the view that the presence of CTCs in the blood is the hallmark of cancer cell invasion and formation of metastases. After years of extensive study, CTCs' role in the event of metastatic cascade is better understood. Its critical pathway from primary tumour to metastatic site is depicted in Figure 2.1 and the overall process can be summarized into four main steps as shown below:

I. The formation of primary tumour originated from the transformation of normal stem cells, undergoing mutation in their growth regulation pathways. The transformation resulted in these mutant cells to be insensitive to both growth factor signals (GFs[7]) and growth-inhibitory signals (e.g. TGFβ). Consequently, masses of tumour cells proliferate uncontrollably, until the dividing tumour cells

surpass the available nutrition and oxygen (Culp *et al.*, 1998; Esmaeilsabzali *et al.*, 2013). At this stage, the expression of angiogenesis-promoting factors (e.g. FGF-2, VEGP, PDGP, and HIF) will be activated to induce blood vessel growth into the tumour (Chow, 2010; Esmaeilsabzali *et al.*, 2013).

II. The primary tumour site normally consists of in-situ cancer, which is referring to the tumour that is formed from the original mutant cells. However, the activation of angiogenesis-promoting factor such as HIF (Chow, 2010), will cause the down-regulation of E-cadherin factor which subsequently reduce the cell-cell adhesion (Pouyssegur, Dayan, & Mazure, 2006). As a result, part of the cancer cells undergo epithelial-to-mesenchymal transition (EMT), such that these cells lose their epithelial phenotype and features a migratory, invasive mesenchymal characteristic. Subsequently, they will break through the basement membrane and enter the bloodstream through intravasation (Radisky, 2005), forming CTCs.

III. CTCs transport via the blood circulation to the distant organ and arrest at its capillary bed. The extravasation process will then be initiated, in which CTCs penetrate through the layer of endothelial cells and invade the host organ. Following this, the cancer cells undergo another phenotype transition, contrary to the EMT process, known as mesenchymal-to-epithelial transition (MET) (Harouaka, Nisic, & Zheng, 2013).

IV. The cancer cells which have settled in the secondary organ recoups its ability to proliferate and colonize in the new environment.

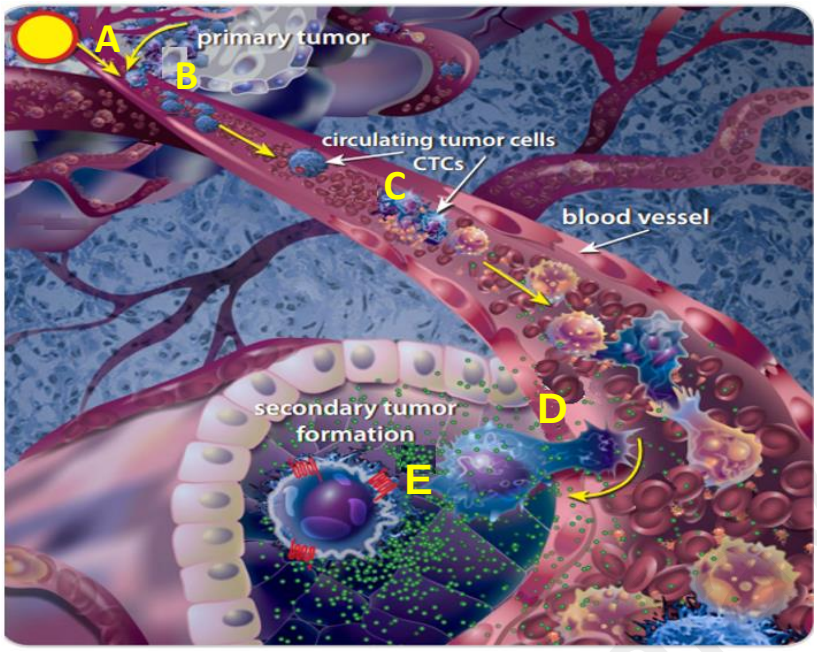

Figure 2.1: Illustration of metastasis process: (A) the formation and growth of tumour within a primary tissue. (B) Cancer cells undergo EMT process and intravasate into the blood stream. (C) The cancer cells shed from primary tumour and travel within the circulation system are termed as CTCs. (D) CTC is captured at the vessel wall and extravasate from blood stream at distant organ to seed new tumour. (E) The cell will perform MET and colonize at the host organ, resulted the formation of secondary tumour site (The Kuhn Lab, 2014).

Based on the simplified framework of metastasis discussed above, it is clearly showed that the persistence of CTCs in circulation is likely to demonstrate the link to the disease CTCs, which may provide further information to support clinical decisions. Notably, there are increasing evidences about the presence of significant correlation between the prognosis value of CTCs enumeration and patient survival rate. This statement is scientifically validated by prospective multicentre studies, focusing on breast (Ying & Wang, 2013), colorectal (Sleijfer *et al.*, 2007; Antolovic *et al.*, 2010; Krawczyk *et al.*, 2013) and prostate cancer (Hart & Fidler, 1980). Despite different methods employed in these studies, all of them have unanimously elucidated that patients with a cut-off of 5 CTCs per 7.5mL of blood would have a poor survival rate. Recently, a similar analysis of prognostic value of CTCs among 90 blood sample from stage I to stage III gastric cancer patient was performed by Wang *et al.* (2014). This

study pointed out that the median progression free survival (PFS) and overall survival rates were twice as high for patient with less than 3 CTCs per 7.5mL of blood; thus, it has confirmed the previous findings. Additionally, this group also presented a significant data which showed patients with elevated CTC density after therapy would have poor survival rate (Wang *et al.*, 2014). The importance of CTCs is further established when a study conducted by Husemann *et al.* (2008) on breast cancer model has proposed that CTCs may precede the outgrowth of primary tumour within the patient, after analysing clinical data from 607 patients. Their theory was clarified when a preclinical research of metatastic tumour in the animal model demonstrated that tumour cells could disseminate systematically from the earliest epithelial genomic alteration before the formation of primary tumour sit (Juratli *et al.*, 2014). In their study, micrometatases was detected at a distant organ (e.g. lung, liver, lymph nodes) in minority of mice (≥20%) at the first carcinoma site at week 9, after inoculation of cancer cells into the mammary glands.

In spite of CTCs clinical significance, simple enumeration of CTCs is inadequate because cancer is a constellation of diseases with various pathologic alterations. Since the ability in analysing proliferation of viable CTCs has still been lacking, it is difficult to assess to CTC information which is the representative of cellular information available in primary tumour (Khoo *et al.*, 2016). To further complicate matters, the recent appreciation of genetic alterations and biomarker expression, for instance KRAS, within tumours means a single biopsy sample is no longer sufficient (Geislinger & Franke, 2014). Henceforth, detecting and analysing these cells on a sample of blood may shed the new light on circumvents clinical need to improve therapeutic efficacy as well as the overall patient survival rate.

2.3. The challenges of CTC detection

In recognition of the potential utility of CTC in research and treatment of cancer, there is a growing interest to develop techniques for enumeration and characterization of CTCs. Despite its high potential in cancer treatment, the detection of CTCs from a whole blood sample remains technically challenging. A key limitation is their rare appearance in blood in relative to the haematological cells such as white blood cells and red blood cells. For instance, the cell density of CTCs are normally ranged from 0~1 cells per millilitre of blood sample, which comprises of $5x10^9$ heterogeneous mixture of diverse blood cells (Husemann *et al.*, 2008). To increase the CTC detection rate from a patient's blood, the American Joint Committee on Cancer (AJCC) has recommended 7.5mL blood sample volume as the optimal, clinically-allowable range (Kin *et al.*, 2013). A blood volume of 7.5mL was chosen based on the reported frequencies of tumour cells in patients with metastatic cancer (Tibbe, Miller, & Terstappen, 2007). Although this parameter is widely employed by most researches, the intrinsic nature of blood such as its labile characteristic in response to the microenvironment (Krawczyk *et al.*, 2013) as well as the presence of coagulation factor within the plasma protein (Sleijfer *et al.*, 2007) has caused the use of a whole blood sample to perform CTC isolation formidably difficult.

Another challenge that needs to be addressed is the large morphological variability among CTCs. Previous size-based microscopic analysis on inter-patient blood samples reported that the size of CTC is generally larger than normal blood cells, which ranges from 8 μm to 52 μm (Bodensteiner, 1989; Cormack, 2001; Coumans *et al.*, 2013). However, this size definition is largely determined based on the location where the CTCs are derived from. For instances, a study conducted on 19 prostate cancer patients by Park *et al.* (2014) has demonstrated a small variation of mean cell size ranging from

7.05 µm to 8.94 µm with a median of 8.04 µm. Meanwhile, CTCs derived from breast cancer was reported to have a higher median cell diameter of 13.1 µm, with cells ranging from 10 µm to 14 µm (Coumans *et al.*, 2013). Apart of size variation, CTCs also exhibit heterogeneity of cell surface markers (Park *et al*., 2014). Mutational analysis of KRAS, BRAF and PIK3CA which were performed on these cells demonstrated inconsistent response to EGFR inhibitors among CTCs from different patients as well as CTCs captured from a single blood draw (Kin *et al.*, 2013; Lustberg *et al.*, 2014). This heterogeneity can disrupt the accuracy of analysis and to detect mutations and differential expression.

Aforesaid, CTC counts are associated with progression of cancer in patient prognosis. Therefore, an effective discrimination of CTCs from blood sample is the key functional requirement of any separation device. The devices which were actively employed for CTC isolation in recent researches will be discussed in the following unit.

2.4. Technologies for CTC separation

Numerous academic and technology platforms have been employed and discussed in literature for CTC separation. Up-to-date, the majority of CTC isolation device are designed for bench-top testing and yet to be implemented for clinical usage. Generally, these methods can be classified into two types: the conventional macroscale analytical system and emerging microfluidic devices.

Macroscale analytical system utilizes large laboratory equipment to analyse millilitres (mL) of cell suspension, whereby separation of cellular constituents within blood is typically achieved by affinity-based method. As different cell lineages differ in their protein surface expressions, this method isolates cells according to the interaction between antibody and antigen (Mocellin *et al.*, 2006). Cell surface markers such as epithelial cell adhesion molecule (EpCAM) and cytokinetin (CK) 8, 18, and 19, were

found to be widely present in the epithelium of CTC but not in normal blood cells (Chen, Li, & Sun, 2012; Dobryzynska, Skryzydlewka, & Figaszewski, 2013). Owing to this distinctive expression of marker protein, both EpCAM and CK are selected as target antigen in most macroscale molecular recognition techniques, including fibre optic array scanning technologies (FAST) (Zhang *et al.*, 2012) , laser scanning cytometry (Zabaglo *et al.*, 2003), and flow cytometry (Orfao *et al.*, 2005; Hu *et al.*, 2010). These three techniques distinguish the presence of CTC from a given blood sample based on fluorescence signalling emitted by antigen-antibody bonding during laser beam illumination. In 2004, an established macroscale system developed using affinity via magnetic approach has been commercialized as CellSearch System (Veridex, Raritan, NJ) (Arya, Lim, & Rahman, 2013). To date, it is the sole medical device that received the United States' Food and Drug Administration (FDA) approval for prognostic evaluation and monitoring the therapeutic response in patients with metastatic breast, prostate or colon cancer. This approach uses ferro-fluids coated with epithelial cell-specific EpCAM and CK antibodies to immunomagnetically detect CTCs(Miller, Doyle, & Terstappen, 2010).

Although both CellSearch and the molecular recognition techniques mentioned above are able to isolate CTC efficiently with a high recovery rate (>80%), several shortcomings were discussed in other papers (Arya, Lim, & Rahman, 2013). Notably, the existing macroscale analytical techniques such as FAST, flow cytometry and laser scanning cytometry require long processing time and laborious sample preparations (Orfao *et al.*, 2005; Hu *et al.*, 2010). As a result, it prevents the patient and physician to receive quick results. Furthermore, extensive study conducted by Hong and Zu (2013) has showed that cell contamination as well as loss of cell viability commonly occur during CTC detection process with the macroscale analytical system. Consequently, the more aggressive cancer cells are less likely to be captured and identified using these

techniques. Besides, a recent study done by Lustberg *et al.* (2014) on CTC biochemical feature has revealed that EpCAM is not present in all tumours. There was evidence for downregulation of EpCAM with higher cancer progression (Kirby *et al.*, 2012; Hong & Zu, 2013), and different correlation between marker protein expression with tumour types (Hoeppener, Swennenhuis, & Terstappen, 2012). Subsequently, the reliability of affinity-based technique using EpCAM is hotly debated as up to a 40% discordance rate was reported in 2012 among laboratories using CellSearch, which is of concern (Balic, 2013). Moreover, the use of affinity capture method in macroscale analytical system often results in permanent attachment of target cells to marker protein on CTC, which limits downstream options for the extraction and subsequent characterization of CTC (Lustberg *et al.*, 2014).

To overcome the limitations imposed by the macroscale system, vigorous efforts have been undertaken in the past decade to develop more robust laboratory tests. The technology advancements at the turn of the millennium have given birth to microfluidic-based analysing platforms, also referred as Lab-on-a-Chip (LOC) or micro-total analysis systems (μTAS). This miniaturization reaction platform carries out laboratory work on a scale of one-tenth to one-thousandth of the macroscale analytical device, thus shortens the sample analysis time (Jin *et al.*, 2014). Furthermore, microfluidic devices have a scalable architecture for different biological cells, where it provides a programmable platform that enables manipulation of bioparticles at a microscale level (Gerges, Rak, & Jabado, 2010). This feature is especially important for CTC characterization considering the rare presence of CTCs within the blood, as mentioned previously. It allows more efficient and accurate isolation of cancer cells within a controlled time and selected flow rate. Leveraging these advantages, the application of microfluidic device based technologies for CTC detection has received a growing number of interest among researchers.

A large panel of microfluidic approaches for CTC isolation that are independent of cell surface antigens have been developed on the basis of its physical properties. Majority of these devices exploit the differences of cell's size, electricity and deformability between CTC and normal blood cells to conduct the isolation. Examples of these physical-based microfluidic technique include microfiltration (Zheng *et al.*, 2011; Coumans *et al.*, 2013), hydrodynamic sorting (Sun *et al.*, 2013; Warkiani *et al.*, 2014) and dielectrophoresis (Moon *et al.*, 2011; Huang *et al.*, 2012). Microfiltration is a technique of flowing a cell sample through an array of micro-scale constrictions in order to capture target cells based on size, or a combination of size and cell deformability. A hydrodynamic microfluidic sorter isolates cells by distributing them into specific stream lines which superpose with the particle's velocity due to its size and density. Meanwhile, dielectrophoretic sorters separate cells by subjecting them under a non-uniform electric field. Unlike the immunoaffinity method where epithelial antigens are needed to mediate the intercellular adhesion, the physical-based isolation techniques mentioned above are label-free. Therefore, interference such as sample contamination due to the tagging molecules can be avoided and a high cell viability rate (>90%) can be achieved (Jin *et al.*, 2014). Cells isolated using these methods are thus compatible with a wider range of downstream phenotypic and genotypic analyses, including those requiring viable cells.

Despite their popularity in CTC research, there are some limitations remaining for these devices to be fully employed in point-of-care application. As alluded in the previous section, CTC has high degree of heterogeneity in cell size. A mathematical model by Marrinucci *et al*. (2007) has demonstrated that CTCs could consist of complex histological organization with connective tissue and tumour-infiltrating immune cells. This study is in agreement with a histological study conducted by Park *et al*. (2014) which shows that a significant overlap in size of certain CTCs with

leukocytes has resulted in leukocyte contamination in most size-based microfluidic separation methods, particularly of microfiltration and hydrodynamic cell sorters. In addition, as the effectiveness of these size-based microfluidic devices are controlled by tailored gap dimensions, their separation mechanisms are not universal and will require variation in design when the target sample changes.

In contrast to the size-based microfluidic separation, dielectrophoresis utilises an external electric field source to manipulate the CTC separation within the microchannel. This technique allows the reconfiguration of an electric field externally to obtain accurate isolation results in accordance to cell phenotypes, thereby promotes flexible control of the microenvironment for a wide range of cells. Furthermore, several studies discover that most CTC exhibit similar responses when they are subjected under an electrical field in spite of their heterogeneity (Moon *et al*., 2011; Shim *et al*., 2013). Consequently, it has been surmised that the DEP can be used to detect CTCs of different cancer types. This technique would thus be employed to develop a microfluidic platform for CTC isolation in the study. A DEP principle will be discussed in detail in the next section.

2.5 Dielectrophoresis (DEP)

The concept of DEP was first described by Pohl in 1951 as the phenomenon of particle motion under a non-uniform electrical field. His study highlighted that physical parameters such as electric field strength and particle dielectric properties are essential for DEP response. A review of the electrical properties of tissues and cell suspensions by Schwan (1957) have provided a fundamental statement that the cell membrane's selective permeability is controlled by electrical charges. This discovery has prompted Pohl and Hawk (1966) to apply selective DEP on yeast cell suspension. Their study had elucidated that with a proper combination of frequency and solvent conductivity,

different cell types will experience a counter-motion in response to DEP field. An extended study conducted by this group in 1971 has concluded that DEP could efficiently detect changes in membrane conductivity resulting from physiological changes (Pohl & Crane, 1971). Consequently, these methods are honed as important tools for characterize the dielectric properties and to discriminate between different cell types. With the rapid advancement of technology, DEP has undergone significant development and is today applied on microscale-chip to manipulate and separate a variety of non-biological particles and biological cells. To date, a remarkable amount of DEP applications are reportedly transferred from the research bench to clinical studies, in which the DEP is used to characterise cells such as platelets (Pommer *et al.*, 2008; Gagnon, 2011), leukocyctes (Wang *et al.*, 2000), erythrocytes (Gagnon, 2011) and cancer cells , by measuring the function of cell collection vs. frequency.

In DEP-based experiments relating to CTC, consistent dielectric differences have been reported between cancer cells and normal blood cells. An electrorotation measurement conducted by Becker *et al.* (1995) had uncovered the differences of dielectric properties between the metastatic human breast cancer cell lines MDA231, erythrocytes and T lymphocytes. Their result showed that MDA241 has a higher membrane capacitance (26±4.2 mF/m^2) in contrast to both T lymphocytes (11±4.2 mF/m^2) and erythrocytes (9±0.8 mF/m^2) (Becker *et al.*, 1995). Although this finding was published decades ago, the obtained result is in agreement with the experiment conducted by Shim *et al.* (2011). This group concluded that the capacitance of cancer cells are significantly larger than those of blood cells after studying the electrical capacitance of seven subtypes of blood cells and nine cancer cells lines (Shim, Gascoyne, Noshari, & Hale, 2011). The reason behind these quantitative information of dielectric properties of CTC is explained in paper published by Dobrzynska *et al.* (2013). Their study discovered the presence of a lipid peroxidation product in cancer

cells during tumorigenesis has resulted in changes in the intracellular cell signalling, thereby altering the cell membrane structures as well as the membrane charges (Dobrzynska, Skrzydlewska, & Figaszewski, 2013). Based on the outcome of these researches, it is clearly informed that each cancer cell line has a specific electrical signature whereby DEP could be utilized to isolate CTCs from blood sample.

Leveraging the dissimilarities of electrical properties between CTCs and blood cells, few bench-top DEP devices have been successfully used to detect variables of cancer cells, including oral (Broche *et al.*, 2007; Mulhall *et al.*, 2011) , colon (Fabbri *et al.*, 2013), breast (Moon *et al.*, 2011), lung (Chen *et al.*, 2012) and prostate cancer cells (Park *et al.*, 2013) . In most cases, these DEP devices used for CTC isolation are operating based on two types of sample flow configuration, such that (i) a variant of sample-batch-flow-fractionation and (ii) a continuous flow.

For a sample-batch-flow-fractionation DEP device, the number of cells to be processed in a given run of DEP device is restrained to help enhancing the CTCs recovery rate. The cells will be left to settle for a few minutes inside the DEP microchamber before the electrode are energized to initiate the isolation process. Using this technique, Shim *et al*. (2013) have demonstrated their DEP device ability to capture more than 70% of NCI-60 cancer cells from a spiked blood sample. Because the loading capacity of this method is limited to a few million cells per run, many batches are required to achieve CTC analysis of 1mL blood. Consequently, a timescale of 2 to 4 hours are needed to process up to 10^8 peripheral blood mononuclear cells. To enhance the number of DEP-analysed cell per second, this group has later suggested the use of a relatively large DEP chamber of 25mm wide and 300mm long. Comparing to previous batch-mode DEP device for CTC detection, a higher throughput that exceeds 10^6 cells/min was achieved when this architecture was experimented with 1mL diluted

clinical blood specimens. Despite the improvement, a study conducted by Pamme (2014) showed that the separation conditions for batch-mode-DEP-operation are not ideal for CTC isolation from a blood sample. It is because an optimal condition for separation such as flow speed can only be found after a sample injection is repeated for several times. More often than not, this method can be quite cumbersome as the cell recovery is needed to be evaluated at the end of each separation batch (Pamme, 2014). Therefore, this type of DEP operation is primarily analytical in nature and is not suited to procedures which requiring the removal of cells from a large sample volume.

A continuous flow DEP microfluidic cell-sorting device, on the other hand, provides an alternative to process any volume of sample. In this method, a cell suspension is continuously introduced into the DEP separation chamber, whereby the sample will be sorted into different stream and subsequently leaves the channel at different positions after the separation is performed. Owning to this configuration, the DEP effect on CTCs cell isolation can be observed in real time thus enabled on-line feedback, as such the fluid flow and induced DEP force can be changed independently from each other (Qian *et al.*, 2014). Consequently, this technique has widely been employed in recent year as the method to isolate cancer cell from a particular cell populations. For example, in 2011, a research group based at Yonsei University, South Korea, has developed a continuous DEP-based CTC detection technique which can accommodate flow rate of 0.6mL/h to 1.8mL/h within a specially designed chamber. A voltage of $10V_{pp}$ with frequency of 2MHz was applied on the slanted microelectrode to generate DEP force for separating human breast cancer cells (MCF-7) from a spiked blood cell sample. The obtained recovery rate for MCF-7, RBC and WBC are 75.18%, 99.24% and 94.23%, respectively (Moon *et al.*, 2011). Another study conducted by Huang *et al.* (2012) has developed a continuous flow DEP-based technology known as contactless DEP (cDEP) which capable of manipulating cells without direct contact between the electrodes and

the sample.This cDEP capitalized on the sensitivity of traditional DEP, while eliminating challenges such as bubble formation, electrode delamination, expensive fabrication, and electrode sample contamination. The experimental results has indicated that the cervical carcinoma cells was isolated from the concentrated RBC with a recovery rate of 64.5%.

Although the previously discussed DEP techniques showed a successful CTCs isolation outcome, there are some limitations reported across multiple study. First and foremost, for an on-chip DEP microfluidic device, the reported separation efficiency is relatively low, such that the achievable recovery rate for cancer cells is less than 80%. Such a scenario is mainly caused by the high conductivity of a blood (Vykoukal, Gascoyne, & Vykoukal, 2009). This distinctive blood feature has resulted in cells to experience negative DEP most of the time, and therefore influenced separation performance of a DEP device (e.g. difficult to obtain a high purity output). Additionally, the high conductivity of a blood suspension is reported to cause significant heating within a DEP device (Qian *et al*., 2014). This may lead to undesirable lysing of cells . To circumvent this issue, few studies has reported to suspend the blood cells in a low osmolality buffer (also known as hypotonic diluent) prior to the DEP processing. Though this technique is widely employed to obtain optimal recovery for DEP isolation of a blood sample, the viability measurements in these sample are reported to be low, as such less than 70% (Kuczenski, Chang, & Revzin, 2011). Such a condition is caused by the cytoplasmic ions leakage when cells are placed in a low conductivity medium (Miyakoshi, 2005). Furthermore, a spectroscopic study conducted by Cheng *et al*. (2007) has found lysis in both RBC and WBC to begin as early as 3s after a blood sample was mixed with low conductivity medium.

As first noted by Gascoyne *et al*. (2007), the integration of multiple separation forces enable a microfluidic device to precisely control the cell separation dynamics, and thus give rise to new modalities of separation. In order to improve CTC capture efficiency as well as to achieve the isolation of cell types having small differences in their DEP crossover frequencies, integration of DEP with other cell separation techniques has been attempted. Up-to-date, there is only one method, known as hydrodynamic separation technique, which is reported to be integrated with a DEP-based microfluidic chip for CTCs' isolation. This technique is pioneered by a group of scientists from University of Texas MD Anderson Cancer Centre's Laboratory Diagnostic Microsystems, whereby they have combined DEP force with field-flow fractionation to create DEP-FFF (Shim *et al*., 2011). In this approach, a diluted mixed cell population which is continuously flowing into the chamber, will be subjected to a combination of upward pushing DEP force, downward-pulling sedimentation force and hydrodynamic force. A detailed illustration of DEP-FFF is depicted in Figure 2.2. As shown, the cells will be repelled to a height which is equilibrium to the DEP force over a planar interdigitated microelectrode array due to the differences in their electric properties. Since the flow generated within the microfluidic channel was laminar and has a parabolic velocity profile, cells at different vertical position would have exposed to different velocity. The separation of cells was achieved through the different velocities of particles in the parabolic velocity in the chamber (Abdul Razak *et al.*, 2013). As such, the non-targeted cell at the vertical middle of channel were carried from separation chamber toward a waste outlet by a high velocity profile of eluate stream. Meanwhile, the target cells which were close to the bottom will slowly flow into an outlet located at the chamber floor. Due to the reported high separation efficiency (~85%) in practical applications, this device has created an advancement from bench top preclinical trial toward clinical trial. In 2010, this technique has been commercialized as clinical diagnostic device,

namely ApoStream system to isolate live CTCs from epithelial and non-epithelial malignancies (Tan, 2013). When the preliminary performance of ApoStream was tested using human blood sample spiked with breast cancer cell line (MDA-MB-231), Gupta *et al*. (2012) has demonstrated a recovery efficiency of 86.6% . Therefore, it can be deduced that the development of DEP-FFF has enhanced the cell discriminating ability and throughput in contrast to a-standalone-DEP stage. Recently, this device is reported to isolate CTCs for assessing the pharmacodynamics effects of anticancer on DNA damage in solid tumours (Balasubramanian *et al.*, 2014) .

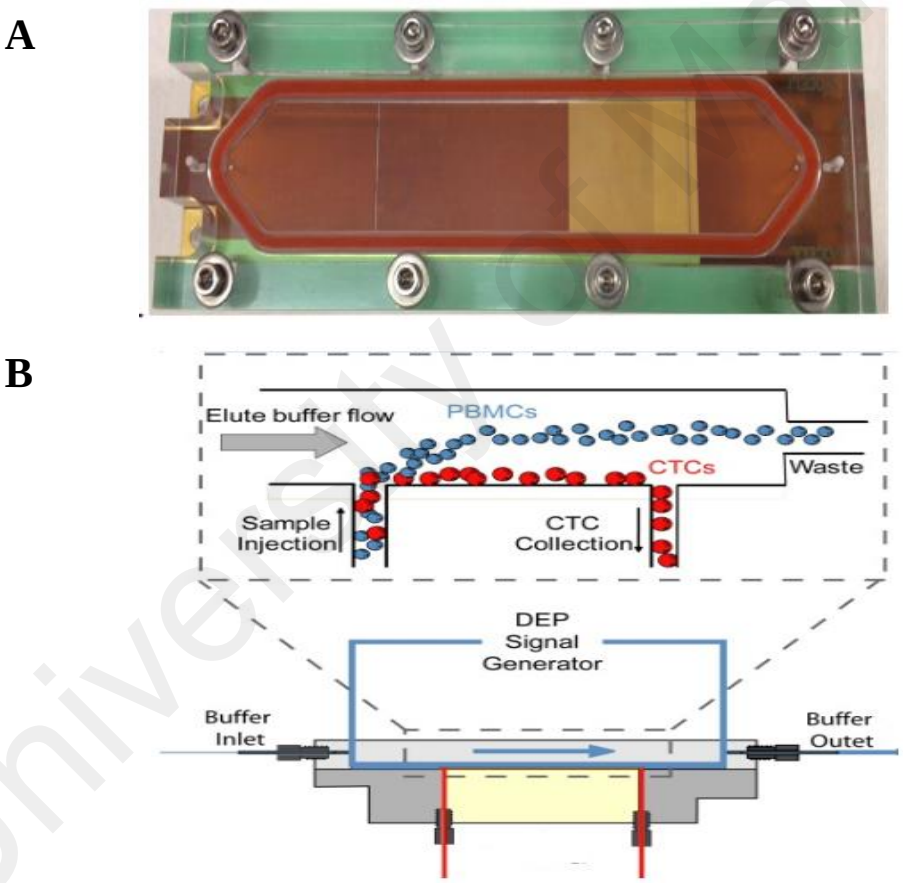

Figure 2.2: (A) Photo of ApoStream DEP microchip. (B) Schematic diagram of ApoStream device(Gupta *et al.*, 2012). The blood sample is injected with a high precision syringe pump at a low flow rate into the bottom of the flow chamber to reduce the cell levitation as well as to ensure them stay within effective DEP field. Under the DEP field, the DEP forces will attract cancer cells toward the electrodes on the chamber floors and vice versa to the other cells. Cancer cells will withdraw through the collection port which is located close to the chamber floor. Meanwhile, other blood cells will be levitated and flow into the waste container via a second outlet port.

Despite enhanced separation, there are numerous problems to be solved in this integration platform. The latest study conducted at BEACON (a Phase 3 open-label and multicenter study of Etirinotecan pegol versus treatment of physician's choice (TPC) in patients with metastatic breast cancer) has indicated an existence of excessive cell loading in DEP-FFF device (Wang *et al*, 2013). Such a condition can result in dipole-dipole interaction between cells, thus cause the clustering of cells and the entrapment of both similar and dissimilar cell types. Consequently, it will lead to reductions in cell discrimination and a device's separation efficiency. For example, on a DEP-FFF device which consisted of arrays of 50μm wide interdigitated electrodes, the isolation efficiency was 85% at a loading density of 500 peripheral blood cells per mm^2 but only 20% at a loading density of 10000 peripheral blood cells per mm^2 (Abonnenc *et al.*, 2009). However, it should be noted that the number of target CTCs in clinical specimens is very small. The overloading of cell within the DEP chamber might cause interactions between CTCs does not have any impact on device performance. From a CTC application standpoint, such a condition is undesirable as it shows the isolation efficiency of CTCs is independent of its concentration. Though few studies suggested that the overloading cell problem can be solved by increasing a blood dilution ratio, Pommer *et al.* (2008) and Liao *et al.* (2013) have reported that the actual separation efficiency to be dropped for approximately 20% if the dilution ratio of 1:10 of whole blood sample was conducted. Furthermore, another study conducted by Takaori in 1966 has indicated that an excessive dilution will cause a progressive decrease in blood sample pH. Since blood cells respond quickly to the changes in their environment, their biological characteristics might change in regard to the reduction of pH.

To circumvent these issues, integration of DEP with other cell separation force should be attempted. The design will focus on decreasing an excessive cell loading within a DEP separation chamber, as well as to enhance a recovery rate and throughput.

Notably, in a whole blood sample, 98% of human blood cells are red blood cells (RBCs), whose cell density is around $5x10^6$ cells/μL (Lynch, 1990). Besides, study conducted by a group from LifeScan Scotland has shown that electrical conductivity of the blood medium is highly dependent on the haematocrit level within blood (Gassner *et al.*, 2009). As such, the blood medium conductivity will be reduced with the decreased of haematocrit level. Therefore, a removal of RBCs from whole blood samples in the early stage would greatly help downstream sub-classification of target cells as well as eliminate cell overloading issues. Interestingly, various studies have reported RBCs exhibit a distinctive magnetic response under magnetic field in contrast to both WBC and CTC. Owning to this feature, a technique which employ non-uniform magnetic field in cell separation, namely magnetophoresis (MAP) is proposed as an alternative separation technique in this cooperative platform.

2.5.1 Theory

As previously mentioned, a DEP force is generated when a dielectric particle is placed in a conductive medium, which a non-uniform electric field is applied. Depending on the alignment of induced dipole moments, particles may experience a force which cause them to either move toward or away from the electric gradient. It is noted that the magnitude and charge orientation of induced dipole is affected by the difference of relative polarizability between medium and particle (Khoshmanesh *et al.*, 2009). Such condition can be explained through a series of DEP equations.

To begin with, a dipole will be formed when a particle is subjected to an electric field, due to the accumulation of charges on both sides of the interface between the suspending medium and the particle. An illustration of an electric dipole within a conductive medium is showed in Figure 2.3. The electrostatic potential which is imposed on these electric dipole can be written as (Jones, 2003):

$$\Phi_{dipole} = \frac{\vec{p} \cdot \vec{r}}{4\pi\varepsilon_o\varepsilon_m r^3} \quad \textbf{2-1}$$

where $\vec{p}$ depicts vector moment of an electric dipole, $\vec{r}$ refers to the radial vector distance measured from the dipole's centre, r is the modulus of $\vec{r}$, ε_m denotes the permittivity of dielectric fluid and ε_o is the free space permittivity. Notably, in a constant electric field, equal force is present on charges on both side of the dipole. Thus, there would be no net force since the force on the positive charge is cancelled by that on negative charge. On contrary, in a non-homogenous electric, difference forces are found to be induced on charges on both side of the dipole (Payen, 2003). Its net force can be calculated as follows:

$$\vec{F} = q\vec{E}_+ - q\vec{E}_- = q\,(\Delta E_x\vec{x} + \Delta E_y\vec{y} + \Delta E_z\vec{z}) \quad \textbf{2-2}$$

where q is the charge on dipole; $\overrightarrow{E}$ represents the electric field vector; Δ is the difference operator; $\vec{x}$, $\vec{y}$ and $\vec{z}$ are the unit along x, y and z coordinate direction, respectively. For an infinitesimal distance, the change in field can be written as the dot product of gradient (∇) of each components with an infinitesimal displacement, $\mathrm{d}\vec{l}$:

$$\Delta E_x = \nabla E_x \cdot \mathrm{d}\vec{l} \quad \textbf{2-3}$$

Substituting Eq. (2-3) into Eq. (2-2), the force experienced by the dipole can be rewritten as:

$$\begin{aligned}\vec{F} &= (q\,\mathrm{d}\vec{l} \cdot \nabla E_x)\,\vec{x} + (q\,\mathrm{d}\vec{l} \cdot \nabla E_y)\,\vec{y} + (q\,\mathrm{d}\vec{l} \cdot \nabla E_z)\,\vec{z} \\ &= q\,(\mathrm{d}\vec{l} \cdot \nabla)\,\vec{E} \\ &= (\vec{p} \cdot \nabla)\,\vec{E}\end{aligned} \quad \textbf{2-4}$$

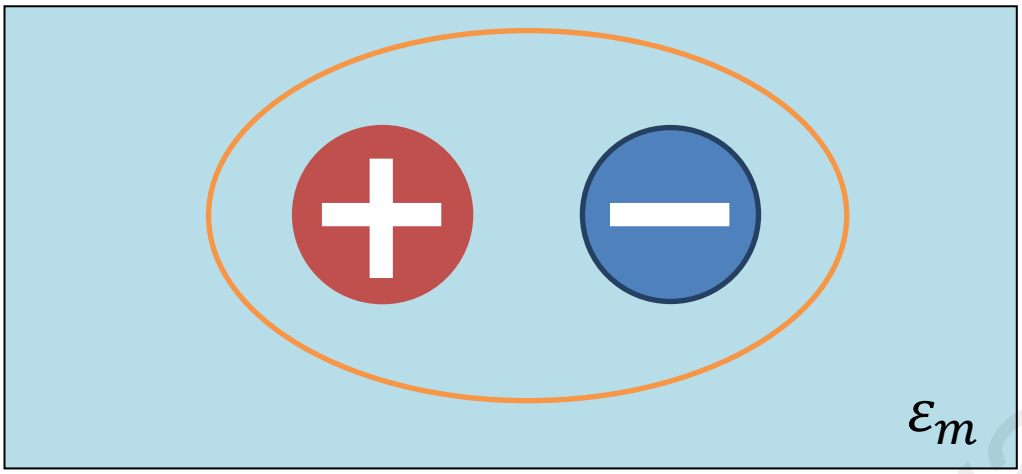

Figure 2.3: Schematic shows the presence of a dipole within a conductive medium with permittivity of ε_m. A dipole consists of two point electrical charges of opposite polarity located close together.

In order to work out the force acting on biological particles, the remark of dipole element above will be replaced by considering the example of a small dielectric sphere in a non-uniform electric field. This dielectric sphere is assumed to have radius of R and particle permittivity of ε_p. Since biological cell have the effect of perturbing the electric field, its induced dipole's electrostatic potential can be expressed as:

$$\Phi_{cell} = \frac{(\varepsilon_p - \varepsilon_m)\, R^3 \vec{E} \cdot \vec{r}}{(\varepsilon_p + 2\varepsilon_m)\, r^3} \qquad \textbf{2-5}$$

According to Gauss Law, the electric field is indistinguishable on surface that enclosed the particle (Gascoyne *et al*., 1997). Comparing Eq. (2-5) with Eq. (2-1), a relation between dipole moment and electric field can be established, which is defined as:

$$\vec{p}_{eff} = 4\pi\varepsilon_o\varepsilon_m r^3 \frac{\varepsilon_p - \varepsilon_m}{\varepsilon_p + 2\varepsilon_m} R^3 \vec{E} \qquad \textbf{2-6}$$

This equation expresses the moment of the electric dipole that would create perturbation field identical to that of dielectric sphere for all $|r| > R$. To evaluate the force on the

homogeneous dielectric particle, the effective moment from Eq. (2-6) will be substituted into Eq. (2-4). The generated force is referred as net DEP force and is given by:

$$\vec{F}_{DEP} = 2\pi\varepsilon_0\varepsilon_m R^3 Re[K(\omega)]\nabla E^2 \quad \textbf{2-7}$$

where ∇E is the magnitude gradient of electric field, expressed in RMS value. $K(\omega)$ denotes the complex Clausius-Mossotti factor and is showed as:

$$K(\omega) = \frac{\varepsilon_p^* - \varepsilon_m^*}{\varepsilon_p^* + 2\,\varepsilon_m^*} \quad \textbf{2-8}$$

where ε^* subscripts p and m are respectively assigned to permittivity of particle and medium. For a single shell model, this complex permittivity can be further represented by the formulae in Eq. (2-9):

$$\varepsilon^* = \varepsilon - j\,\frac{\sigma}{\omega} \quad \textbf{2-9}$$

such that ε is the permittivity, σ is the conductivity and ω is the angular frequency of the applied electric field. Meanwhile, j is the imaginary number which is represented by $\sqrt{-1}$. It is clear from the DEP force expression that the sign of $\mathrm{Re}[K(\omega)]$ signifies the extent of polarisation as well as determines the direction of DEP force. As the Clausius-Mossotti factor indicates the function of frequency depending on the dielectric features of both medium and particles, variation in this factor will result the change of DEP force that is frequency dependent. Noteworthy, at high frequency of AC electric field, permittivity is found to dominate over conductivity (Ikeda, Matsumaru, & Watarai, 2010). Therefore, $\mathrm{Re}[K(\omega)]$ depends only on the permittivity of both particle and suspending medium. However, at low frequency, permittivity is less dominant than conductivity and it can be neglected.

For a homogeneous sphere, $Re[K(\omega)]$ is bounded by a range of $0.5<Re[K(\omega)]<1$ within a non-uniform electric field (Pohl & Crane, 1971). When the particle polarizability is smaller than that of the medium ($Re[K(\omega)]<0$) , the particle will be pushed away from electrode edge due to the force acts in the direction of decreasing field strength. This reaction is called as negative DEP (nDEP). On the contrary, a positive-DEP (pDEP) occurs when the particle polarizability is greater than that of medium ($Re[K(\omega)]>0$). Consequently, the force will act in the direction of high electric field in which the particle is attracted toward high electric field gradient region. Both nDEP and pDEP can be illustrated through Figure 2-4.

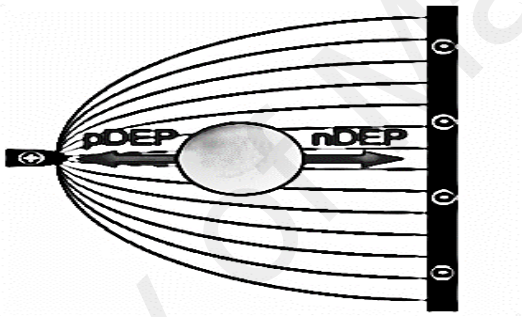

Figure 2.4: Schematic of polarized particle under nonuniform electric field (Chen et *al.*, 2006). A particle which shows stronger polarization compared to its support medium will induce pDEP force and the particle is impelled into maximum intensity electric field region. Meanwhile, when the suspending medium is more polarizable than the particle, nDEP will happen and the particle is impelled to region with minimum electric field intensity.

The general remarks above are mainly based on the dielectric properties of a single shell model, as denoted in both Eq. (2-8) and Eq. (2-9). However, it must be noted that the single shell model may not be suitable for all types of cells. Very often, biological cells are found to have heterogeneous structure with multiple layers, whereby each of them possess distinct electrical properties (Figure 2.5). For instance, a study conducted by Peng (2011) has inferred cancer cells which carry surface charges are surrounded by an electrical double layers (EDL) whereby the thickness of the EDL are depended on the concentration of suspending medium, the amount of ions present and the valence of

the electrolyte. For the purpose of DEP data analysis, two models are commonly used by researchers for the estimation of complex permittivity of these layered biological cells: the protoplast model (Lo *et al.*, 2014) and the multi-shell model (Dash & Mohanty, 2014).

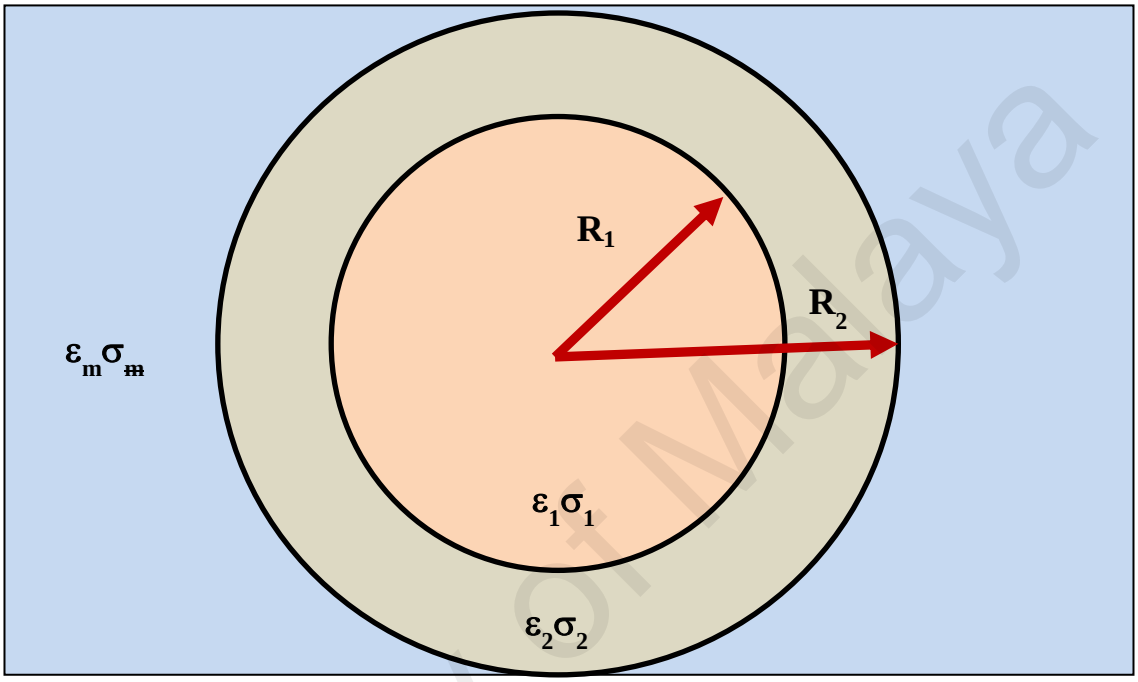

Figure 2.5: Schematic diagram of a heterogeneous particle with multiple layers.

The multi-shell model is the general model to calculate an effective complex permittivity of a particle. This model considers the core along with all the layers as a homogeneous particle with an effective complex permittivity. The conversion process of a dielectric particle with N-layers to an equivalent homogeneous particle with its generic effective dielectric property is depicted in Figure 2.6. This conversion is done in steps by taking two consecutive shells at a time. The process is to start with the core and the layer enclosing it, and is repeated until the outermost layer is incorporated into an effective permittivity and a single homogeneous particle is obtained. The final effective dielectric property of the equivalent homogeneous particle for a core with N shells is shown as (Dash & Mohanty, 2014):

$$\varepsilon_{eff}^{*} = \varepsilon_{N}^{*} \frac{\left(\frac{r_{N+1}}{r_N}\right)^3 + 2\frac{\varepsilon_{N-1}^{*} - \varepsilon_{N+1}^{*}}{\varepsilon_{N-1}^{*} + 2\varepsilon_{N+1}^{*}}}{\left(\frac{r_{N+1}}{r_N}\right)^3 - \frac{\varepsilon_{N-1}^{*} - \varepsilon_{N+1}^{*}}{\varepsilon_{N-1}^{*} + 2\varepsilon_{N+1}^{*}}} \quad \textbf{2-10}$$

This will then effectively transform the Clausius-Mossotti factor into:

$$K(\omega) = \frac{\left(\varepsilon_{eff}^{*} - \varepsilon_{m}^{*}\right)\left(\varepsilon_{eff}^{*} + 2\varepsilon_{m}^{*}\right) + \frac{\left(\sigma_{eff}^{*} - \sigma_{m}^{*}\right)\left(\sigma_{eff}^{*} + 2\sigma_{m}^{*}\right)}{\omega^2}}{\left(\varepsilon_{eff}^{*} + 2\varepsilon_{m}^{*}\right)^2 + \left(\frac{\sigma_{eff}^{*} - 2\sigma_{m}^{*}}{\omega}\right)^2}$$

$$= \frac{\varepsilon_{eff}^{*} - \varepsilon_{m}^{*}}{\varepsilon_{eff}^{*} + 2\varepsilon_{m}^{*}} \quad \textbf{2-11}$$

where ε_{m}^{*} refers to the surrounding dielectric medium; ε_{eff}^{*} and σ_{eff}^{*} represents the effective permittivity and conductivity of the heterogeneous particle, respectively.

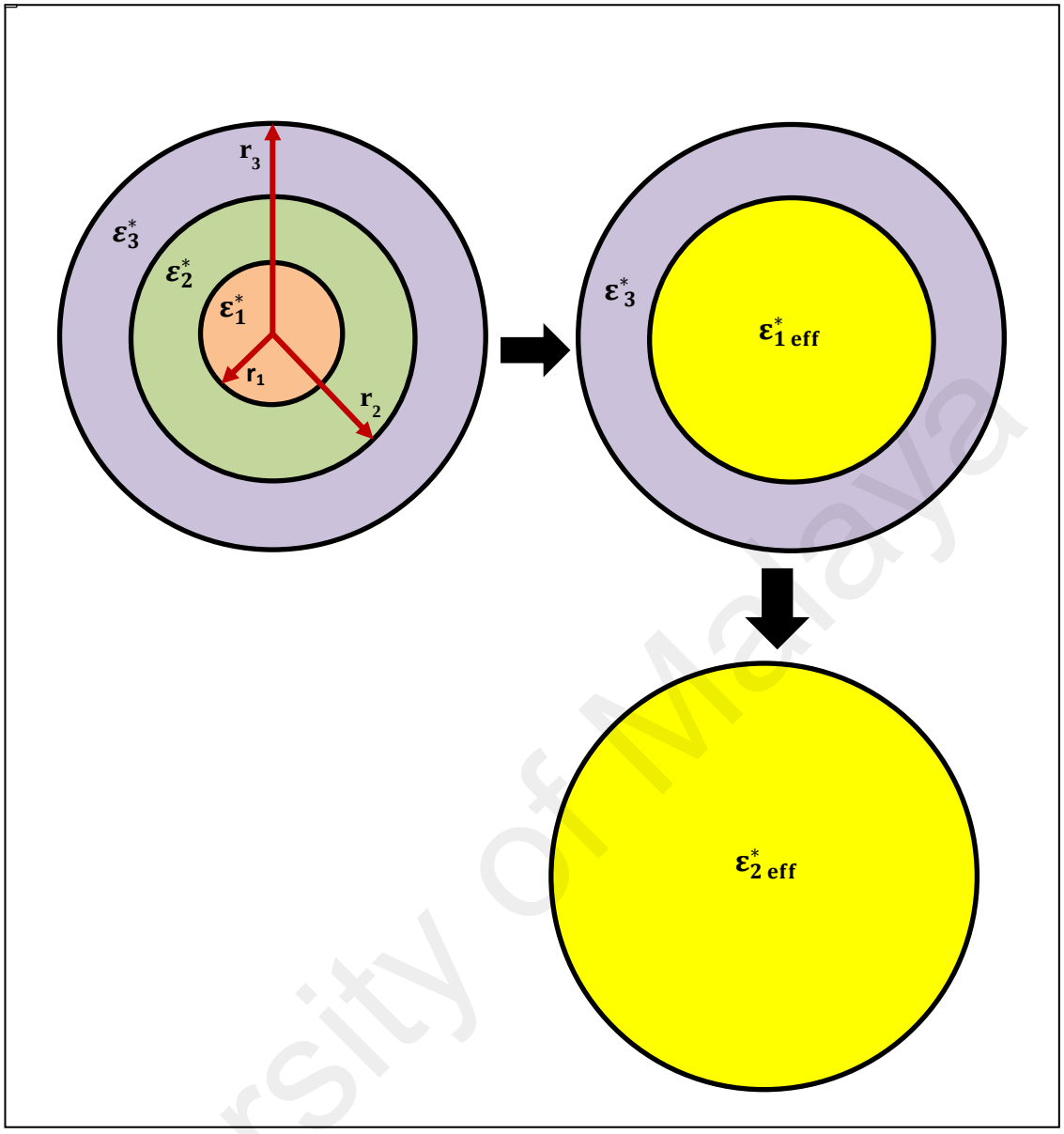

Figure 2.6: Illustration of process to convert a multiple dielectric layers to an equivalent homogeneous particle.

Although the multi-shell model above have been satisfactory in explaining the DEP behaviour of heterogeneous particle in a given solution, it is considerably too complex to be expanded in order for the dielectric properties to be directly calculated and correlated in a useful manner (Lo *et al.*, 2014). To achieve simplification, the protoplast model is developed with an assumption that the thickness of the layer is negligible with respect to the core radius, and the conductance of the membrane is zero (Dash & Mohanty, 2014). A detailed analysis of Clausius-Mossotti factor on cervical carcinoma

cells was formulated by Huang *et al*. (2012) using this Protoplast model. Its Clausius-Mossotti factor for viable cell is written as:

$$K(\omega) = -\frac{\omega^2(\tau_m\tau_c^* - \tau_c\tau_m^*) + j\omega(\tau_m^* - \tau_m - \tau_c^*) - 1}{\omega^2(2\tau_m\tau_c^* + \tau_c\tau_m^*) - j\omega(\tau_m^* + 2\tau_m + \tau_c^*) - 2} \quad \textbf{2-12}$$

where both τ_c^* and τ_c are time constants, and they can be further derived such that $\tau_c^* = \frac{C_m R}{\sigma_c}$ and $\tau_c = \frac{\varepsilon_c}{\sigma_c}$. The parameters of ε_c and σ_c denotes the electric permittivity and conductivity of the membrane, respectively. Meanwhile, C_m refers to the effective capacitance of the membrane, whereas R is the cell radius. Additionally, the constants τ_m^* and τ_m can be defined as $\tau_m^* = \frac{C_m R}{\sigma_m}$ and $\tau_m = \frac{\varepsilon_m}{\sigma_m}$, whereby ε_m and σ_m refers to the electrical permittivity and conductivity of the medium, respectively.

Inevitably, both multi-shell model and Protoplast model offer distinguishable mathematical formula to obtain dielectric properties of a heterogeneous cells. In spite of the difference, both model highlights that the magnitude and the direction of DEP force varies depending on a cell dielectric properties as well as the frequency of the applied AC signals. These parameters have influential impact for the selective separation and characterization of cells, providing that different types of cells are differ in their morphology and composition which in turn lead to different. An example of DEP phenotypes of various cell types is depicted in Figure 2.7. The DEP crossover frequency of breast tumour cell is lower than others blood cells. By choosing an appropriate frequency, cells can be separated according to their intrinsic dielectric properties.

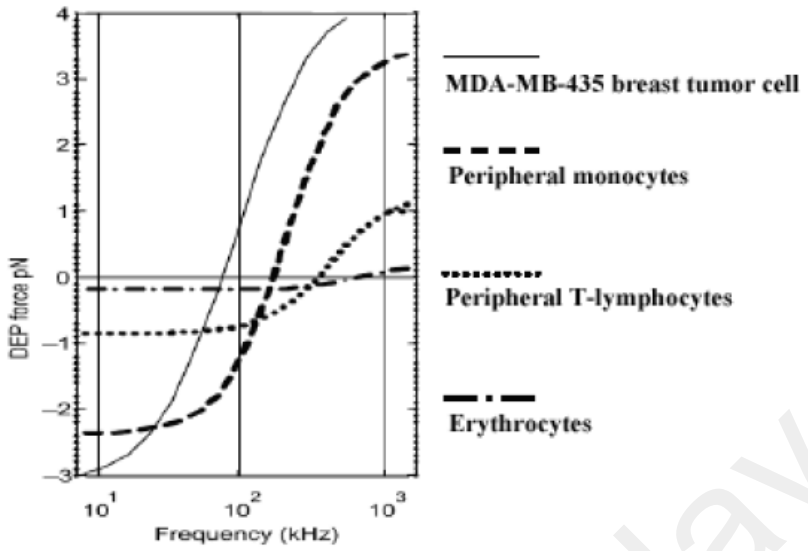

Figure 2.7: Different DEP frequency responses corresponding to different cell dielectric phenotypes (Gascoyne, 2002).

Apart of the real part of complex Clausius-Mossotti factor, the induced DEP force also relies on the gradient of electrical field (∇E^2) as evidenced by eq. (2-1). Generally, the gradient of electric field manipulates the sensitivity of DEP force to the position of particles (Kaler, Fritz, & Adamson, 1986; Saias *et al.*, 2011). In an idealized DEP configuration, the gradient of electric field emitted by microelectrode is assumed to be invariant of position and have constant value. Such a constancy of electric field gradient received by cell particle is crucial to induce efficient separation of particles based on their dielectric field properties. Since a microfluidic device have intrinsically a large surface-to-volume ratio, this device offers a significant advantage of generating high electric field gradients. For instance, gradients on the order of 10^6 V/m can be generated by applying voltage as low as 10 to 20V, which is sufficient for sorting cells such as CTCs from a blood sample (Ciprian *et al.*, 2007; Mario & Elisabeth, 2008). To convey a proper control of DEP force on experimented blood sample, the selected microelectrode design has important implication of microelectrode. The configuration of microelectrodes employed in literature will be discussed in next section.

2.5.2 Microelectrode Design

Microelectrode is made of a conductive element such as indium tin oxide (Azaman, Kadri, & Abu Osman, 2013), gold (Kadri, 2010) and titanium oxide (Zhang *et al.*, 2008). It is integrated onto a DEP-based microfluidic device to generate AC field gradient as well as to manipulate particle motion within the chamber. In order to achieve the specificity of the sorting and collection of cells, the difference between the effects of nDEP and pDEP around microelectrode are needed to be clearly distinguished (Azaman, Kadri, & Abu Osman, 2013). A suitable electrode design must therefore be prepared to fulfil the particular requirement of this study.

In general, the DEP microelectrode can be divided into three types: 2-dimensional (2D) microelectrode, 3-dimensional (3D) microelectrode and contactless microelectrode. The 2D microelectrodes are patterned within the bottom of the microchannel using conventional lithography techniques. They produces a tangential electric field on the electrode surface thus enable the manipulation particle movement around these region The DEP forces can either attract the particles down to the electrodes or repel them away and lift them up in the channel. The example of these microelectrode configuration are interdigitated (Lu *et al.*, 2008; Varshney & Li, 2009; Joon, Michael, & Chong, 2013), castellated (Gonzalez & Remcho, 2005; Morales *et al.*, 2008), spiral (Wang *et al.*, 1997), curved (Khoshmanesh *et al.*, 2009), quadrupole (Gagnon, Mazur, & Chang, 2010; Ikeda, Matsumaru, & Watarai, 2010; Ibrahim *et al.*, 2012) and divergent (Moon *et al.*, 2011). Figure 2.8 shows the selection of these designs.

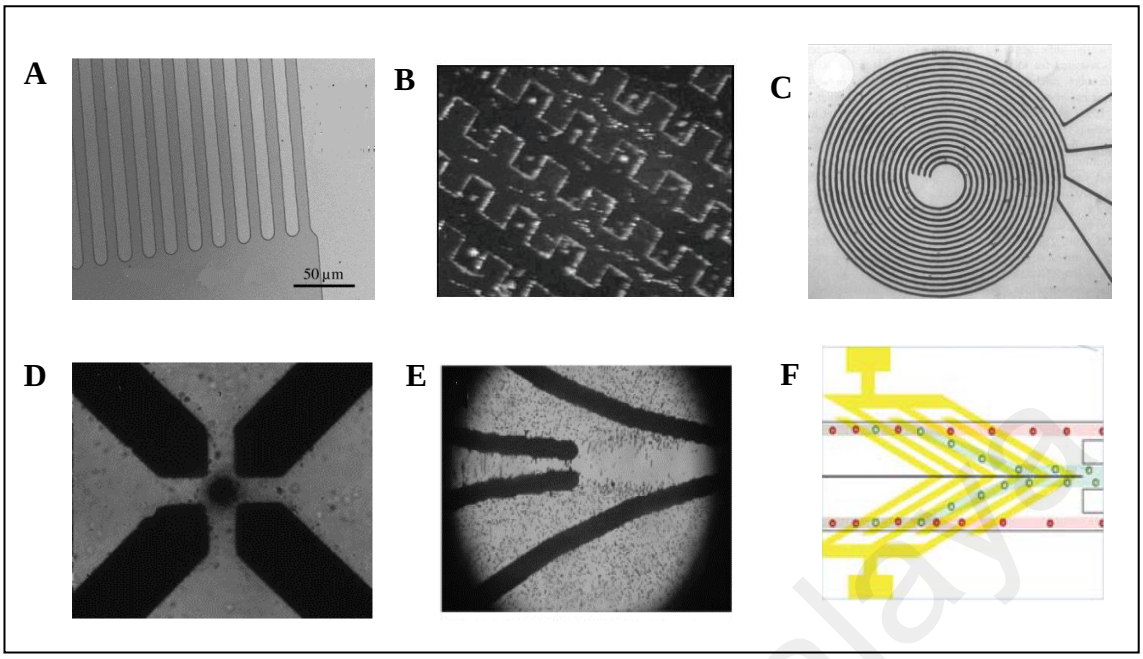

Figure 2.8: Classification of DEP devices according to the microelectrodes configurations: (A) interdigitated (Joon, Michael, & Chong, 2013), (B) castellated (Morales *et al.*, 2008), (C) spiral (Wang *et al.*, 1997), (D) quadrupole (Gagnon, Mazur, & Chang, 2010), (E) curve (Khoshmanesh *et al.*, 2009), (F) divergent (Moon *et al.*, 2011).

In recent research, a planar DEP-based technology known as contactless microelectrode is developed (Gascoyne & Shim, 2014). This device avoids the direct contact between electrodes and sample by replacing the conventional metallic electrode in 2D configuration with fluidic electrode channels. The fluidic electrode channel consists of highly conductive fluid and is separated from the microchannel with a thin insulating barrier (Huang *et al.*, 2012). As a result of this method, the DEP device fabrication issues such as electrode delamination and bubble formation can be eliminated (Gascoyne & Shim, 2014). Although previously reported 2D microelectrode shows a favourable result in DEP-based on-chip blood sample analysis, there are some drawback associated with these planar microelectrode design. Fabbri *et al.* (2013) have found that the electrical field to be decayed exponentially with the distance away from the planar electrode. The finding is in concordance with study conducted by Wang *et al.*

(2007) who stated that cell which was positioned away from the planar electrode were less controlled by DEP force.

Alternatively, the 3D microelectrode structures such as extruded vertical electrodes on bottom, bottom/top patterned (Wang *et al.*, 2007), or sidewall patterned microelectrode have been developed (Voldman *et al.*, 2003). In contrast to 2D microelectrode, the lateral positioning design of these electrodes allow an electric field gradient to be generated along the width of the channel direction. Therefore, a strong DEP force can be generated to cover the larger volume of microchannel and affect the particle more efficiently. In this case, The cell sorting done with 3D microelectrode had shown an improvement of 15% in cell recovery rate in contrast to the conventional 2D microelectrode (Wang *et al.*, 2007). Regardless of its enhanced isolation performance, 3D microelectrode structure is rarely applied in experimental DEP studies. This issue is mainly caused by its cumbersome and costly fabrication procedure. As such, a specialised equipment, known as femtosecond laser micromachine is necessary for producing sophisticated patterning of the 3D micro-cavity mold (Chen, Du & Li, 2006; Ciprian *et al*., 2007; Li *et al*., 2014). Furthermore, this equipment is commonly inaccessible to many research group .

In context of current study, an electrode design will be employed to conduct performance evaluation of a proposed integration technique. Due to the fabrication limitation in Malaysia microfluidic foundry, the most suitable electrode design would be planar electrode type. Since our study will feature a continuous flow, there is one criteria which need to be taken into consideration when selecting microelectrode structure. As such, it must have a mean to isolate cells and direct them toward their designated outlets under constant suspension injection. In literature, a divergent interdigitated electrode array developed by Moon *et al.* (2011) has shown an efficient

performance, whereby the recovery rate of CTCs is 75.81% from 1mL of diluted blood sample. Therefore, it will be adopted into our study to create chamber for DEP effect.

2.6 Magnetophoresis

Analogously to DEP, a magnetophoresis (MAP) involves the manipulation of magnetic particles in a viscous medium, using an applied magnetic field. It has emerged as a topic of great interest in a wide range of technological areas: from pollutants removal (Yavuz *et al.*, 2006), to biomedical applications such as protein isolation (Corchero & Villaverde, 2009), drug delivery and magnetic particle imaging (Krishnan, 2010). This approach takes advantages of the distinctive magnetic permeability of particles and their nonlinearity of magnetic response under magnetic field to remove them from a complex medium by the use of non-homogeneous magnetic field.

In a microfluidic device, the method of MAP separation can be applied via two ways: the immunomagnetic separation and the non-immunomagnetic separation. In an immunomagnetic separation approach, the magnetic microparticles are used to conjugate with antibody proteins which are specific to the cell membrane protein of interests, to help enhancing their attraction towards the magnetic field around the ferromagnetic area (Wang *et al.*, 2013). Conversely, a non-immunomagnetic separation method isolates cells based on their native magnetic properties (Pamme & Manz, 2004). As alluded previously, the aim of this study is to develop a label-free based-biophysical technique for CTC isolation. Thus, the non-immunomagnetic MAP separation method will be selected as the enrichment technique in our proposed device.

In clinical-trial, the non-immunomagnetic MAP method is showed as a promising approach for separating RBC from peripheral blood. The presence of iron-containing molecules, such as haemoglobin within the RBC has given it an inherent distinctive magnetic feature, thus distinguish them from CTC and WBC (Furiani, 2007). CTC and

WBC, on the other hand, is found to be lacking of iron-manganase-containing molecules (Esmaeilsabzali *et al.*, 2013). When subjected under an inhomogeneous magnetic field, they behave as the diamagnetic microparticle, such that the cells are repelled from the high magnetic field gradient. It has been evidenced through a study conducted by Jin *et al.* (2012) on the magnetophoretic mobility of eight cancer cell line. Their study discovered that a significant motion among cancer cell which approaches that of diamagnetic WBC in an imposed magnetic field.

Although paramagnetic element such as iron is found in RBC, few studies has reported a profound change in magnetic response for both oxygenated and deoxygenated RBC. In 1936, Pauling and Coryell carried out an experiment to measure the magnetic moment of RBC with oxyhemoglobin and RBC with deoxyhemoglobin. Their result had indicated that the magnetic susceptibility of haemoglobin is dependent on the chemical bonds in heme-group during oxygenation process. For instance, the presence of ionic bond within deoxygenated ferrous haemoglobin will give rise to the unpaired electrons in the heme- groups, thus making them paramagnetic in which cell tends to be attracted toward high magnetic field. Meanwhile, the oxygenated RBC, which consists of covalent bond would result in a low magnetic susceptibility and therefore behave as diamagnetic cell (Pauling & Coryell, 1936). A research group from Lemer Research Institute based in Ohio had developed a cell tracking velocimetry to measure the mobility of erythrocytes under an induced non-uniform magnetic field. Their result had shown a magnetophoretic mobility of $3.86 \times 10^{-6} mm^3 s/kg$ for deoxygenated erythrocytes, indicating a significant paramagnetic component relative to the blood sample, thus in agreement with Pauling's study (M. Zborowski *et al.*, 2003). To enhance the RBC separation in magnetophoretic stage, Furiani (2007) and Shen *et al.* (2012) has clarified the need for the blood sample obtained from the patient to be first deoxygenated.

To date, relatively few systems have been developed for magnetically separate unlabelled blood cells within microfluidic channel. In spite of it, studies has shown promising results with approximately 90% RBC recovery with this method. In 2006, Han and Frazier developed the first microfluidic-based-MAP device for direct separation of RBC and WBC based on their native magnetic properties. A microseparator made of ferromagnetic wire was embedded in the channel wall to generate a high-gradient magnetic field within the MAP chamber. In order to evaluate the recovery rate for both RBC and WBC, a Coulter counter was employed to measure the amount of particle accumulating in specific outlet. The experimental results showed that the use of single-stage microseparator allowed 91.1% of the RBC to be continuously separated from a whole blood sample at flow rate of $0.1 mms^{-1}$, whereas a three-stage microseparator separated 93.5% of red blood cells at a same volumetric flow rate (Han & Frazier, 2006). In 2008, a research group from Institute of Bioengineering and Nanotechnology, Singapore studied the performance of their proposed MAP-based microfluidic device by continuously pumping in a diluted blood sample (1:10 in PBS) at the flow rate of 0.5 to 0.7mL/h. A strong magnetic field perpendicular on the flow direction was generated through the array of ferromagnetic dots which was patterned at the bottom of the channel, to help generate a gradient of magnetic field. The proposed device had successfully trapped an average of 95% of RBC at the outlet collection port (Iliescu *et al.*, 2008). In the same year, another research group from Inje University, Republic of Korea had reported that their MAP device to be able to continuously separate out 93.9% of red blood cells and 89.2% of WBCs from the whole blood sample (Jung & Han, 2008).

Based on the cell separation outcome presented above, it clearly shows that the MAP provides a significant effectiveness in RBC separation. Therefore, it will be used as the enrichment stage in our proposed integrated microfluidic device to separate the RBC

from a given sample. Since other nucleated cells exhibit the same response under magnetic field, an additional downstream separation through the DEP can be conducted to further isolate CTC from WBCs and platelets.

2.6.1 Theory

The MAP force experienced by a cell suspended in a fluid arising from a change in the magnetic energy of the system. Given a region characterized by a non-homogeneous magnetic field, the magnetic force exerted on a magnetized cell can be written as (Kawano & Watarai, 2012):

$$\overrightarrow{F_{MAP}} = \int_V (\vec{M} \cdot \vec{\nabla}) \overrightarrow{B_{ext}} \, d\vec{v} \qquad \textbf{2-13}$$

where V is the volume of a cell, M denotes the resulting magnetization of the material, ∇ is the gradient operator and $\overrightarrow{B_{ext}}$ is the magnitude of the external magnetic flux density. As multiple studies show that saturation does not occur in blood cells for most of the applied magnetic field, the relationship between the density of the induced magnetic dipole moments within the magnetic material and the induced magnetic field strength inside a cell (H_{in}) can be represented by (Pamme & Manz, 2004; Furiani, 2007):

$$\vec{M} = \chi_o \overrightarrow{H_{in}} \qquad \textbf{2-14}$$

where χ_o is the volume magnetic susceptibility. It can further represented by the difference in magnetic susceptibility of cells, χ_p, and its surrounding buffer or medium, χ_m:

$$\chi_o = \chi_p - \chi_m \qquad \textbf{2-15}$$

According to the Maxwell's law of electromagnetism, the total magnetic field in a magnetized region (H_{in}) is the sum of external applied magnetic field (H_{ext}), and the stray field outside the magnet and the demagnetizing fields of the magnet ($H_{d,c}$), such that (Furiani, 2007):

$$\begin{aligned}\overrightarrow{H_{in}} &= \overrightarrow{H_{ext}} + \overrightarrow{H_{d,c}} \\ &= \overrightarrow{H_{ext}} - N_{d,c}\vec{M}\end{aligned} \quad \textbf{2-16}$$

where $N_{d,c}$ refers to the demagnetization factor relative to the cell. The corresponding amount of external magnetic fluxes flow through the cell surface can be related the induced magnetic field from external source by:

$$\overrightarrow{B_{ext}} = \mu_f \overrightarrow{H_{ext}} \quad \textbf{2-17}$$

in which, μ_f represents the permeability of the fluid. Substituting Eq. (2-15) into Eq. (2-14), $\vec{M}$ can be rewritten as (Shen *et al.*, 2012):

$$\begin{aligned}\vec{M} &= \chi_o \left(\overrightarrow{H_{ext}} - N_{d,c}\vec{M}\right) \\ &= \frac{\chi_o}{\chi_o N_{d,c} + 1}\overrightarrow{H_{ext}}\end{aligned} \quad \textbf{2-18}$$

In majority of the cell, the measurement for χ_o is relatively low, such that in the order of magnitude of 0.1. Thus, the demagnetization field for the cells can be neglected, resulting in a linear magnetization characteristic with respect to the external applied magnetic field, given by:

$$\vec{M} \approx \chi_o \overrightarrow{H_{ext}} \quad \textbf{2-19}$$

Since the magnetically active structure within the microfluidic device is sized as to have dimension greater than blood cell, variations of magnetic field will not be considerable within the volume of a single cell. This leads to the collapse of integration in Eq. (2-13) and is replace with a multiplication factor corresponding to the volume of the modelled cell, V_c. By substituting Eq. (2-15), (2-17) and (2-19) into Eq. (2-13), the final expression of MAP force can be defined as:

$$\overrightarrow{F_{MAP}} = \mu_f \, (\chi_p - \chi_m) \, V_c \, (\overrightarrow{H_{ext}} \cdot \vec{\nabla}) \overrightarrow{H_{ext}} \qquad \textbf{2-20}$$

In accordance with the equation above, the MAP force is linearly related to the volume of immersed particle as well as the permeability of the suspended medium (Pamme & Manz, 2004). The time-averaged of a MAP force is independent of the field polarity since the MAP force vector is directed along the gradient of the magnetic field intensity, $\nabla \vec{H}_{rms}^2$ (Forbes & Forry, 2012). Noteworthy, the direction of the MAP force can be determined by the difference in magnetic susceptibility between a magnetic particles (χ_p) and its surrounding buffer medium (χ_m). For instance, when the calculated difference is positive ($\chi_p - \chi_m > 0$), the cells will be aligned in a magnetic field and experience a force toward magnetic field maxima. The force generated is referred as positive-MAP (pMAP) and the cell would be paramagnetic. Likewise, when a suspended cell have smaller magnetic susceptibility in contrast to the surrounding medium ($\chi_p - \chi_m < 0$), a negative-MAP (nMAP) will take effect in which the cells will be repelled from the magnetic field and pushed toward a magnetic field minima. These types of cells would be diamagnetic as they develop a weak magnetization in the direction of magnetic field (Plouffe, Lewis, & Murthy, 2011).

2.6.2 MAP Configuration

To effectively separate the RBC from a given blood sample, the present of an external magnetic field source has an important implication. This magnetic source will generate a localized high magnetic field gradient over the confined space of a microfluidic channel, to produce a force to sort and immobilize targeted cell under a continuous flow.

In literature, the conventional magnetic manipulation in a microfluidic device is generally accomplished by placing permanent magnets or electromagnets outside the microdevice (Pamme & Manz, 2004; Shen *et al.*, 2012; Zhu *et al.*, 2014). A permanent magnet used in the microfluidic application is usually a small neodymium-iron-boron (NdFeB) magnet featuring magnetic flux densities of up to 500mT. Meanwhile, the electromagnets consists of tapered cores which are made of highly permeable material such as soft iron (Ramadan, Poenar, & Yu, 2008) or μmetal, in order to achieve high field gradients in contrast to permanent magnet. This field can be switched on and off depending on the applied electric current. For instance, a study done by Pamme and Manz (2004) had placed a small permanent magnet upon the microchannel and perpendicular to the direction of flow to separate magnetic and non-magnetic beads. Depending on the bead's size and magnetic properties, it would be deflected more or less from its natural path due to the presence of a magnetic field. The addition of spacers at the inflow and outflow area had permitted the independent collection of different particles. For instance, the magnetic particles would be dragged into the magnetic field and left the chamber via one of the spacer, while non-magnetic particle left the chamber through the spacer opposite to the sample inlet. This device is illustrated in Figure 2.9.

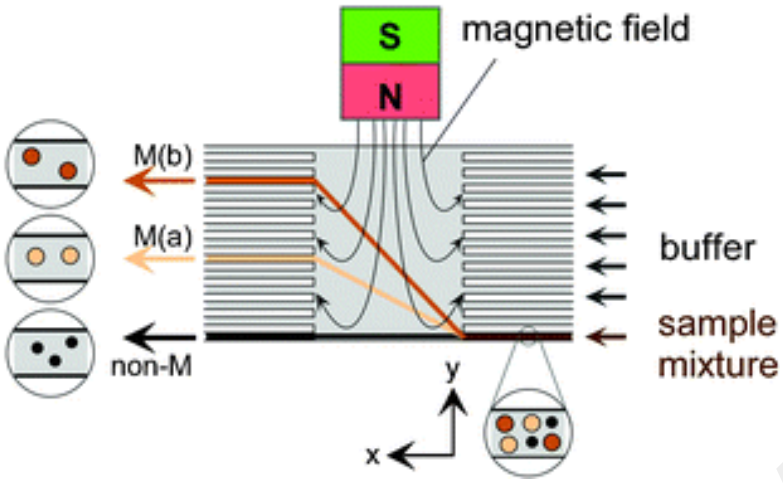

Figure 2.9: Magnetic separation principle by Pamme and Hanz (2004).

In 2004, a study conducted by a research group from Princeton University, New Jersey, has indicated that the flux density would decrease with distance from the magnet surface. The cell capture efficiency was found to be greatly diminished as the size of flow channel increased due to the relatively short range effectiveness of the magnetic force (Inglis *et al.*, 2004). To overcome this limitation, this group has proposed the use of ferromagnetic element such as the nickel strip array at the bottom of the separation chamber, whereby each having the length of 10µm wide and a thickness of 2µm, aligning at an angle of 11° to the fluid flow. A high magnetic field gradient was generated around nickel strips array using permanent magnets (200mT) as the external field source. This phenomenon had created magnetic traps around these ferromagnetic strips, thus altered the movement of cells which primarily featured paramagnetic. The magnetically labelled leukocytes were attracted to the strips and found to flow along the strips rather than the direction of fluid flow, as shown in Figure 2.10. Their results has provided an important information, such that the use of soft magnetic element within the microchannel can be served as magnetic field concentrators thus enhancing the separation process.

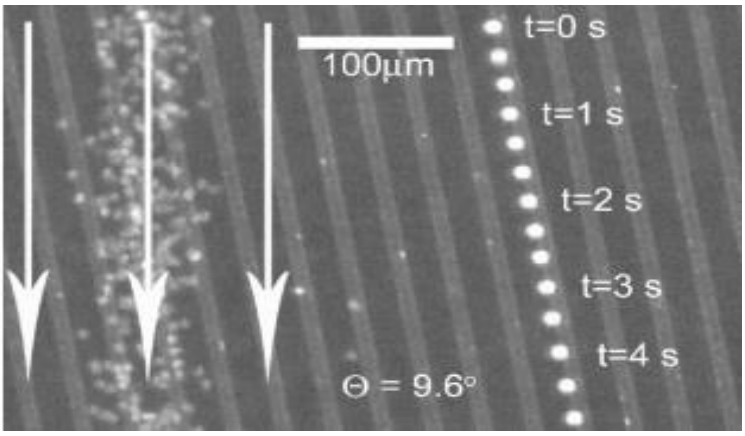

Figure 2.10: Time lapse image of the magnetic-labelled leukocytes'movement at an angle of 9.6° to the fluid flow indicated by the white arrows (Inglis *et al.*, 2004).

Following by their discovery, various microfluidic designs using integrated ferromagnetic elements have been proposed. Xia *et al.* (2006) utilized a layer of soft magnetic material (NiFe) with a micro-comb configuration that has triangular saw-tooth edge positioned close to the side of the channel (see Figure 2.11(A)). Their study reported that the separation performance of this layer can be improved by setting its thickness equal to the height of the channel even at high volume throughput. Meanwhile, Kang *et al.* (2008) and Shen *et al.* (2012) electroplated a nickel bar alongside the edge corner of the main separation channel (see Figure 2.11(B)). Once magnetized, the posts generated strong magnetic field gradients and trapped the paramagnetic-featured-cells in a flowing stream of water.

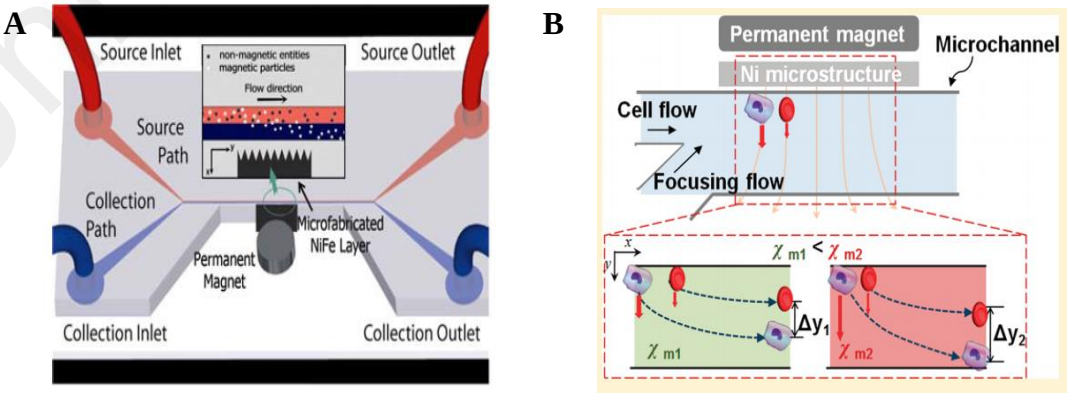

Figure 2.11: Schematic depiction of a MAP microfluidic separation device by (A) Xi *et al.* (2006) and (B) Shen *et al*. (2012).

Apart of using external magnetic source to magnetize the ferromagnetic structure within the microfluidic channel, some works had directed toward the system using planar electromagnets to generate magnetic fields. A planar electromagnet typically consists a current carrying wire which is made of the conducting material, such as copper, gold and aluminium (Song, Kwak, & Jung, 2009). Varying the geometry of the carrying wire strongly impacts the trapping profile of magnetic and non-magnetic particles. Examples of the electromagnet design within the microfluidic channel includes meander μ-coil (Mukhopadhyaya, 2005), single current loop (Song, Kwak, & Jung, 2009), spiral μ-coil (Ramadan, Poenar, & Yu, 2008) and loop array (Pauline *et al.*, 2014). Figure 2.12 shows a selection of these electrode designs.

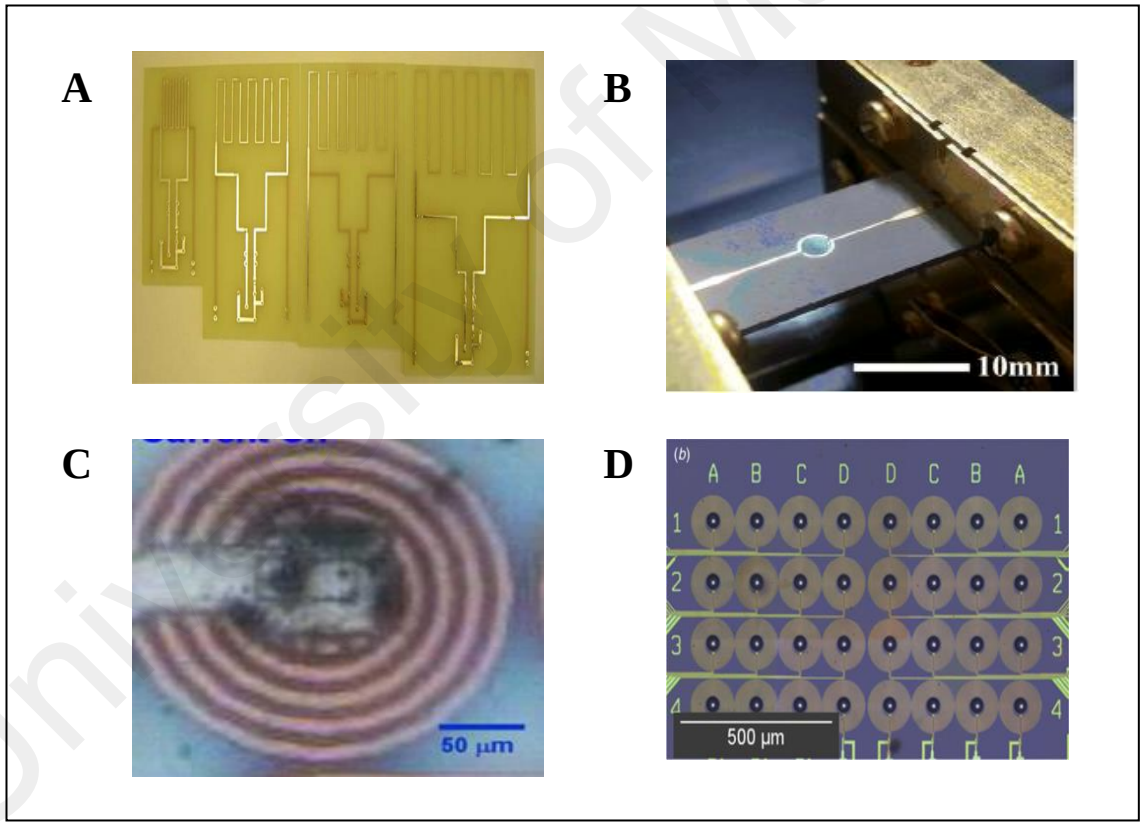

Figure 2.12: Classification of MAP microfluidic device according to the planar electromagnet configurations: (A) meander μ-coil (Mukhopadhyaya, 2005), (B) single current loop (Song, Kwak, & Jung, 2009), (C) spiral μ-coil (Ramadan, Poenar, & Yu, 2008), and (D) loop array (Pauline *et al.*, 2014).

Although a planar electromagnet enables the strength of the resultant magnetic field to be tuned by varying current, there are some limitations of its usage in lab-on-a-chip

systems. A study conducted by Siegel *et al.* (2006) has showed that this device produced weaker magnetic field in contrast a permanent magnet. It is further evidenced when Liu *et al.* (2009) found that the strength of a small electromagnet which was made of large number of windings and subjected with high current, was not comparable to that of a small NdFeB permanent magnet (Liu *et al.*, 2009). Besides, the Joule heating derived from currents flowing through the planar electromagnet winding will result the generation of thermal energy. Such a scenario would cause the degradation of the device which consequently decrease its separation efficiency (Plouffe, Lewis, & Murthy, 2011). Furthermore, the elevated temperature caused by the Joule heating will result in cell lysis due to their labile characteristic in response to the microenvironment (Hou *et al.*, 2011).

In the context of current study, the permanent magnet will therefore be selected to create a magnetic field within the proposed MAP microchamber. However, it should be noted that the aforementioned magnetic configurations are limited by the range of magnetic capture force that they provide, which is typically only effective for cell capture within tens of microns of the elements. Subsequently, they are only effective for a relatively narrow microchannel (<100μm), thus limiting the system throughput (Furiani, 2007; Jung & Han, 2008; Lim *et al.*, 2014). To circumvent this problem, a robust MAP platform design which facilitates both high throughput and separation efficiency will be proposed in this study. As the ultimate aim of the MAP stage described herein is to isolate RBCs and enhance the selectivity of the downstream DEP force application, additional conditions which will affect the device efficiency particularly of the magnetic field are needed to be addressed within the model. It has been shown that the magnetic field and force generated by previous studies is defined by the magnet geometry and pole orientation (e.g. attraction, repulsion, and single

magnet configuration). These variables will therefore be highlighted in this study to help developing the proposed MAP stage.

2.7 Blood Cell Properties

From the point of view of biological systems analysis, it is important to determine the basic molecular features that are necessary for proper modelling. The cells that we are focusing in this study consists of blood cells and circulating tumour cells (CTCs). These cells are non-uniform such that red blood cell (RBC) consists of spherical shape meanwhile white blood cell (WBC) and CTC is multilayered particle with irregular-shape centred. Despite of the difference in cell morphology, the fundamental physic of a cell would not be changed as the internal cellular structure primarily manifests itself in the cell conductivity, permeability and permittivity (Kashevskii *et al.*, 2006; Vykoukal, Gascoyne, & Vykoukal, 2009). Detailed knowledges of these properties are important to carry out our computational design study to identify and separate the cell subpopulations.

Generally, normal blood is made up of RBCs, WBCs and platelets, which are carried within fluid named plasma. Each of them carried a distinctive morphology and physical characteristic and they are described in below:

(i) A plasma was found to behave like a Newtonian viscous fluid. This transport fluid has the following properties, such as : viscosity of 0.001 kg/s, density of 1000 kg/m^3 , magnetic susceptibility of -7.7x10^{-6} (SI) (Yang *et al.*, 2000), electric permeability of 78 and electric conductivity of 1.8 S/m (Park *et al.*, 2011).

(ii) RBC will occupy 50% of blood volume and their number is about 5 million/mm^3 . Human RBCs are disk shaped, with a diameter of 8.0±0.4 μm

and thickness of 2.8μm. The magnetic susceptibility of a RBC depends on the oxygenation state of its haemoglobin. For deoxygenated RBC, the values given was -3.9×10^{-6} (Yang *et al.*, 2000). Meanwhile, the dielectric properties of RBCs were given as: membrane permittivity of 0.052 S/m, cytoplasm relative permittivity of 57, and cytoplasm conductivity of $9 mFm^{-2}$ (Chen *et al*., 2014)

(iii) WBC is making up of 1/600 of the cellular volume with cell count range from 5000 to $8000/mm^3$. It comprises of five different kinds of cells which are classified into two groups: agranulocytes (lymphocyte and monocyte), and granulocytes (neutrophil, eosinophil and basophil) (Merrill, 1969). These cells are rounded in shape, with diameter that range from 6μm to 15μm (Pommer *et al*., 2008; Chen *et al*., 2011). In most study, a WBC's magnetic susceptibility was assumed similar to that of the water, which is -9.2×10^{-6} (Takayasu, Kelland, & Minervini, 2000; Furiani, 2007) . This value is consistent with measurement made by Han and Frazier (2006) in which a value of -9.9×10^{-6} was obtained for WBC with 5μm diameter. The ranges of WBC electrical properties from previous publications are as follows: membrane relative permittivity of 0.56 – 0.76 S/m, cytoplasm relative permittivity of 100– 151, and cytoplasm conductivity of 9.9 – 13 (mFm^{-2}).

(iv) Platelet consists of 1/800 of cellular volume with 250000 to $300000/mm^3$. It has a diameter of about 2.5μm and is much smaller compared to other blood cells (Lynch, 1990). Its magnetic susceptibility was found to be similar to that of WBC, which is -9.2×10^{-6} (Furiani, 2007). Meanwhile, both its cytoplasm relative permittivity and conductivity was given by 0.25 and 1×10^{-7} (Armitage, 1985), respectively.

In contrast to the mentioned blood cells, the reported CTCs in literature show a significant variability in size with consistent elongated shaped, ranges from 7.52µm to 40µm (Hofman *et al.*, 2011). Both breast and prostate CTC are of interest in this study in which a breast CTC have the largest size in CTC taxonomy (such that range from 13 to 40µm) and vice versa for the prostate CTCs (range from 7 to 13µm) (Baccelli *et al.*, 2013; S. Park *et al.*, 2013). A study conducted by Jin *et al.* (2012) has showed that the prostate CTC has magnetic susceptibility of -9.4966×10^{-6} . The magnetic susceptibility of CTC is found to decrease in accordance to cell size, in which breast cancer with size of 13 µm has the magnetic susceptibility of -9.5143×10^{-6} while breast CTC with size of 20µm has of -9.5179×10^{-6} (Kashevskii *et al.*, 2006). In term of membrane electric permeability, both type of CTCs exhibit a similar measurement, which is 0.52. Meanwhile, for membrane conductivity, breast and prostate CTCs shows a value of 0.62S/m and 0.21S/m, respectively (Chen *et al.*, 2011).

The cell parameters as mentioned above can be summarized in Table 2.1 as showed below:

Table 2.1: The dielectric and magnetic parameters of cells

Cell Type	**Mean radius, r (µm)**	**Magnetic susceptibility, χ_{cell}**	**Electrical properties**		
			$\sigma_{cytplasm}$ (S/m)	**$\varepsilon_{cytoplasm}$**	**$C_{membrane}$**
RBC	4.0	-3.69×10^{-6}	0.52	57	9
WBC	7	-9.9×10^{-6}	0.76	150.9	13.29
Human breast cancer MDA-231	20	-9.5143×10^{-6}	0.62	52	25.9
Human prostate cancer HeLa	7.36	-9.4966×10^{-6}	0.21	52	12.4
Platelet	2	-9.2×10^{-6}	0.25	1×10^{-7}	-

2.8 Summary

A major challenge for a microfluidic device in detecting the CTCs comes from the fact that the cell density of CTCs in a peripheral blood is extremely low (0~1 cells per millilitres) compared to the density of other blood cells. On a side note, the overloading cell issue in a DEP study has hindered its effectiveness in detecting the CTCs. To circumvent these issues, integration of DEP with another cell separation force, which is MAP, will be attempted in this study.

The principles and limitation of both DEP and MAP have been briefly described in this chapter to furnish the basic concepts necessary for understanding the following dissertation chapters. Based on the characterization results of the presented DEP and MAP separation systems in literature, a MAP system cascaded with a DEP system could potentially enable efficient and novel separation of target rare cells from human whole blood sample. As such, a continuous flow MAP will be used in stage one as a pre-enrichment device for separating most RBCs from a human whole blood sample, concentrating target rare cells and other nucleated blood cells. In stage two, the integrated continuous flow DEP could be used as an isolation device for separating targeted rare cells out from other nucleated cells.

Notably, a precise control of the cell's microenvironment of a microfluidic system still remains a vexing challenge within the technological realm. In this case, computational modelling could be served as a decision tools for researchers to aid in the design of experimental setup and to gain a further insight into the separation phenomenon. A researcher can rapidly determine how design changes will affect chip performance, thereby reducing the number of prototyping iterations. Perhaps even more importantly, numerical protyping which is applied at the conceptual design stage can provide an order of magnitude estimates of potential chip performance, thus enabling a

fruitful path to be taken from the beginning of experiment. Henceforth, in the course of this study, a computational modelling method will be employed to develop an integrated microfluidic system which capable of delivering high isolation efficiency. To attain a more realistic device design, the physical parameter of blood cells associated with MAP device and DEP device is obtained from literature and directly accounted in the resulting computation. To date, there were no benchmark datasets that have studied the integration of DEP and MAP for CTCs isolation.

CHAPTER 3:

MICROFLUIDIC DEVICE DESIGN AND MODELING

3.1 Introduction

As alluded in previous chapter, the MAP will be employed in our study to help enhance the CTC separation in the DEP stage. However, it should be noted that the control of fluid flow and forces distribution within a microfluidic device are highly influential for the deposition and separation of cell within the chamber. To achieve a desirable output, the performance of a proposed MAP stage is needed to be optimized and evaluated before integrating it with a DEP stage. In short, this chapter particularly documents the processes involved in developing a new generation of integrated MAP-DEP technique microfluidic device. In Section 3.2, the part mainly revolves around the quantitative requirements for the device design whilst Section 3.3 and 3.4 will bring out the general background of the design. Section 3.5 will highlight the procedures needed for optimizing the channel structure by COMSOL simulation. Additional numerical methods have been developed to simulate these solvent-solute interactions within the proposed platforms.

3.2 Requirements

In proposing a design of CTC detection microfluidic device, the first step is to define the required specifications. including the developed channel flow pattern, optimum fluid mean velocity, uniformity of flow, material of microfluidic channel, the electric and magnetic field gradient produced, and fabrication complexity, as described in the following:

3.2.1 Flow Pattern

In our microfluidic system, laminar flow is highly desirable. It is defined as streamline flow where fluid flow in a parallel layer (Kamholz & Yager, 2001). Such a flow has thus resulted cells to be transported in a relatively predictable manner across microchannel. For a microfluidic device, the flow would be completely laminar if Reynolds number is less than 200 (Levenberg & Shemesh, 2014). Notably, Reynolds number (Re) is defined as ratio between inertial forces and viscous forces in particular flow as such:

$$Re = \frac{inertia\ force}{viscous\ force} = \frac{pVD}{\mu} \quad \textbf{3-1}$$

where p is the fluid density, V is the mean fluid velocity, D is the diameter of microfluidic channel while μ is the fluid viscosity. Since blood sample will be used as the main material flow through the channel during the simulation process, the fluid viscosity will remain the same for all proposed geometries. In order to achieve laminar flow, the inlet diameter of microfluidic channel should be kept as small as possible, with the maximum value of 1mm in our study. Besides, the depth of the microfluidic channel needs to be constant across the whole microdevice.

3.2.2 Optimum Fluid Mean Velocity

When a specimen is pushed into the microfluidic channel, the hydrodynamic force ($\mathbf{F_{HD}}$) applied on a cell will be influenced by the flow velocity. It can be derived from Stokes' Law, as such (Wang *et al*., 2007; Lee *et al*., 2012):

$$\vec{F}_{HD} = 4\pi\eta R\vec{v} \quad \textbf{3-2}$$

in which $\vec{v}$ is the relative velocity between the cell with a radius, R and the flow. This equation has shown that the flow velocity is directly proportional with hydrodynamic force.

It must be noted that apart of hydrodynamic force, the cell will experience a MAP force (**F_{MAP}**) or a DEP force (**F_{DEP}**) in our proposed CTC capture micro-device. Therefore, as the cells are directed into the MAP or DEP microchamber, there are some points corresponding to the electrical or magnetic field gradient in tangential direction relative of flow. These forces will deviate the flow direction of cells and direct them to their targeted outlet under **F_{HD}**. However, if the applied flow rate is not strong enough to carry them through the channel, a **F_{MAP}** or **F_{DEP}** along the length direction will hold them from the **F_{HD}** of the flow and trap the cells in a series of virtual traps along the channel. Such a condition will result in an undesirable accumulation and suspension of cells along the channel, which in turn causes uneven electrical or magnetic field intensity to be measured during cell separation analysis. In order for the flow to generate sufficient **F_{HD}** to carry cells toward their respectively outlet, the flow velocity must overcome the **F_{MAP}** or **F_{DEP}** along the length of channel (x-direction). The minimum flow velocity within DEP (v_{Dmin}) or MAP stage (v_{Mmin}) can be derived and written respectively as below:

For DEP,

$$\vec{F}_{HD} > \vec{F}_{DEP}$$

$$4\pi\eta R\vec{v} > 2\pi\varepsilon_0\varepsilon_m R^3 Re[K(\omega)]\frac{\partial E^2}{\partial x}$$

$$\vec{v} > \frac{\varepsilon_m\varepsilon_0 R^2}{2\eta}\, Re[K(\omega)]\nabla\frac{\partial E^2}{\partial x}$$

$$v_{D\_min} = \frac{\varepsilon_m \varepsilon_0 R^2}{2\eta} Re[K(\omega)] \nabla \frac{\partial E^2}{\partial x} \quad \textbf{3-3}$$

For MAP,

$$\vec{F}_{hd} > \vec{F}_{MAP}$$

$$4\pi\eta R\vec{v} > \mu_f (\chi_p - \chi_m) V_c \frac{\partial H_{ext}}{\partial x}^2$$

$$\vec{v} > \frac{\mu_f (\chi_p - \chi_m) V_c \frac{\partial H_{ext}}{\partial x}^2}{4\pi\eta R}$$

$$v_{M\_min} = \frac{\mu_f (\chi_p - \chi_m) V_c \frac{\partial H_{ext}}{\partial x}^2}{4\pi\eta R} \quad \textbf{3-4}$$

In contrast, when the flow rate is higher than a maximum velocity v_{max}, the cells will flow through a MAP or DEP microchamber without enough time for them to be deflected to the equilibrium position. A$\mathbf{F_{HD}}$ will take control over the $\mathbf{F_{DEP}}$ and $\mathbf{F_{MAP}}$, thus eliminate these forces from exerting on a cell in the separation process. Consequently, cells will be directed into their outlet without undergoing the DEP or MAP separation, thus influence the effectiveness of the device. The lateral flow velocity of cell in the DEP and MAP stage can be stated respectively by the following approximation:

For DEP,

$$v_{y\_DEP} = \frac{\varepsilon_m \varepsilon_0 R^2}{2\eta} Re[K(\omega)] \nabla \frac{\partial E^2}{\partial y} \quad \textbf{3-5}$$

For MAP,

$$v_{y\_MAP} = \frac{\mu_f (\chi_p - \chi_m) V_c \frac{\partial H_{ext}}{\partial y}^2}{4\pi\eta R} \quad \textbf{3-6}$$

To ensure that all cells reach their equilibrium positions under $\mathbf{F_{MAP}}$ and $\mathbf{F_{DEP}}$, Wang *et al.* (2014) has stated that the cell which located furthest from the equilibrium must be accounted for. The time for cells furthest from the equilibrium to reach their equilibrium position can be mathematical represented by:

$$\tau = \frac{w}{v_y} \quad \textbf{3-7}$$

where w is the width of channel. The time for cells exposed to a $\mathbf{F_{MAP}}$ or $\mathbf{F_{DEP}}$ is determined by (Wang *et al*., 2007):

$$\tau' = \frac{l}{v_{max}} \quad \textbf{3-8}$$

in which l is referred to the length of microchamber within the MAP stage (l_{stg1}) or DEP stage (l_{stg2}). For effective lateral positioning within proposed micro-device, Li *et al.* (2014) clarified that τ have to be lowered than τ' ($\tau<\tau'$):

$$\frac{w}{v_y} < \frac{l}{v_{max}} \quad \textbf{3-9}$$

By substituting Eq. (3-7) and Eq. (3-8) into both Eq. (3-4) and Eq. (3-5), the maximum flow velocity in DEP stage and MAP stage, respectively, can be written as:

$$v_{max\_DEP} = \frac{lR^2}{2w\eta}\varepsilon_m\varepsilon_0\, Re[K(\omega)]\nabla\frac{\partial E^2}{\partial y} \quad \textbf{3-10}$$

$$v_{max\_MAP} = \frac{l\,\mu_f\,(\chi_p - \chi_m)\,V_c\frac{\partial H_{ext}}{\partial y}^2}{4\pi\eta\, wR} \quad \textbf{3-11}$$

To allow sufficient cell capture by these forces, the parameter of flow velocity should be adapted to a certain range. This flow parameter can be stated quantitatively by the following approximation:

$$v_{min} < v_{opt} < v_{max} \quad \textbf{3-12}$$

whereby v_{opt} is referred to the range of optimum flow velocity, v_{min} is the minimum flow velocity and v_{max} is the maximum flow velocity. By relating Eq. (3-12) with the velocity formulation as discussed before, the ideal flow rate in cell capture application for DEP and MAP stage can be alluded respectively as:

DEP stage:

$$\frac{\varepsilon_m\varepsilon_0 R^2}{2\eta}\, Re[K(\omega)]\nabla\frac{\partial E^2}{\partial x} < v_{D\_opt} < \frac{lR^2}{2w\eta}\varepsilon_m\varepsilon_0\, Re[K(\omega)]\nabla\frac{\partial E^2}{\partial y} \quad \textbf{3-13}$$

MAP stage:

$$\frac{\mu_f\,(\chi_p-\chi_m)\,V_c\frac{\partial H_{ext}}{\partial x}^2}{4\pi\eta\, R} < v_{M\_opt} < \frac{l\,\mu_f\,(\chi_p-\chi_m)\,V_c\frac{\partial H_{ext}}{\partial y}^2}{4\pi\eta\, wR} \quad \textbf{3-14}$$

where v_{D_opt} is the optimum flow rate in DEP stage whereas v_{M_opt} is the optimum flow rate in MAP stage. From the equation above, both length and the width of a DEP or MAP microchamber are showed to be correlated with the maximum flow velocity of

cell. As such, the smaller the width, the higher the flow rate that can be flowed through the channel to ensure successful cell separation with high throughput. Due to the constraint of available micro-fabrication technique, the minimum allowed width of the channel will be fixed to 250μm. In order to capture the optimal volume of microfluidic channel without influencing the flow velocity and the microelectrode efficiency, the length of the microfluidic DEP and MAP chamber is suggested to be ranged in 15mm to 20mm respectively (Saliterman, 2006).

3.2.3 Electric field strength (DEP stage)

Because electrical field will be scaled down favourably at microscale, a high electric field can be generated using only a few volts within a DEP microchamber. A $\mathbf{F_{DEP}}$ will increase with the square of the applied electric field gradient, thus making larger input voltages desirable for cell separation. Notably, the application of external electric field on the living cell will cause a transmembrane voltage due to the accumulation of ions on the cell membrane surface (Gascoyne & Shim, 2014). The transmembrane voltage has been proven in literature to be proportional to the cell radius. For instances, cells of larger radii such as breast CTC can be electroporated at a smaller local field strength (Dimitrov, 1995). However, if the applied DEP voltage is too high for large cancer cells to be attracted toward an electrode edge with high field region, the transmembrane potential will result in ion leakage and electrodestruction (M. Toner & Irimia, 2005). Such a condition can lead to a loss of target cells as well as the reduction of cell viability in an isolation device. To prevent these problems, the electric field within a DEP microchamber need to be carefully adjusted. Besides, the isolation should be completed within a short duration after the sample processing starts. A study conducted by Gascoyne and Shim (2014) has suggested that the highest field region to which cells

are exposed shouldn't be more than $5x10^5$ Vm^{-1} and the exposure time to F_{DEP} shouldn't be more than 400s for blood cell separation.

3.2.4 Magnetic field strength (MAP stage)

Similar to $\mathbf{F_{DEP}}$, $\mathbf{F_{MAP}}$ is dependent on the magnetic field generated by the magnetic flux source, which are permanent magnets in this study. The total force exercised on a MAP microfluidic chamber can be calculated by integrating Eq. (2-17) over the volume of a magnet (Furiani, 2007):

$$\boldsymbol{F} = \int_s (\boldsymbol{M} \cdot \boldsymbol{B_o}) d\boldsymbol{S} \qquad \textbf{3-15}$$

where $\mathbf{B_0}$ is the magnetic field generated by permanent magnet, while $d\boldsymbol{S}$ is a vector in the surface normal direction, which modulus is equal to the area of d**S**. This expression has implied that the total magnetic force on MAP microchamber is determined by the surface magnetization (**M**) and the surface orientation of the magnet. More specifically, the magnetic field within the capture region falls off inversely with the square of the distance to the magnet and it can be represented as (Gassner *et al.*, 2009):

$$\boldsymbol{B}(y)\ \alpha \frac{\boldsymbol{B_0}}{(S+y)^2} \qquad \textbf{3-16}$$

where S is the thickness of the substrate, and y represents the distance between permanent magnet and the channel wall. This magnetic field has not only to induce a magnetic moment, but also to generate a magnetic gradient (which produces a magnetic force on the particle) in order to drive targeted cells apart from solution. To enable effective capture distance of the magnetic force, the distance of permanent magnet from

the middle line of microfluidic channel shouldn't be more than 10mm (Porcher, 2005). Meanwhile, for face-to-face permanent magnet, the magnet length (L_m) over inter-magnet gap ratio have to be equal or more than 1 (Zheng *et al.*, 2011). Aforesaid, enhancing $\mathbf{F_{MAP}}$ by increasing the magnetic field intensity can improve the cell capture rate. To achieve the field strength require for successful targeted cell capture, the magnetic field gradient within the microfluidic channel should not be less than $10T/m^2$ (Zhu *et al*., 2014)

3.2.5 Dilution ratio

As alluded in previous chapter, the massive numbers of blood cells (e.g. $5x10^6$ cells in each microliter of blood) will result in cell overlapping within a microchannel. Such a condition is undesirable in this study because it will prevent the device from precisely isolating target cells from a whole blood sample. To circumvent this problem, the blood samples are generally diluted with diluent before proceeding to bench top separation process (Mehmet; Toner & Irimia, 2008). Dilution reduces the concentration of blood cell per unit volume, thus allows for rapid detection of certain particles from dense colonies. The numbers of cells per volume concentration (with units such as cells/mL, cells/L) of diluted blood can be calculated by employing the equation as below (Fishel, 2010):

$$C_1V_1 = C_2V_2 \qquad \textbf{3-17}$$

whereby C represents the concentration and V is the sample volume. Their subscript indicates type of solution, such that 1 refers to the whole blood sample and 2 is the diluted blood solution.

Multiple studies have explored the effect of wide ranges of dilution on blood samples. A study conducted by Chen *et al*. (2012) has found lyses among white blood cells when the dilute ratio of whole blood to saline exceeds 1:11. This statement is in agreement with the result elucidated by Peter *et al.* in 1964. Their experiment has discovered that the blood plasma would undergo a significant change in water and protein concentration, when dilutions that are equalled or exceeded clinically. Consequently, the blood viscosity is reduced, following by an increasing size of blood cells, which further lead to cell lysis once it exceeds the cell's membrane viscoelasticity. Furthermore, very recently, a research group from Ghent University, Belgium, reported the dilution of whole blood sample greater than 1:10 would reduce the Fe isotopic composition within the RBC due to the increase of matrix elements such as Na and K (Anoshkina, Costas-Rodriguez, & Vanhaecke, 2015). Such a condition is not favourable in our study as it will greatly reduce the efficiency of MAP as a pre-enrichment stage to separate RBC cells from the blood sample. For the purpose of cell study on bench top device, the dilution ratio (whole blood: saline) of 1:10, as suggested by Anoshkina *et al.* (2015) will be employed. Beyond this point, study has reported the viscosity of these mixtures would remain similar to the undiluted blood and no changes is detected among the blood cells.

3.2.6 Material of microfluidic channel

There are a few factors to be considered when choosing a material for a microfluidic system: required function, and degree of integration. Since microfluidic channel is the basis in building a microchip, the ability of photonic interrogation of the sample is required. Therefore, the material chosen must be transparent to visible light. Besides, such a material should be biocompatible and will not react with the chemical properties of fluid flowing through it. Furthermore, the material should have high flexibility and

versatility during fabrication process. Notably, a study conducted by *Li et al.* (2014) has shown that large capillary forces which are detected within a microfluidic device as a result of integration of fluid movement and detection instrumentation will cause the microchannel wall substrate to swell, crack, or dissolve. Such a condition is undesirable as it may drive fluids into unwanted areas of the device, risking contamination of a fluid stream and dislocation of the cells (Car *et al.*, 2009; Li *et al*., 2014). As our device will feature continuous flow, therefore, it is important that the employed material must be able to withstand a maximum shear stress of a flow. In this case, a weak yield stress of a material will result deformation of a proposed microfluidic channel, following with dislocation motion of cells. In order to overcome the problem as well as to fulfil application of our device, quartz glass will be selected as material for construction of the channel or spacer which serves as the passage of fluid. Combination of this material with a deformable component such as polydimethylsiloxane (PDMS) can enable integration of microelectrodes and ferromagnetic into the channel.

3.2.7 Fabrication complexity

Although various microfabrication techniques are employed to process and fabricate the gasket, the complexity of microfluidic system can result in higher cost. This is because different channels depths and dimensions require a series of fabrication procedures which will involve sophisticated technologies. In this context, a microfluidic channel with rectangular cross-section is selected in our design due to the ease of fabrication. To prevent the microfluidic channel from collapsing during the fabrication process, its aspect ratio (height: width) should not be lower than 1:10 (Saias *et al.*, 2011). Besides, the minimum allowed width of the channel should be limited to approximately of 0.25mm to allow a sufficient margin for bonding (Saliterman, 2006).

3.2.8 Uniformity of flow

Finally, in our application, it is necessary to make sure that the flow velocity is as uniform as possible within a microfluidic channel. As a consequence of the inserting cell suspension through the inlet, the flowing of non-uniform fluid across the channel is major problem faced by lots of studies. Apart from that, any sedimentation of cell at particular point within microfluidic channel can exert influential impact on both MAP-DEP analysis. Thus, to ensure uniform loading capacity for a given chamber size, it is crucial that the whole area reaches saturation at the same time. In this case, cross-section of microfluidic channel should be increased and it will be further discussed later in this chapter.

3.3 Proposed Microfluidic Architecture

Figure 3.1 presents a structure of our proposed MAP-DEP based microfluidic interface. The overall design is configured in a way similar to that of the standard microscopic slide format, as such 78mm long and 25mm wide. This has enabled the entire device on a small glass slide to be placed on the size of a human palm, and therefore fulfil the fundamental need of a lab-on-a-chip.

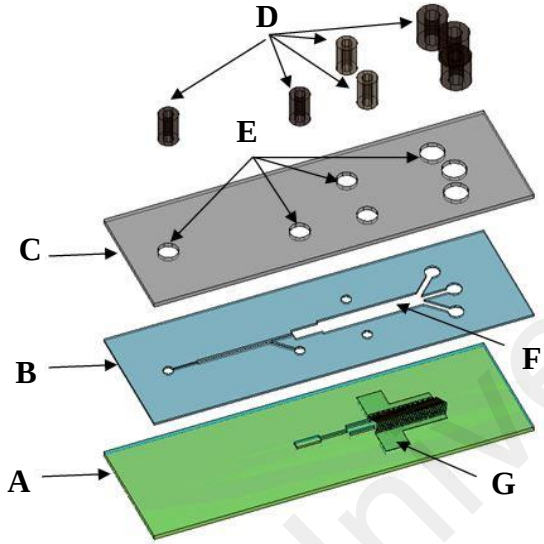

Table 3.1: Component Description

	Components	**Material**
A	Cover slip	Indium tin oxide
B	Spacer	glass
C	Bottom glass die with metal deposition	Polydimethylsiloxane (PDMS)
D	Rubber O-ring	-
E	Port interconnection	-
F	Separation chamber/microfluidic channel	-
G	Electroplated microelectrode	Ti_2O

Figure 3.1: Exploded basic structure of the proposed microfluidic platform.

As show in figure above, the microfluidic device consists of three important layers: bottom glass die, spacer and cover slip. In this embodiment, a planar microelectrode pattern will be deposited on the surface of a bottom glass slide through the standard photolithographic process. Followingly, the spacer with an imprinted microfluidic channel's mask design is bonded with the bottom glass die via plasma treatment. A cover slip will be placed over spacer to keep the cell sample intact during the experiment process. To provide inlet and outlet ports for microfluidic injection and ejection, a few holes are drilled in the cover slip. Noteworthy, the capillary tubing is typically use to interface the macroscale fluid delivery system to a microscale separation system. Therefore, the upper O-ring will be inserted into the cover slip holes to hold these tube firmly in place during experiments. In order to ease our computational study, the glass cover slip will be bonded to serve as the substrate or the "capture plane", with a negligible thickness. Here, a closed-up view of our proposed microfluidic channel employed for computational study is illustrated in Figure 3.2.

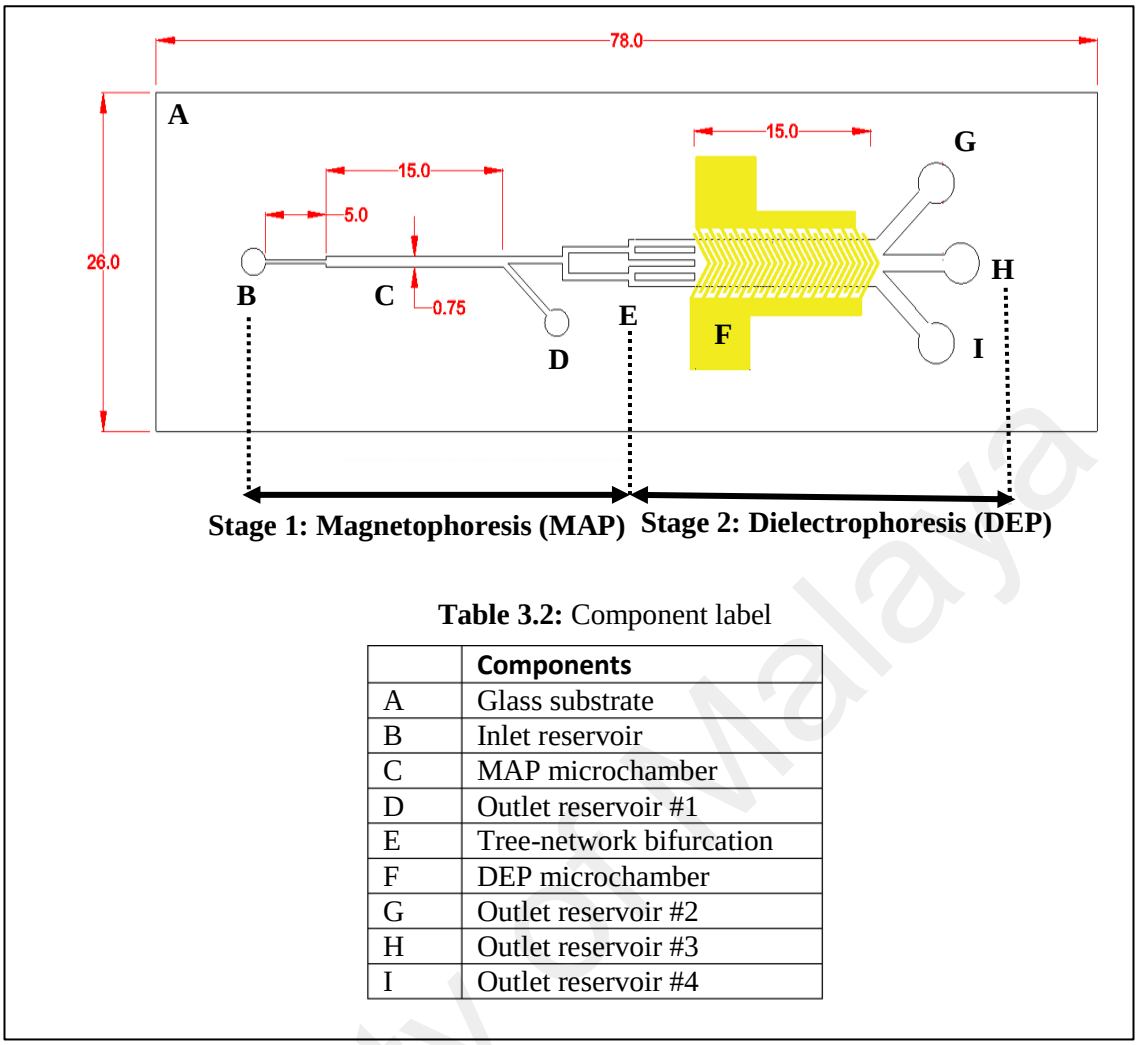

Table 3.2: Component label

	Components
A	Glass substrate
B	Inlet reservoir
C	MAP microchamber
D	Outlet reservoir #1
E	Tree-network bifurcation
F	DEP microchamber
G	Outlet reservoir #2
H	Outlet reservoir #3
I	Outlet reservoir #4

Figure 3.2: The layout of the design for a proposed MAP-DEP integrated device.

In Figure 3.2, the proposed microfluidic channel will support 2 microseparation processes, such that MAP separation in stage 1 follow by DEP separation in stage 2. For MAP stage, permanent magnets which are made of neodymium–iron-boron (Ne-F-B) featuring magnetic flux densities of 500mT will be employed to generate magnetic field over the MAP chamber. Meanwhile, in DEP stage, an array of interdigitated divergent-shape microelectrodes are embedded at the bottom of chamber. A metal contact, as presented in figure above, will connect them with an external sinusoidal electric potential to create an electric field for cell capture. Although the use of planar electrode able to increase surface area for reaction, a study conducted by Yafouz *et al.* (2015) shows that the cells would not homogeneously distributed over the electrodes. Such a

condition is undesirable as it will hinder our integrated micro-device from achieving its optimal performance. To ensure uniform loading capacity for a given chamber size, a tree-network bifurcation from our previous study (Low *et al*., 2014) is implemented into this proposed design (see Figure 3.2). The detailed architecture of this design will be further discussed in next chapter. When a suspension of blood sample spiked with CTCs is inserted into this system, the cells will enter the first stage through an inlet. A MAP force will be exhibited on these blood cells as they pass through the MAP microchamber. In the end of the MAP stage, red blood cells (RBCs) will be removed and collected in outlet 1. Concurrently, the enriched nucleated cells such as white blood cells (WBCs) and CTCs will be directed into DEP stage to undergo DEP force. This leads to a separation of CTCs from other nucleated cells. Depending on the dielectric properties of both CTCs and WBCs, they will be led toward their designated collection outlet in the end of DEP stage.

As alluded in previous section, the dimension of microfluidic channel is correlated with the distribution of electric, magnetic and hydrodynamic force. Therefore, these parameters should be incorporated into the course of this study to help developing a successful microchip device based on a force balance equation between DEP, MAP and hydrodynamic force. It has been reviewed in Chapter 2 that the electric field distribution within the channel will be decayed significantly at a height greater than 0.5mm. To achieve optimal sample processing volume as well as accommodate DEP stage requirement, the height of entire microfluidic channel will therefore be fixed at 5mm. As shown in Figure 3.2, the entrance length is set as 5mm. It is because a consistent flow profile is found to be quickly developed at this linear extent (Adams, Olson, & Rawlins, 2015). Meanwhile, the length of both MAP and DEP microchamber are assigned as 15mm respectively to accomplish the term of optimum sample volume and cell throughput (refer to Section 3.2.2).

Since both length and height of microchannel have been fixed, subsequently, a channel width will directly influence performance of our integrated device. In this case, a width of 0.75mm has been employed for the MAP microchamber of Stage 1. It is the allowed maximum value for an effective magnetic field to be distributed within the channel, providing that a permanent magnet is located on the side of MAP microchamber in our study . Meanwhile, in stage 2, the width of DEP microchamber will be regulated according to the width of output channel width from MAP stage (see Figure 3.2). Notably, the width of MAP output channel is determined in dependence of the cells' positions in the gradient. Thus, these dimensions will be decided based on the result of cell trajectory analysis in next chapter. Nevertheless, a microfluidic structure with height-to-width aspect ratio below 1: 10 (height: width) is prone to collapse (Zborowski *et al*., 2008). To avoid this issue, the width of the DEP chamber should not be more than 5mm (Friend & Yeo, 2010).

3.4 Design Development and Optimization

Apart from channel architecture, it is necessary to examine our proposed system's physic to enhance the separation of this integrated model. Our analysis will be focused on the MAP stage, whereby the evaluated properties include fundamental physics of cells, magnetic field distribution in MAP stage, and hydrodynamic force of the integrated platform. By assembling these parameters in algorithms, a separation can be tested and calibrated to achieve optimal recovery rate and throughput. They will be described in details in the following section.

3.4.1 Clausius-Mossotti (CM) factor

For the purpose of creating a physiological relevant microenvironment within the our microfluidic system, the factor that controlling behaviour of a cell under the MAP

and DEP force is needed to be understood by considering first how the imposed magnetic field and electric field affects the cell. In literature, the motility of the blood cells within the magnetic force have been defined Meanwhile, the DEP force exacted on a cells can be vary in space, depending on the applied frequency. Therefore, to determine the trajectories of blood cells within the electric field, a primitive model based on a blood sample that accounted for Clausius-Mossotti factor as a function of frequency will be computed.

Aforementioned, the Clausius-Mosotti (CM) factor is the key principle that determine strength and directional sign of a DEP force. It translates a difference in polarization between the cells itself and the medium in which it is suspended. Generally, the derivation of CM relation for these dielectric cells has been showed in Eq. (2-8) to Eq. (2-12). According to these equations, this factor is proved to be frequency dependence, as such different cell types will be discriminated on the basic of their crossover frequencies at the chosen suspending medium conductivity. Noted that a crossover frequency is the transition frequency point where the DEP force switches from pDEP to nDEP or vice versa. In this case, cells will be attracted to the high field regions and exhibit pDEP if the applied field frequency is higher than their crossover frequency. Meanwhile, for the nDEP, a cell is repelled from the high field regions on the array if an applied field frequency is lower than their cross-over frequency. However, if the crossover frequency for the two types of cells to be separated is close, separation may not be very effective. Therefore, a DEP frequency are needed to be properly selected to impose differential forces on cell types to be separated in accordance with the cell crossover frequencies at the chosen suspending medium conductivity. To assess the optimum frequency used to isolate CTCs from a blood sample, a plot of polarizability as a function of frequency will be presented in our study.

3.4.2 Permanent magnet orientation

As mentioned beforehand, the permanent magnet configuration will influence the magnetic force generated within a MAP microchamber. To obtain desirable cell separating configuration in our proposed MAP stage, it is important to employ a correct magnet orientation. For this purpose, the effect of various permanent magnet orientations on magnetic force distribution within a microfluidic channel will be examined and compared in this study. A single magnet configuration, two magnets placed in attraction, and two magnet placed in repulsion, have been considered respectively, as depicted in Figure 3.3. For instance, Figure 3.3(a) illustrates the single permanent magnet configuration. A permanent magnet is aligned in the way whereby the direction of the field is parallel with the direction of the fluid flow within the microchannel. Meanwhile, for face-to-face magnet configuration, the microchannel will be surrounded by two permanent magnets. These magnets are placed in north-to-south (attractive) and north-to-north (repulsive) orientation. They are showed in Figure 3.3(B) and Figure 3.3(C), respectively. In this study, the distance of permanent magnet from the microchannel wall will be fixed at 5mm, which is a half of maximum allowed value for all configuration. Nevertheless, to ease fabrication process as well as to balance the magnetic forces, permanent magnets used in our study has axial symmetry.

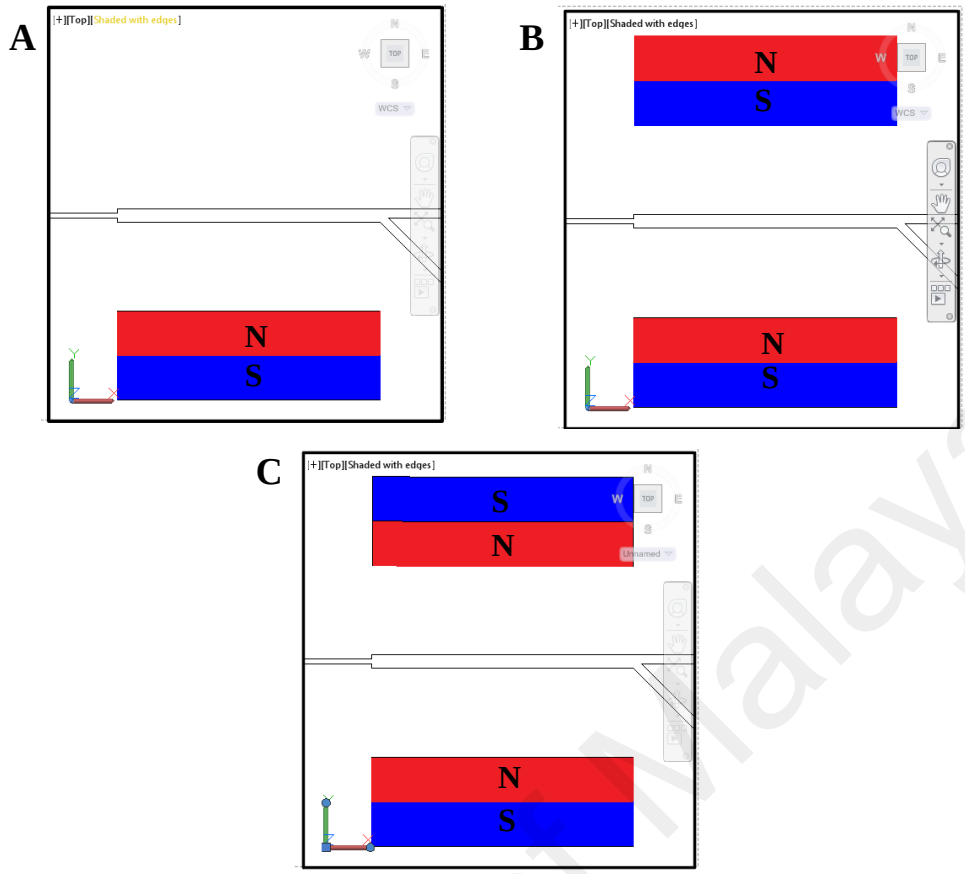

Figure 3.3: Schematic of microfluidic channel with its magnet: (A) Conventional imbedded permanent magnet configuration; Face-to-face permanent magnet in (B) attractive and (C) repulsive configuration.

3.4.3 Magnetic field gradient of the ferromagnetic track

Notably, the used of ferromagnetic track coupled with permanent magnet can concentrate the magnetic field over the confined space of a microfluidic channel, thus produce a force to efficiently separate targeted cell under a continuous flow**.** However, majority of the available ferromagnetic track design were proved their effectiveness in cell separation for a microfluidic channel which was less than or equal to 100µm wide (Jung & Han, 2008; Shen *et al.*, 2012). As a channel dimension will contribute to our device throughput, the range of width used for MAP microchamber in previous study is too small for our system. Such a condition will result in a longer time needed to process one sample. To solve this problem, a ferromagnetic track is proposed to be embedded in the middle of MAP microchamber. The design can be showed in Figure 3.4. A magnetic

field generated within the MAP chamber with the presence of ferromagnetic track will be examined in this study.

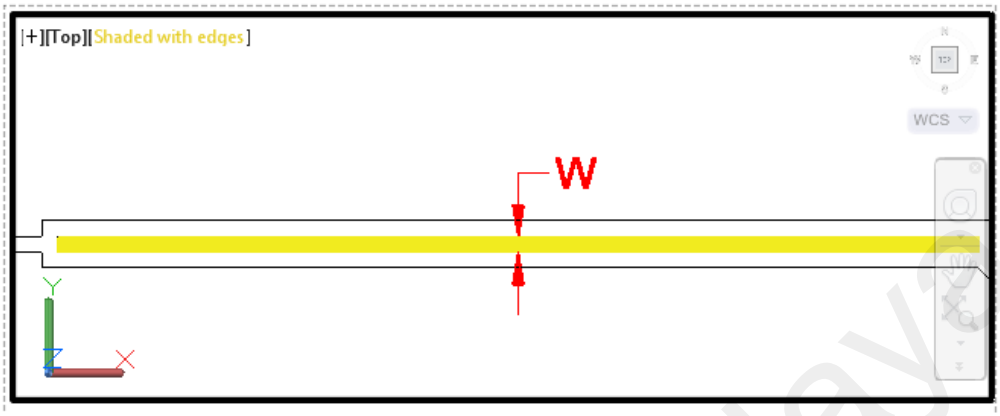

Figure 3.4: Schematic of ferromagnetic track (represented with yellow segment) within a MAP microchamber.

Notably, a study conducted by Chen *et al.* (2014) has reported a correlation between the cross-sectional area of a ferromagnetic track and the magnetic field. An equation was formulated based on the experimental observation, as such:

$$B_0 = \frac{9\mu_0\eta}{R_c^2\Delta\chi_c} \times \frac{H \cdot FR}{W \cdot L} \times \frac{1}{(S+W)^{-4} - S^{-4}} \qquad \textbf{3-18}$$

whereby FR represents flow rate. W, H and L is referred to width, height and length of microfluidic channel, respectively. Meanwhile, S is the cross sectional area of ferromagnetic track. Since both the length and height of the magnet track will be accommodate according to those of the MAP microchamber, therefore, this equation has implied that the magnetic field is inversely proportional with the width of magnetic track. The reason for such a phenomena is that the increasing width of magnet track has resulted a larger surface area for the magnetic flux line to travel through it. Since **B** at a field point is produced by the time derivative of magnetic field flux through a surface, the increase of magnetic track's width will prolong the travel time of magnetic flux thus

reduce **B** (Andreu *et al.*, 2012). In this case, a very strong field can be created over small distances and small displacements on the scale of ferromagnetic track. To obtain an effective F_{MAP} in our proposed microfluidic architecture, the width of ferromagnetic track will be fixed at the allowed minimum fabrication value, which is 250μm wide.

3.4.4 Hydrodynamic mechanism

Apart of magnetic field and electric field distribution, it should be noted that the effectiveness of our proposed MAP-DEP microdevice is depended on the hydrodynamic force subjected within the microsystem. To produce a particular output response at the drain-outlets ports, the flow requirements as mentioned earlier in this chapter (Section 3.2) are needed to be fulfilled. A velocity profile and dynamic pressure generated within a proposed channel topology will therefore be examined. Notably, the hydrodynamic mechanism is depended on a channel geometry. In this context, a flow rate can be optimised by tailoring the proposed geometry.

3.4.5 Separation efficiency

For benchtop CTC's detection device, it is necessary to analyse and optimize the devices' performance before they are employed in an experimental setup. To evaluate the proposed isolation technology, the capture efficiency (or recovery rate) will be measured in our numerical study.

A capture efficiency refers to the fraction of captured target cells relative to the total captured cells. It is usually expressed as a percentage (%). This measurement is important in accessing the total of target cells which has been lost in the isolation process. A high capture efficiency represents less cell losses and thus provides clinician accurate information about the amount of target cells discovered from a given sample (Jin *et al*., 2012)

In our study, an early-stage assessment of MAP operational performance will first be conducted to investigate its recovery metrics as well as cell separation dynamics. Following this, the analysis of our finalised integrated platform's functionality is conducted to ensure the compatibility of a proposed MAP stage in DEP application.

3.4.6 Whole blood vs. dilution ratio 1:10

On a side note, majority of microfluidic techniques demonstrate a dramatic reduction in capture efficiency when whole blood sample is employed. Therefore, the blood sample is typically diluted with saline solution before it is injected into an isolation microfluidic device. It should be noted that a dilution would reduce the concentration of cells carried by fluid flow toward MAP and DEP chamber. Under a constant velocity field, a sample with high dilution ratio will reduce in a lower throughput in contrast to the low-dilution-ratio sample (Fishel, 2010). To gain insight on the correlation between dilution ratio on the device's separation efficiency, the particle tracing simulation will be conducted. In favour of this simulation, two dilution ratio proportion (whole blood: saline) such as 1:0 and 1:10 are used with constant concentration of saline. As the MAP microchamber will handle highly concentrated cells, the evaluation of performance metrics is focused on this stage. The target cells obtained from a sample with the corresponding dilution ratio across the optimised flow velocity will be observed.

3.5 Computational Modelling Method

The computational fluid dynamics method was conducted using the finite analysis package COMSOL Multiphysic 4.4® (COMSOL Inc., Palo Alto, USA). It is a modelling software which consists of advanced physical simulation platform as well as visualization tools to treat fluid structure interaction within our microfluidic architecture. It was used to perform numerical methods with a primary focus on MAP and DEP equation for both 2D and 3D design in our study. The aim of 2D modelling is to validate the forces within the proposed microchannel, while the 3D modelling is employed to compute particle trajectory. To perform the numerical analysis, several assumptions as written below were made:

i. The fluid injected at the inlet channel is non-Newtonian, whereby the viscous stress arises from a flow is linearly at every point.
ii. Cells are spherical.
iii. The flow within the microfluidic is incompressible such that it has constant density, viscosity and concentration.
iv. As the cross sectional of the microchannel is less than $1mm^3$, the Reynolds generated within the fluid flow will be less than 200. Therefore, the flow is considered as laminar.
v. The blood is treated with ethylenediaminetetraacetic acid (EDTA) such that blood clot would not form within the sample
vi. Both surrounding medium and system are considered to have uniform bulk conductivities, dielectric constants, and magnetic permeability. Hence no space charge with the system
vii. The fluid has constant electric conductivity and magnetic permeability.

viii. Constant magnetic field gradient is generated across the fluid volume in the MAP stage. The electric conductivity is negligible in this stage.

ix. The magnetization of the cells are collinear with the magnetic field.

x. The presence of non-magnetic cell will not distort the magnetic field lines in the MAP stage

xi. Joule heating and electrochemical effects are assumed negligible in DEP stage. This is because the electric field is low and frequency is high.

xii. Cells will flow according to the fluid stream. They do not stick to the boundaries.

Aforementioned, 2D and 3D simulation will be investigated in this study. Prior to generating these model, the CAD model of the microfluidic architecture was created. It was performed by using AutoCAD® 2013(Autodesk Inc., USA) due to its ability to generate complicated designs and its compatibility with COMSOL Multiphysic. The design geometry was then be imported into the COMSOL model library. Notably, in order to generate the 3D model, the desired workplane needed to first be indicated before the imported 3-D geometry was located on it. Subsequently, the 2-D cross section layout was extruded in Z direction to form a 3-D structure with 0.5mm height. After completing the geometry for our proposed model, the material of the domains will be defined accordingly to Table 3.1. The property function of each material was complemented by the COMSOL Material Library.

In COMSOL model builder, a complex system of points was presented to highlight the stress levels of a particular area. Generally, regions which normally have higher node density receive large amounts of stress compared to those with lesser node density. Generation of mesh happened when these points were connected according to the nodal point number. It was programmed to define the flow simulation properties within the

microfluidic channel. To avoid inverted mesh elements, the size of mesh needed to be very fine around the region where remeshing occurs (such as the curved region of the channel). This can be accomplished by using "Free Mesh Parameters", whereby the size of mesh was set to predefined. To obtain an accurate solution with a mesh that is sufficiently dense and not overly demanding of computing resources, a "Convergence Study" was performed using "Physic Induced Sequence Setting". The results are found to converge satisfactorily when a maximum element size of 5e-5 is stipulated for the fluidic channel subdomain. The resulting mesh can been seen in Figure 3.5.

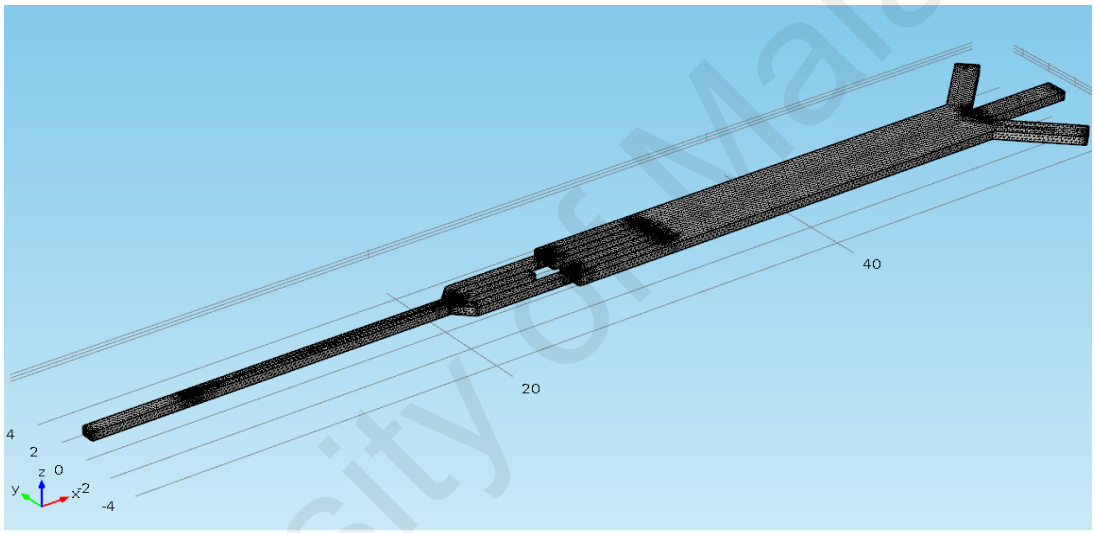

Figure 3.5: Mesh Generation in a 3D model.

Followingly, the finite element method analysis was implemented using three main modules, including: magnetic field modules, electric field module and Navier-Stokes Module. In order to derive forces from various parameters, the same procedure was repeated to generate the output from these modules. Once the whole problem was solved, the numerical data obtained from the magnetic field (H, M,$\frac{\partial H}{\partial X}$, $\frac{\partial H}{\partial Y}$, $\frac{\partial H}{\partial Z}$) and electric field simulation (E, $\frac{\partial E}{\partial X}$, $\frac{\partial E}{\partial Y}$, $\frac{\partial E}{\partial Z}$) was taken as input for the particle tracing module to generate cell trajectory within the proposed microchannel. To depict the individual cell movement corresponding to the derived forces' expression, the

individual cell properties (e.g. radius, charge, density) and its initial velocity was defined in this module. The simulation strategy and the boundary condition set for each module will be described further in the following subsection. A detailed flow chart of the modelling approach for the proposed micro-device is depicted in Figure 3.6.

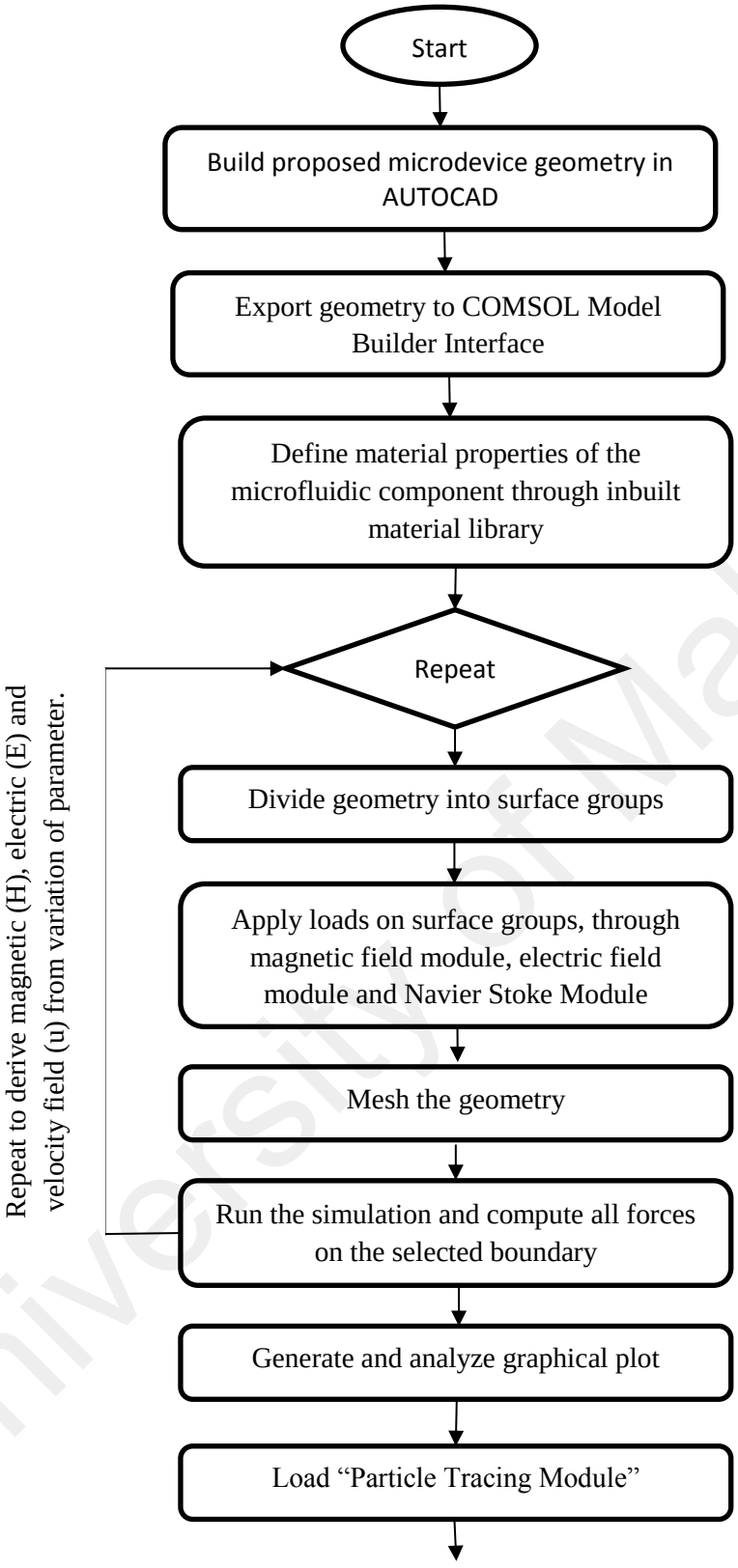

Figure 3.6: Detailed flow chart of simulation approach.

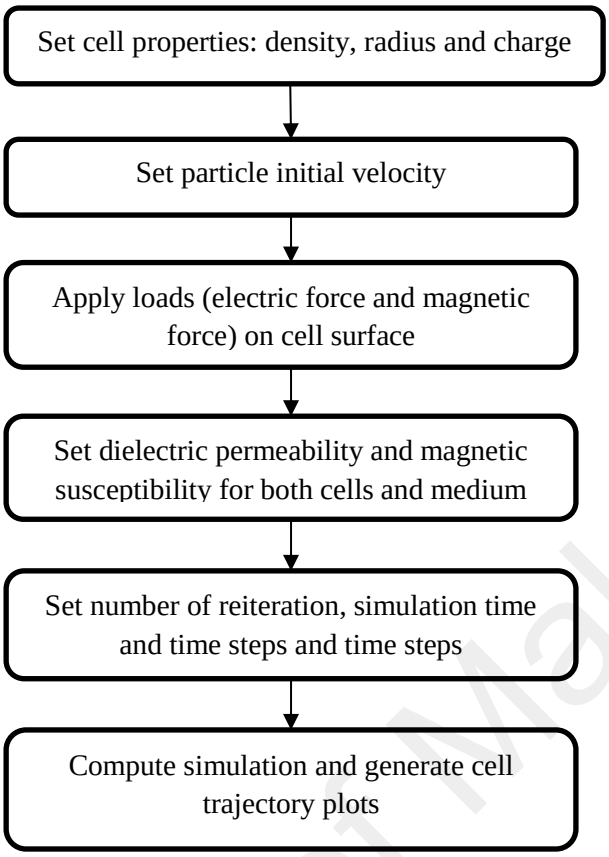

Figure 3.6, continue

3.5.1 Magnetic field module

The magnetic field module was used to model the force in MAP stage. In the magnetostatic simulation, the magnetic field with no current module was loaded. The heart of formulae for the analysis of the magnetic system is the Maxwell equation. The equation is written as below (Pryor, 2011):

$$\nabla \times (\mu_0^{-1}\mu_r^{-1}\nabla \times \mathbf{A} - \boldsymbol{B_r}) - \boldsymbol{J^e} + \sigma\frac{\Delta \mathrm{V}}{\mathrm{L}} = 0 \qquad \textbf{3-19}$$

This formulation was applied across the quadratic Lagrange elements, where σ is the conductivity, μ_0 is magnetic permeability in a vacuum, μ_r is relative magnetic permeability, $\boldsymbol{A}$ is the magnetic vector potential, $\boldsymbol{J^e}$ is an externally generated magnetic

current density, B_r is the remanent magnetic flux density, ∇V is the potential difference, and L is the distance. Once the global governing equations have been applied, the constitute relation of the permanent magnet as well as the MAP microfluidic chamber was defined.

In the subdomain setting, the permanent magnet was modelled as body with magnetization uniformly directed toward the MAP microchamber. Its constitutive relation is designated as (Andreu *et al.*, 2012):

$$\boldsymbol{B} = \mu_0 \mu_r \boldsymbol{H} + \boldsymbol{B_r} \quad \textbf{3-20}$$

where the permeability of free space, μ_0 is equalled to $4\pi \times 10^{-7} NA^{-2}$. A magnetic field (***B***), defined by the remanent flux density (***Br***) is stipulated as 500mT. The magnetic permeability of the simulated permanent magnet is provided accordingly to standard manufacturer's datasheets such that μ_r is 1.05 (Association, 2014). Meanwhile, for MAP microchamber, the constitutive relation is denoted as:

$$\boldsymbol{B} = \mu_0(\boldsymbol{H} + \boldsymbol{M}) \quad \textbf{3-21}$$

The resulting magnetization within the microchamber, ***M***, will depend on the magnetic susceptibility volume of blood (refer to Eq. (2-14)). It should be noted that a soft element of NiFe will be imbedded within the MAP microchamber to enhance the magnet field. It can be modelled by imposing the magnetization response as arbitrary **M(H)** relation in the subdomain settings.

Notably, the magnetic analysis needs a larger (open) domain because the field extends to infinity. A large number of computational nodes are therefore required to

achieve accurate magnetic force values, which has resulted an increase in computation time and inhibited large-scale parametric analysis. To allow the magnetic field to have a proper distribution in the surrounding space, a closed-form magnetic analysis was used. An environment was drawn enfolding the whole device with few boundary condition as below:

i. A symmetry boundary was set on the xz plane in accordance to y=0.25, along the midline of the microchamber.

ii. The boundary conditions on the interior boundaries are set by default to continuity, as such:

$$\boldsymbol{n} \times (\boldsymbol{H_1} - \boldsymbol{H_2}) = \mathbf{0} \qquad \textbf{3-22}$$

where **H** indicates a magnetic field. Meanwhile, a magnetic insulation was set on the external boundaries of the environment, except for the symmetry point in which a zero potential condition is implied. Such a setting able to enhance computational power since the y=0.25 plane is characterised by either magnetic field maxima or minima for symmetry reasons while other external boundaries which are drawn further from the field source would have a null magnetic field.

The problem was then solved for the total potentials to a relative tolerance of 1E-06 using the PARDISO direct solver. Notably, to calculate MAP force within the microchamber, it is important to generate a correct expression for mapping results on Lagrange elements of magnetic field. It can be achieved by computing the derivative of magnetic field from the stored numerical data with "coefficients of PDE" setting. In order to take the values from previous solution, the feature "Values of variables not solved for" needed to be chose (as illustrated in Figure 3.7).

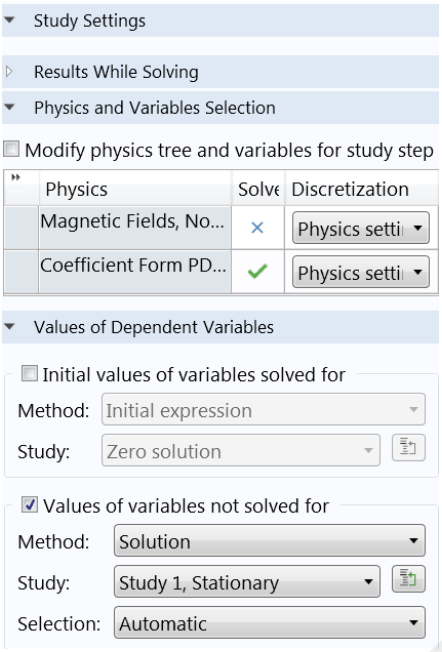

Figure 3.7: Definition of study steps.

Concerning the PDE setting, an equation with the following term is created (Pryor, 2011):

$$a\boldsymbol{u} = \boldsymbol{f} \qquad \textbf{3-23}$$

where a=1, **u** is the vector field and **f** represents the components of magnetic field. To establish this formulation, all coefficients other than a and **f** as illustrated in Figure 3.8 is set to 0. The new variable for **u** can be directly related to the components of magnetic field vector obtained from previous section, such that:

$$\boldsymbol{u}=[mfnc.Hx,\ mfnc.Hy,mfnc.Hz]4^{T} \qquad \textbf{3-24}$$

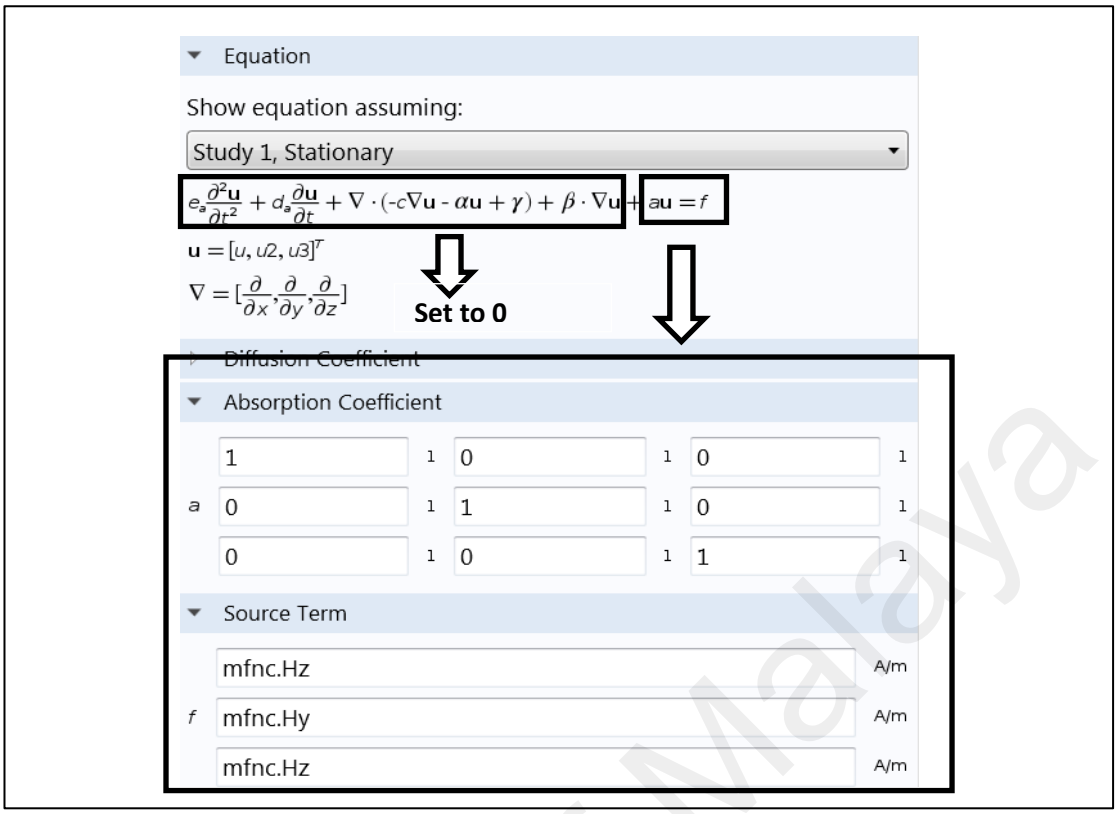

Figure 3.8: Definition of PDE setting**.**

Once the study was performed, the magnetic force was then computed by appending the numerical data of spatial magnetic field into the derived expression as stated in Eq. (2-20). To generate sufficient magnetic force to separate RBC, the graphical and quantitative analysis of magnetic field distribution for different permanent magnet orientation (as illustrated in Figure 3.3) as well as various microchamber width was performed in this study.

3.5.2 Electric field module

The electric current interface was used to model the DEP stage, whereby the magnetic-inductive effects was neglected in this stage and only resistive-conductive and electric-capacitive effects were accounted for. In this simulation, the electric potential in microchannel is governed by Laplace's equation of continuity such that (Lu *et al.*, 2008):

$$-\nabla \cdot ((\sigma + j\omega\varepsilon_r\varepsilon_o)\nabla\varphi) = 0 \quad \textbf{3-25}$$

where σ represents the electrical conductivity of the cell, ω is the angular frequency of the driving field, $\emptyset$ is the electric potential, ε_r is the relative permittivity of the medium and ε_o is the relative permeability of the vacuum. By solving this equation, the electric field generated by the microelectrode, **E** and the displacement of currents, **D** can be obtained, as such (Pryor, 2011):

$$\boldsymbol{E} = \nabla\varphi \quad \textbf{3-26}$$

$$\boldsymbol{D} = \varepsilon_r\varepsilon_o\boldsymbol{E} \quad \textbf{3-27}$$

Few boundary condition was set as following:

i. Electrodes are assumed to be isopotential, thus their thickness and height is neglected in electric field simulation.

ii. The voltage is defined as a sine wave at a particular frequency, whereby an electric potentials of +15V and -15V are assigned across alternating electrodes embedded within the microchannel. A non-uniform electric field will be established either vertically or laterally, depending on the microelectrode configuration.

iii. The other external boundaries were set to be electrical insulated, such that:

$$\boldsymbol{n} \cdot \boldsymbol{J} = 0 \quad \textbf{3-28}$$

where $\boldsymbol{J}$ is the current density. However, for the boundaries that representing the electrode gaps, imposing an insulation condition will result in a mathematical singularity due to the competing Neumann and Dirichlet conditions. To solve this problem, the Neumann condition inside the gaps is changed by a Dirichlet condition, imposing the voltage to linearly vary between the values assumed at two subsequent electrodes.

iv. For the interfaces between the cell surface and the medium, the continuity of the electric displacement (**D**), electric field (**E**), and current density (**J**) are designated according to (Jones, 2003):

$$\boldsymbol{n} \cdot (\boldsymbol{D_1} - \boldsymbol{D_2}) = \boldsymbol{\rho_s} \quad \textbf{3-29}$$

$$\boldsymbol{n} \cdot (\boldsymbol{E_1} - \boldsymbol{E_2}) = 0 \quad \textbf{3-30}$$

$$\boldsymbol{n} \cdot (\boldsymbol{J_1} - \boldsymbol{J_2}) = 0 \quad \textbf{3-31}$$

where $\boldsymbol{\rho_s}$ is the surface charge density. Meanwhile, its boundary conditions from the continuity of potential and the conservation of charge at boundary can be written as:

$$V_i\,(r_i) = V_{i+1}\,(r_{i+1}) \quad \textbf{3-32}$$

$$\varepsilon_i \frac{dV_i}{dr} = \varepsilon_{i+1} \frac{dV_{i+1}}{dr} \quad \textbf{3-33}$$

where i represents region of the cell, such that nucleus as cell cytoplasm as region 1 and blood medium as region 2. The effect of the frequency on RBC, WBC, platelet and tumour cell was investigated.

The problem was solved using PARDISO direct solver with a relative tolerance of 10^{-6}. As akin with magnetic field module, the DEP force can be obtained by computing the derivative of electric field from the stored numerical data with "coefficients of PDE" setting. The new variable for **u** in Eq. (3-24) can be directly related to the components of electric field vector, such that:

$$\boldsymbol{u}=[ec.Ex,\ ec.Ey, ec.Ez]^T \qquad \textbf{3-34}$$

Once the study was performed, the DEP force was computed by appending the numerical data of spatial electric field into the derived expression as stated in Eq. (2-7) . Subsequently, the graphical plots were computed to investigate the electric field distribution of impedance measurement.

3.5.3 Navier-Stokes module

To direct the fluid flow into the proposed micro-device, the incompressible Navier-Stokes module was loaded. As suggested by the name, this module is governed by Navier-Stokes Equation, as such (Mortensen, Okkels, & Bruus, 2005):

$$\rho\frac{\partial \boldsymbol{v}}{\partial t} - \nabla\cdot\sigma + \rho\boldsymbol{u}\cdot\nabla\boldsymbol{u} = \boldsymbol{F} \qquad \textbf{3-35}$$

In this equation, **u** is the velocity vector containing u and v components along x, y and z direction. Meanwhile, ρ is the fluid's density, p is the flow's pressure and σ represents

the total stress tensor of Newtonian fluid which consists of the pressure stress and viscous stress. σ can be further expanded into (Pryor, 2011):

$$\sigma = -p\boldsymbol{I} + \eta\,(\nabla \boldsymbol{u} + (\nabla \boldsymbol{u})^T) \qquad \textbf{3-36}$$

where **I** is the identity matrix, and η represents the dynamic viscosity of the fluid. To fully describe the fluid flow, a statement of the conservation of mass is necessary. Considering both ρ and η is constant throughout the fluid, a mass continuity equation can be formulated such that:

$$\nabla^2 \boldsymbol{u} = \nabla p \qquad \textbf{3-37}$$

$$\nabla \cdot \boldsymbol{u} = 0 \qquad \textbf{3-38}$$

Note that only the fluidic channel was active in this mode whereby its subdomain settings internally specified for blood. Both inlet and outlet ports of the microchannel were defined at the beginning of MAP and end DEP stage, respectively. The boundary conditions for Incompressible Navier-Stokes were summarised as following:

i. No slip boundary conditions are used at wall whereby the velocity generate at the channel wall is zero.

$$\boldsymbol{u} = 0 \qquad \textbf{3-39}$$

ii. The inlet is provided with inflow boundary condition of velocity. A constant velocity will be generated at the input port as such

$$\boldsymbol{u = u_0} \qquad \textbf{3-40}$$

$\mathbf{u_0}$ is specified accordingly to the total length of microfluidic channel.

iii. The outlet boundary condition is considered with the mass flux adjusted to satisfy the continuity equation (Eq. (3-38)), such that the direction of mass flow is principally determined by the pressure inside the outlet boundary. Therefore, the pressure generated on the outlet, which served as a reference pressure for the incompressible flow is equal to zero.

Fluid simulation was carried out and the governing equations were solved numerically. The model surface plot which showed the velocity magnitude was generated. In order to study the fluid distribution within the chamber, the velocity field fluctuation in the middle of MAP microchamber as well as DEP microchamber was evaluated. The best design of microfluidic channel used for our proposed system was concluded.

3.5.4 Particle Tracing Module

To monitor the device functionality, the cell trajectory within both the MAP and DEP stage were computed using Particle Tracing Module. This module calculated the trajectory of cells, which were suspended in the blood sample, as they moved through our proposed device by solving the equation of motion for each set of cells. The equation is governed by Newton's second law such that (Tabatabaian, 2014):

$$m\frac{d\boldsymbol{v}}{dt} = \boldsymbol{F_c} \qquad \textbf{3-41}$$

where m is the mass of cells, **v** is the cell velocity and $\boldsymbol{F_c}$is a total force experienced by the cells. By considering a cell to be located at a position x(t) in a fluid, its position vector can be written as:

$$\frac{dX(t)}{dt} = \boldsymbol{v} \qquad \textbf{3-42}$$

in which the velocity of the particle, v can be obtained by integrating the Eq. (3-42). Taking the initial condition for the particle velocity as stationary and located at position vector $x(t_0)$, the equation for position vector can be rewritten as:

$$x(t) = (\frac{\boldsymbol{F_c}}{m})t^2 + v_o t + x_o \qquad \textbf{3-43}$$

Via Eq. (3-43), the cell trajectory can be traced by iteratively updating the position according to the flow field and the forces that imposed on cell.

Notably, the resulting force acting on the cells composed of four main components: hydrodynamic force ($\boldsymbol{F_{HYD}}$), which is caused by the resistance to the motion of a cell; MAP force ($\boldsymbol{F_{MAP}}$), which is caused by the non-uniform magnetic field; DEP force ($\boldsymbol{F_{DEP}}$), which is due to non-uniform electric field, and Brownian force (Kawano & Watarai, 2012), which is responsible for the random motion of cells resulting from the collisions with the fast-moves molecules of the fluid. The equalities of these forces can be expressed as following:

$$\boldsymbol{F} = \boldsymbol{F_{MAP}} + \boldsymbol{F_{DEP}} + \boldsymbol{F_{HYD}} + \boldsymbol{\zeta}\sqrt{\frac{12\pi k_b \mu T r_c}{\Delta t}} \qquad \textbf{3-44}$$

where ζ is a unit-variance-independent Gaussian random numbers and k_b refers to the Boltzmann constant (1.38065×10^{-23} J/K) (Tabatabaian, 2014). In this equation, the formulation for the first three terms had been discussed in Chapter 2. Meanwhile, for the Brownian force (which is represented by the forth term), its amplitude is depended on the fluid temperature (T) and the radius of the cell (r_c). As the equations for these force vector have already been embedded in this module, the theoretical trajectory of cells can automatically be computed according to the post-processing data obtained from Magnetic Field Module, Electric Field Module and Navier Stokes Module, respectively.

In order to perform the particle motion model, the following variables were defined:

i. The fluid within the microchannel is the only active subdomain.

ii. The cell properties such as diameter, density, magnetic susceptibility and electric permeability will be designated accordingly to Table 2.1.

iii. A **release** node is used to set the initial position and release times of the cells. They are selected to be released at 0s from the microdevice inlet. Override Properties feature is used to define an inlet with multiple particles types. The total time for the cells to migrate in the channel was set to 3600s, which provided smooth particle trajectories. A density-based is chose such that the number of particle will be released from a set of positions determined by a selection of geometric entities in the mesh.

iv. The **Bounce** option is selected as the wall condition to trace the microscopic cells in a fluid. The cells will reflects from the wall and its momentum can be conserved.

v. A **Freeze** option is selected as the outlet condition whereby the particle position and velocity is fixed at the instant the outlet boundary is struck.

Followingly, the Mathematical Particle Tracing interface will simulate the particle motion in Lagrangian reference frame. Particle trajectory plot for the MAP stage and DEP stage will be generated. The cell count obtained at each outlet was evaluated by selecting the predefined expressions (*cpt. Nsel*) under particle statistics, as illustrated in Figure 3.9. A global evaluation node will display the value of expression in a results table.

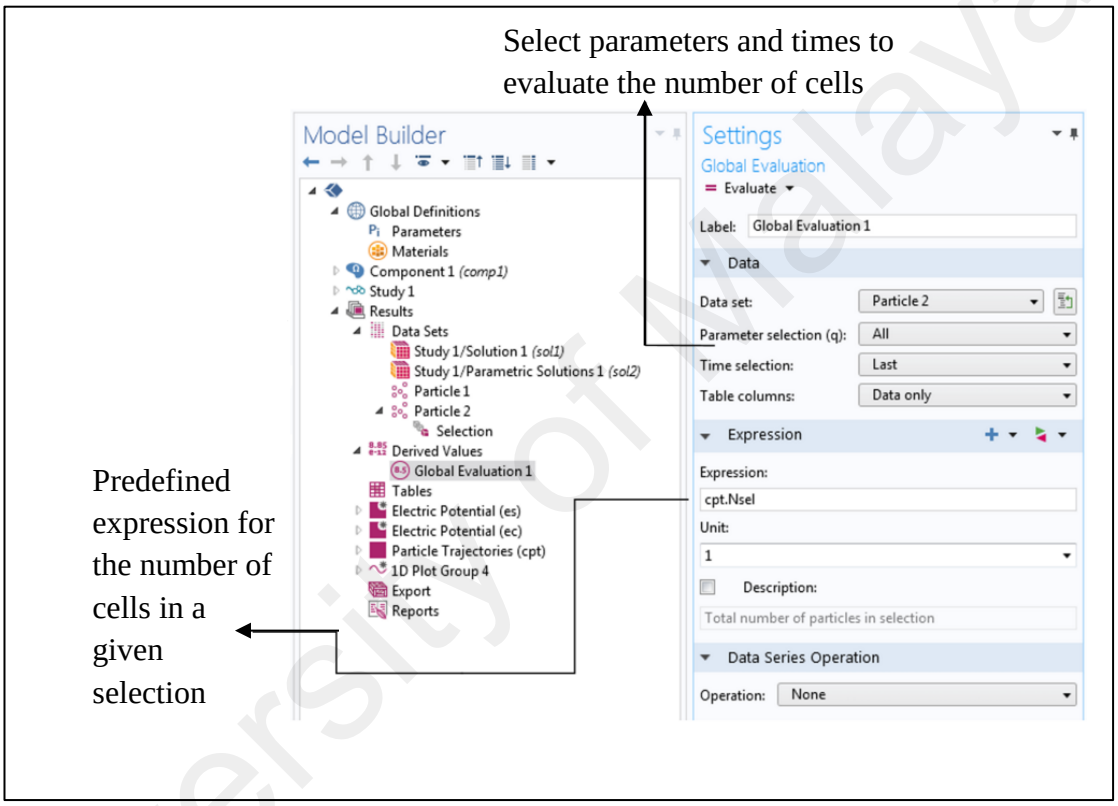

Figure 3.9: Evaluating the cell count in a specific outlet selection.

CHAPTER 4:

RESULTS AND DISCUSSIONS

This chapter encompasses the outcome of the proposed microfluidic system design development. The actual dimensional of the microfluidic device is reported and their CFD models are developed through COMSOL Multiphysics. There are three main issues to be highlighted in this chapter, as such physical model of cells (Section 4.1), the development of magnetophoresis stage (Section 4.2) and evaluation of overall performance of integrated MAP and DEP platform (Section 4.3). For instance, in section 4.1, the forces that act on blood cell will be analysed individually. Since our study emphasizes on how the MAP system able to enhance the DEP device performance by acting as a pre-enrichment stage, in section 4.2, the analysis of the result is obtained for magnetic field and velocity field fluctuation within the proposed MAP microchamber. The results are mainly presented in 3 forms – surface plot, surface arrow plot and line graph. Besides, in-depth explanation of how the use of an inbuilt magnetic track able to enhance magnetic field distribution within the microfluidic channel thus improve the separation efficiency of MAP stage will be discussed. The optimized design of MAP stage for our study is outlined in this section too. As for Section 4.3, it is about the performance evaluation of micro-device when our finalized MAP stage is combined with a DEP stage. Finally, the chapter comes to an end by proposing a final integrated platform and drawing a comparison between this study design and DEP platform proposed by previous study.

4.1 Physical model of blood cell (CM factor)

The calculated Clausius-Mossotti (CM) factor for blood cells and cancer cells over a distribution between 1kHz to 1GHz within a whole blood sample is demonstrated in Figure 4.1. This plot is generated with MATLAB, using a multiple-shell model equation

(Eq. (2-10)) with the parameters described in Table 2.1. The conductivity and permittivity of the whole blood sample is given as 0.76 S/m and 78, respectively (Vykoukal, Gascoyne, & Vykoukal, 2009).

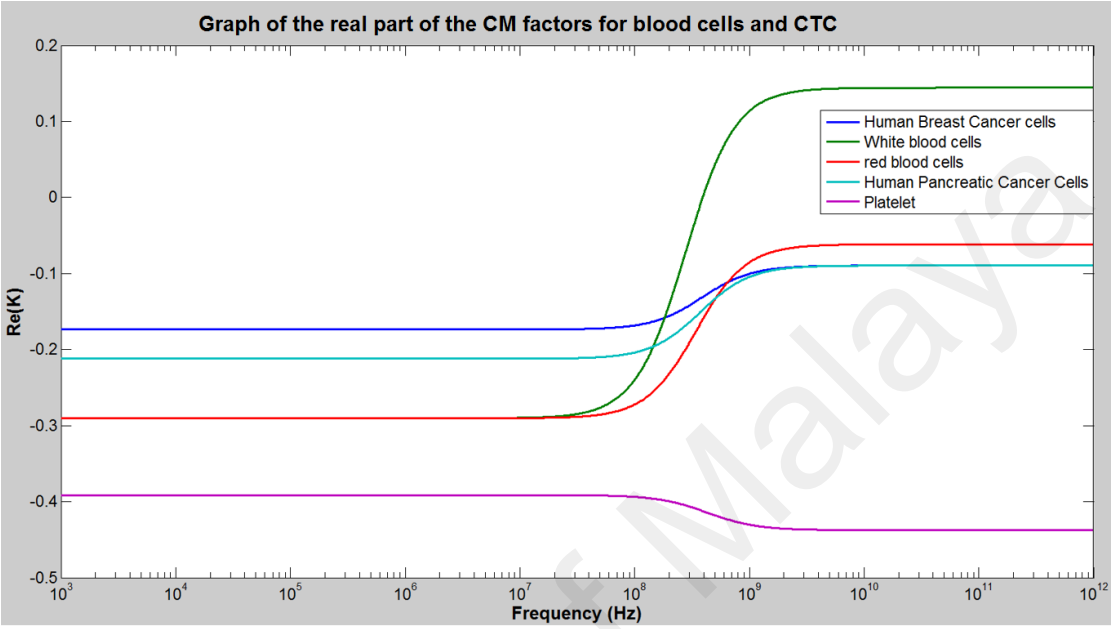

Figure 4.1: Real part of Clausius-Mosotti (CM) factor for human breast cancer cells, human pancreatic cancer cells, WBC and RBC in whole blood sample with a conductivity of 0.76 S/m, using multiple-shell model with the parameters described in Table 2.1.

Several features are apparent according to figure above. Firstly, the polarizability of a cell as the function of CM factor is strongly affected by its internal compartment properties. Since blood is a high conductive medium, at frequency less than 100MHz, all cells' membrane appears insulating and therefore less polarizable than the blood medium. Consequently, these cell types exhibit a negative CM factor and experience nDEP. As the frequency increases from 100MHz to 1GHz, the electric field bridges the membrane and the CM factor will again compare the conductivities of cell's cytoplasm with the media. In this stage, most of the cells will experience a rise in CM factor, except platelet. Such a condition is caused by the conductivity of platelet cytoplasm is lower than that of membrane, and vice versa for others cells. In contrast to RBC and cancer cells, a steeper rising curve of CM factor is obtained for WBC. As depicted in

Figure 4.1, it increases and crosses into the positive domain, thus changing its sign, from negative to positive values. This condition is likely due to cytoplasmic proteins of WBC that impart a net permittivity higher than the blood medium, and vice versa for others cells.

As had been recognized, the target cell one wishes to separate need to have opposite CM sign from other blood cells at an applied frequency. However, due to the highly conductive feature of a whole blood sample, the target cells in our study will display similar DEP signs with other blood cells (e.g. RBC), for a given range of frequency of 1kHz to 1GHz (see Figure 4.1). Consequently, the separation may not be effective. By employing MAP as pre-enrichment stage, the overlapping of DEP response between CTCs and blood cells can be eliminated, as such the RBCs will first be removed from a given blood sample and only nucleated cells such as WBCs, platelet and CTCs undergo isolation in DEP stage.

Nevertheless, it have been known that the removal of RBC in MAP stage will result in a change of whole blood conductivity which flow into a DEP stage, as proved in an experimental study conducted by Abdalla *et al.* (2010). A relationship between the total flowing blood conductivity and haematocrit (RBC volume) value can be represented using Maxwell-Fricke Equation (Gaw, Cornish, & Thosmas, 2007):

$$\sigma_p = \frac{\sigma_m}{1 + (1 - \frac{H}{100-H})C} \quad \textbf{4-1}$$

where σ_m is suspension conductivity, σ_p is plasma conductivity (1.6 S/m) and C is a constant function which represent the orientation of RBC, as such 3.3 for the random orientation (Visser, 1989). Meanwhile, H is the fractional haematocrit value, in which:

$$H = \frac{Volume\ of\ RBC}{Volume\ of\ Blood} \quad \textbf{4-2}$$

Notably, normal human haematocrit level is 40 % (Issa *et al.*, 2014). Assuming RBCs are removed from MAP, the obtained H level will be decreased from 40 to approximately 0%. When the new H value is substituted into eq. (4-2), the conductivity of the blood suspension is equal to 0.37S/m, which is lower in contrast to normal blood sample. The theoretical value of CM factor for WBC and cancer cells in whole blood sample with 0% of haematocrit can be plotted as depicted in Figure 4.2.

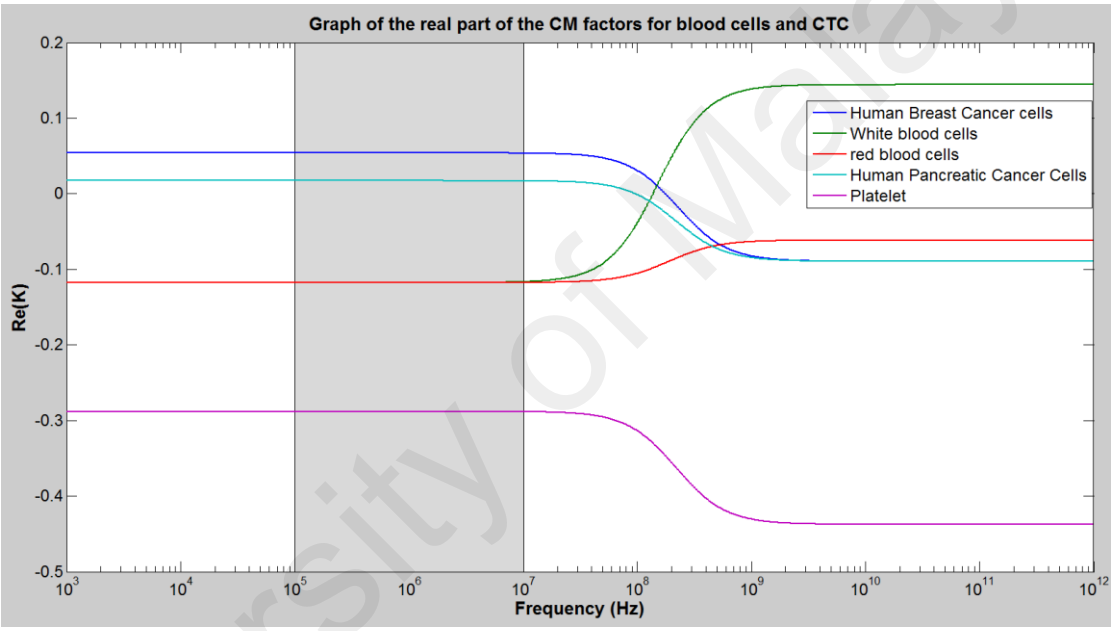

Figure 4.2: Real part of Clausius-Mosotti (CM) factor for human breast cancer cells, human pancreatic cancer cells, WBC and RBC in whole blood sample with a conductivity of 0.37 S/m.

From the graph, a reduction in the blood conductivity has caused changes in the CM factor of blood cell. Unlike normal DEP response (Figure 4.1) which cells act like insulator at frequency between 1kHz to 100MHz, the measured CM factor for CTCs in our proposed device is positive and vice-versa for other cells. The condition is particularly caused by the effect of Maxwell Wagner polarization, whereby the charges are accumulated at the cell membrane opposing the electrode (Qian *et al.*, 2014). Consequently, cell behaves as an electric dipole with these frequency. Due to the

difference in a sign of CM factor between cancer cells and other blood cells, the frequency used in DEP separation can thus be chosen from 1kHz to 100MHz. Noteworthy, the region coloured with grey represents the ideal DEP operating as aforementioned in Section 3.2. To fulfil the design requirement as stated in Section 3.2, a frequency of 1MHz will be used in our DEP stage. The intracellular potential plot for cells when subjected to a non-uniform electric field of 15Vp-p at the designated frequency can be simulated with COMSOL and they are depicted in Figure 4.3. To ease the comparison, the colour bar for these surface plots are designated to have the same mapping of data value, whereby the highest value within the microchamber is indicated on the top of this bar.

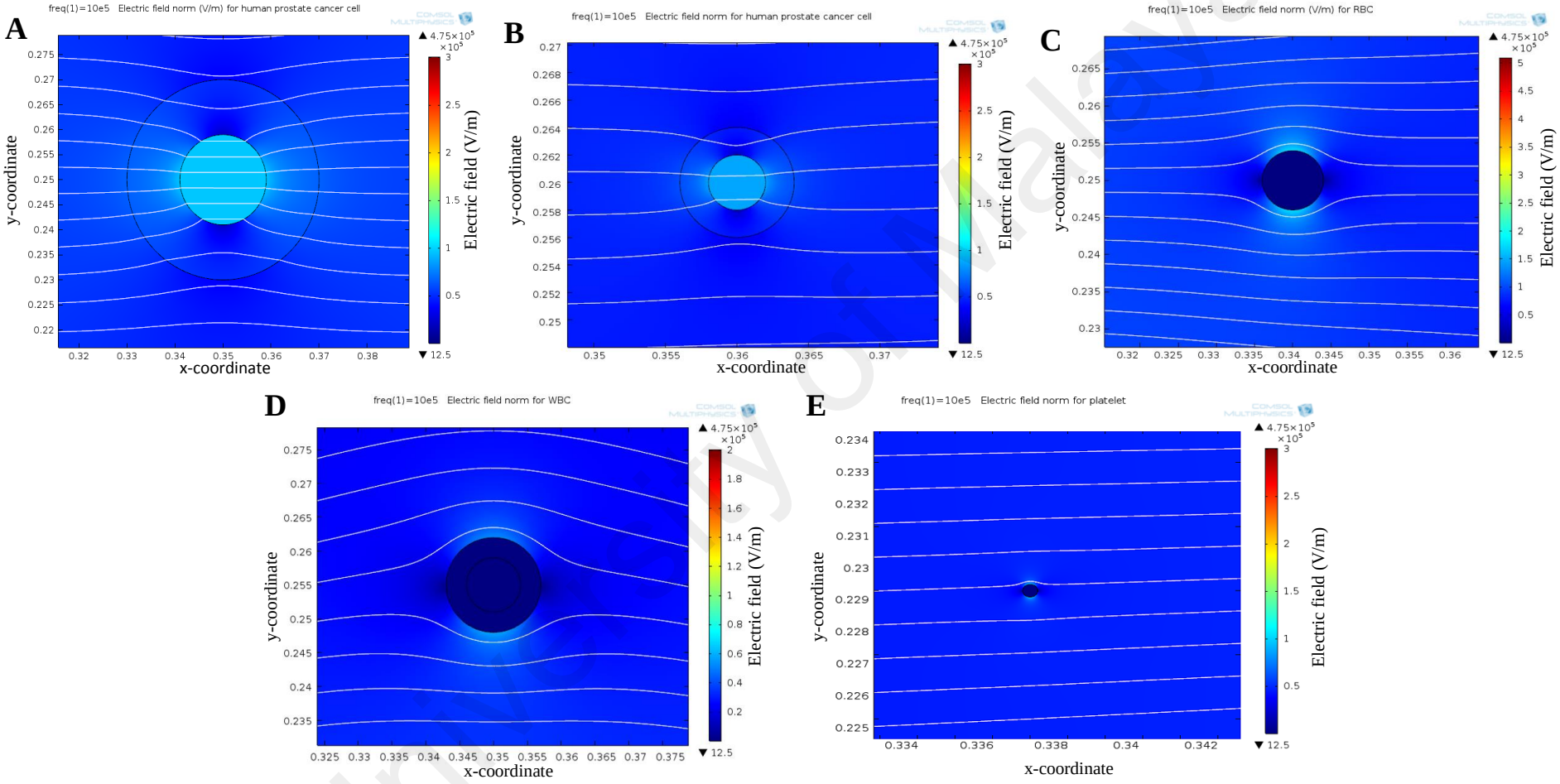

Figure 4.3: Intracellular potential plot for (A) Human Breast Cancer Cell; (B) Human Prostate Cancer Cell; (C) RBC; (D) WBC and (E) Platelet in a non-uniform electric field with the frequency of 1MHz. The streamline represents the intracellular potential distribution meanwhile the surface plot represents the electric field.

From Figure 4.3 (A) and (B), it can be observed that the electric potential within both types of CTC at the applied frequency of 1MHz will be focused across the cell membrane and nucleus. Consequently, these cell will exhibit pDEP. Meanwhile, less electric potential is detected across cells such as RBC (Figure 4.3(C)), WBC (Figure 4.3(D)) and platelets (Figure 4.3(E)). Thus, these cells will experience nDEP.

Based on both CM factor and intracellular potential plot, the use of MAP as pre-enrichment stage of the DEP device can reduce the blood medium's conductivity thus enable a CM factor difference to be present between target cells and blood cells. To enhance the downstream DEP performance, it is crucial for RBC to be successfully isolated from a blood sample in the MAP stage. For this propose, a MAP stage which facilitates the high RBC recovery rate is needed.

4.2 Magnetophoretic (MAP) Stage

It has been known that MAP separates cell based on the presence of magnetic field gradient within a microchannel. To achieve best separation output (e.g. high separation efficiency), it is therefore instructive to examine such a force in details. In this section, we will study the effect of magnetic field caused by various placements of permanent magnets as well as the use of ferromagnetic track. The geometrical design of the MAP chamber which accommodates uniform flow as well as optimized magnetic field distribution would be investigated. For the purpose of this analysis, the design concept will focus solely on the MAP stage. Permanent magnets with dimension of 15mm×10mm×10mm will be employed in our computational study. Noteworthy, the length is determined accordingly to the length of MAP microchamber.

4.2.1 Magnetic orientation of permanent magnets

Three references of permanent magnet configuration as mentioned in section 3.3.1 are studied. For a conventional method, a magnet is located at 5mm from the microfluidic channel and it is simulated having a positive magnetization. Meanwhile, the face-to-face magnet configuration is surrounded by two permanent magnets, with 5mm from the microchannel wall at each side. As mentioned previously, the ratio of magnet length to magnet inter-gap distance for face-to-face magnet configuration need to be more than 1. In this design, the calculated ratio is $\frac{15}{10+0.75} = 1.395$ and thus fulfil the design requirement. To generate an attractive magnet orientation as notified in Figure 3.3 (B), the magnetization of both permanent magnet is configured as positive. Conversely, for a repulsive magnet configuration (see Figure 3-3 (C)), the magnetization of both magnet is computed to have opposite sign. A distribution of magnetic flux density generated from these magnet configurations will be presented in the surface plot, as depicted in Figure 4.4.

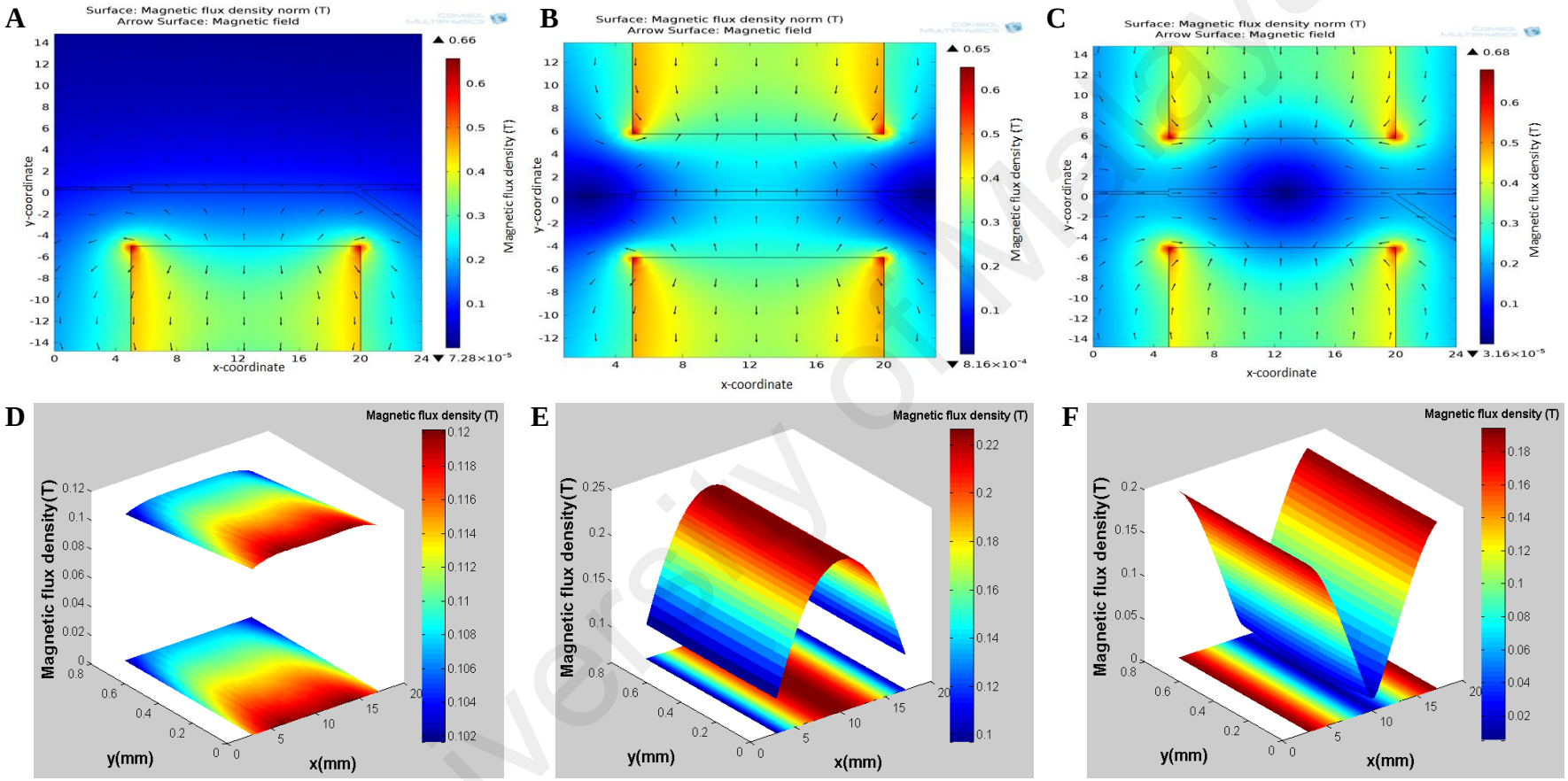

Figure 4.4: Schematic of surface plot of magnetic flux density for (A) single magnet configuration, (B) attractive magnet configuration and (C) repulsive magnet configuration. The distribution of magnetic flux density within the microchannel for each models are plotted in 3D surface plot at the bottom of surface plot, with contour plot projected onto x-y plane, labelled as (D), (E) and (F)

Figure 4.4(A)-(C) shows the 2D surface plot of magnetic flux density (**B**) of the discussed permanent magnet configuration. To illustrate the direction of the magnetic field in each model, an arrow plot of the magnetic field lines will be coupling on each surface plot. In Figure 4.4(A), a uniform magnetic flux density, which is represented by an evenly blue spectrum, is found within the microchannel when a single permanent magnet configuration is applied. Meanwhile, in both attraction (Figure 4.4(B)) and repulsion (Figure 4.4(C)), the fluctuation of magnetic flux density is observed to be higher at the microchannel region which is aligned at the midpoint (x=10) between both permanent magnet. Note that the cell separation will take place in the MAP microchamber. It refers to the region which is located parallel to the permanent magnet that ranges from x=2.5 to x=17.5. To quantitatively evaluated magnetic flux density within this region, 3D surface charts with contour plots projected onto x-y plane, are plotted across the length (x-axis) and the width (y-axis) of the microchannel.

As shown in Figure 4.4(D), the magnetic flux gradient of the single magnetic configuration is found to be orientated toward y-axis, whereby it gradually decreases from 0.12T to 0.104T. This situation can be defined through the inverse square law, which stated that the magnetic flux density is inversely proportional to the distance from permanent magnet squared (Elblbesy, 2010). On the contrary, the magnetic flux density for both attractive (see Figure 4.4(E)) and repulsive configuration (Figure 4.4(F)) is found to be orientated along the length of magnet (x-axis). A symmetry axis is presented at x=10mm for both configuration. For instance, in Figure 4.4(E), the attractive configuration generates a high spectrum value of 0.22 T in the middle region (x=10mm) along the microchannel length and gradually decreasing toward the region next to the edge of the permanent magnet. Meanwhile, the repulsive configuration, as depicted in Figure 4.4(F), displays a mirror 3D surface image of attractive configuration. In this configuration, a lowest magnetic flux density of 0.02T is obtained in the middle

region and the spectrum colour is gradually proceeding to the red at the value of 0.18T toward the region residing the side of permanent magnet. These observed phenomenon within the microchannel for both attractive and repulsive configuration can be explained by referring to the direction in which the arrow points. As shown in the arrow plot, the magnetic lines will travel from north (N) directly to the south (S) pole. Therefore, in an attractive magnet configuration, the magnetic lines from N-pole will go directly to the S-pole confronting it. Consequently, a high magnetic scalar field (represented by the red colour) can be found in the middle zones of the microchannel. It will be gradually decreased toward inlet and outlet, forming a loop around the magnets. Unlike attraction, the repulsive magnet configuration has two positive forces, facing each side of the microchannel wall. Henceforth, this configuration compels the magnetic field lines to turn horizontally before the horizontal symmetry axis of the microchannel. As a result, a low (shorter arrow) field region and two focusing zones with high magnetic field can be found respectively in the middle of a microchannel and the corners of both magnets.

In process of further validating the result, a post-processing of particle trajectories within the microfluidic channel was implemented. For this model setting, a steady state study is employed whereby an initial condition of cell is assigned to align along the length of microfluidic channel, with a constant distance of 5μm from each other. The resulted plot is delivered in Figure 4.5, which its equalities of forces are stipulated according to Eq. (2-13). To ease the analysis process, a grey-scaled magnetic field surface is set as the plot background, as such the high magnetic flux density (**B**) region is represented by light grey and the colour saturation will increase with the decreased of **B**.

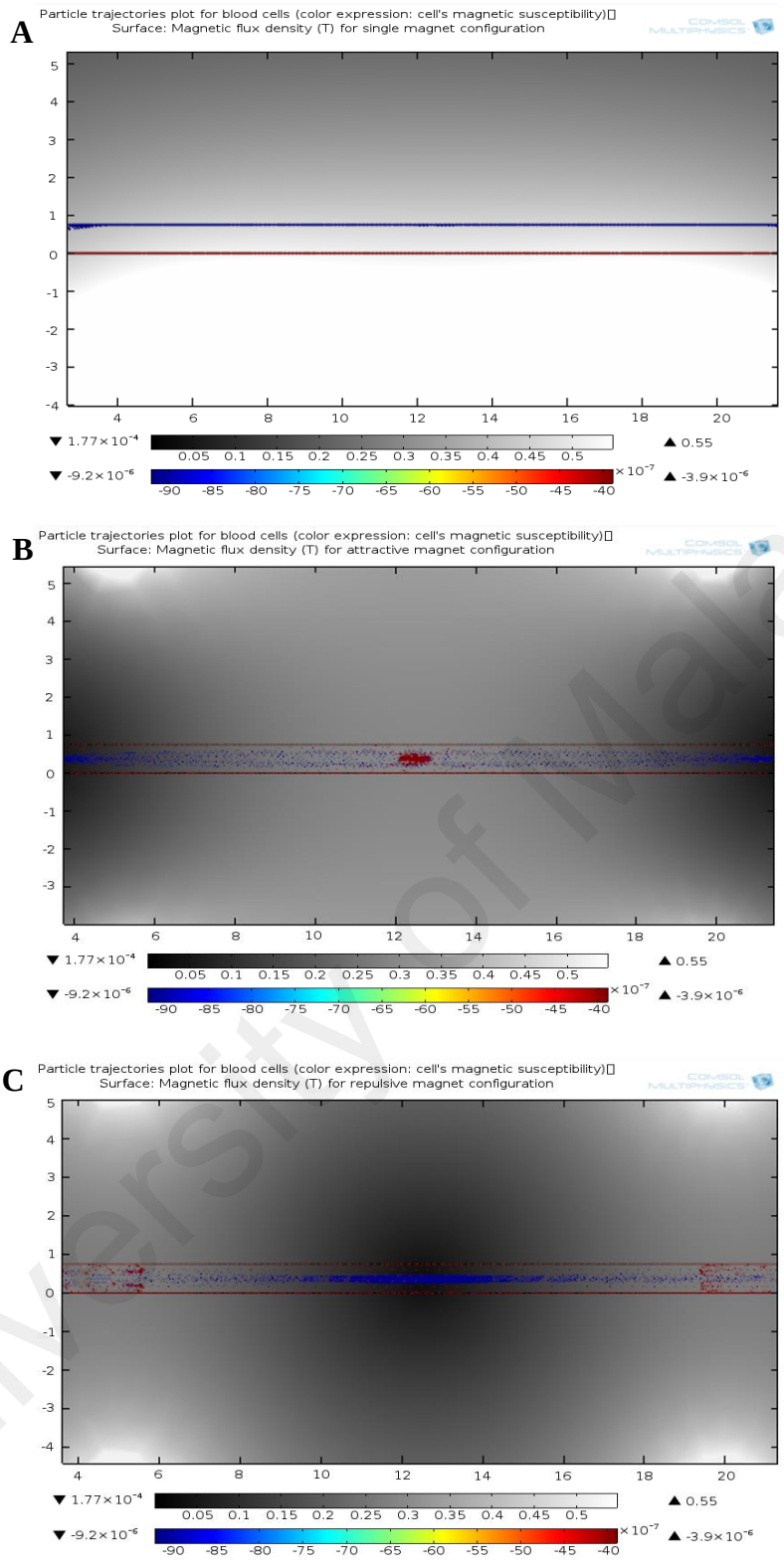

Figure 4.5: Cell trajectories within microchannel: (A) Single magnet; (B) Magnet in attraction; and (C) Magnet in repulsion. The grey scale and colour spectrum bar shows the magnetic flux density and magnetic susceptibility of cells, respectively.

In Figure 4.5, the red particles represent the RBCs meanwhile other nucleated cells such as CTCs and WBCs (which magnetic susceptibility is lower than $-8x10^{-6}$) are represented by blue particles. For single permanent magnet configuration, the cells are found to move toward both side of channel walls. As showed in Figure 4.5(A), RBCs are attracted toward the channel wall located next to the permanent magnet (high **B** region), thus exhibit p-MAP. Meanwhile, n-MAP driven cells such as CTCs, WBCs and platelet are found to be repelled toward the opposite channel wall with low **B** value. On contrary, the presence of an axially-symmetric magnetic flux density within the attractive and repulsive configuration has resulted various cells to be accumulated in the middle region of this MAP microchamber. For instance, in Figure 4.5(B), accumulation of RBC is found around this region due to the presence of high magnetic field. Likewise, Figure 4.5(C) shows n-MAP driven cells to be concentrated around the middle of microchannel due to the present of low **B** zone. Considering the influence of magnet orientation, both attractive and repulsive configuration will cause cell blockage within the microchannel thus compromise the purpose of the MAP stage. Since a single permanent magnet would generate two opposing **B** along left-right microchannel wall respectively, coupled with hydrodynamic force, the cells can be separated and directed toward the desired outlets at the end of the MAP stage. Henceforth, this configuration will be selected to generate magnetic force in our proposed MAP stage.

Notably, the operative of magnetic force in this system is determined primarily by two factors: (1) gradient of magnetic flux density ($\nabla \boldsymbol{B}^2$), and (2) a volumetric magnetic susceptibility difference ($\Delta\chi$) between the cells and the surrounding buffered fluid medium. Due to the magnetic susceptibility of blood cells is on the order of 10^{-6} to 10^{-7}, this parameter will not impact force calculation within the proposed MAP system. Therefore, the MAP force exerted on cells is mainly dependent on $\nabla \boldsymbol{B}^2$. As alluded in Section 3.2, the distribution of $\nabla \boldsymbol{B}^2$ should not be less than $10T/m^2$ for a MAP cell

separation device. To ensure optimum MAP force obtained for cell separation, $\nabla \boldsymbol{B}^2$ within the microchannel of the selected magnet configuration will be investigated. An expression for $\nabla \boldsymbol{B}^2$ can be expanded in explicit form to yield:

$$\nabla \boldsymbol{B}^2 = (\vec{B} \cdot \nabla)\vec{B} = \begin{bmatrix} B_x \dfrac{\partial B_x}{dx} + B_y \dfrac{\partial B_x}{dy} + B_z \dfrac{\partial B_x}{dz} \\ B_x \dfrac{\partial B_y}{dx} + B_y \dfrac{\partial B_y}{dy} + B_z \dfrac{\partial B_y}{dz} \\ B_x \dfrac{\partial B_z}{dx} + B_y \dfrac{\partial B_z}{dy} + B_z \dfrac{\partial B_z}{dz} \end{bmatrix} \quad \textbf{4-3}$$

By assuming the single permanent magnet which is located at the side of microchannel is infinitely long in x-direction, Eq. (4-4) can be simplified as such the spatial derivatives of x component is written as:

$$\frac{\partial \vec{B}}{\partial x} = 0 \leftrightarrow \left\{ \frac{\partial B_x}{dx} = 0, \frac{\partial B_y}{dx} = 0, \frac{\partial B_z}{dx} = 0 \right\} \quad \textbf{4-4}$$

Aforementioned, the flow will be established throughout our proposed continuous cell sorting system in a horizontal direction (x-axis). As B_y is directed across the channel width, it will induce the magnetic velocity that is superimposed with cell separation in the MAP stage. An iso-value of $\nabla \boldsymbol{B}^2$ in y-direction can be provided as:

$$\nabla \boldsymbol{B}^2 = \left[B_y \frac{\partial B_y}{dy} + B_z \frac{\partial B_y}{dz} \right] \quad \textbf{4-5}$$

The spatial derivatives of y-component magnetic flux is plotted in Figure 4.6.

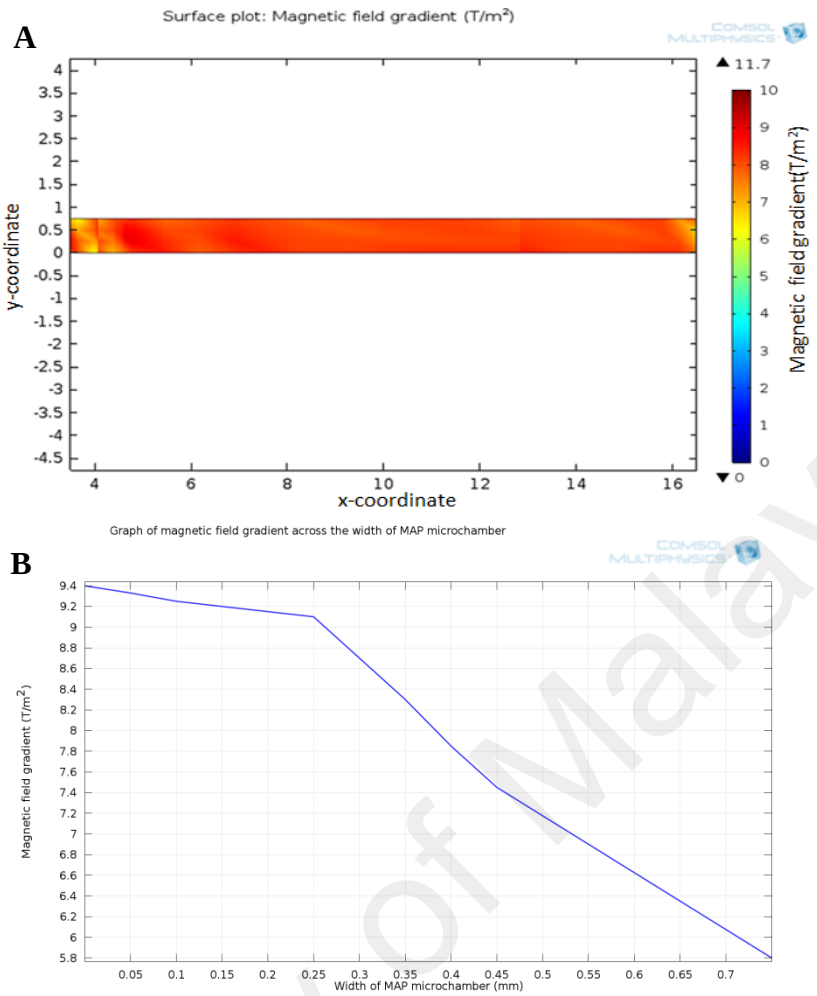

Figure 4.6: (A) Surface ∇B^2 plot. (B) Average ∇B^2 across the width of MAP microchamber.

In Figure 4.6(A), the surface plot has showed the derivative of magnetic field is uniform across the channel. To quantitatively analyse gradient of magnetic field within the microchamber, the graph of average y-derivative of magnetic field across the width is plotted (Figure 4.6(B)). From this graph, the derivative of magnetic field is found to be reduced with the distance from permanent magnet, as such the difference between the highest and lowest value of $\nabla \boldsymbol{B}^2$ is 2.2T/m^2. However, the highest gradient of magnetic field obtained from this simulation is in the approximate to 9.4T/m^2. Such a condition does not fulfil the design requirement as stated in Section 3.2, where the magnetic field gradient exacted on the cells within the microchamber have to be in more

than $10T^2/m$. To optimize the $\nabla \boldsymbol{B}^2$, a soft magnetic element will be integrated in our proposed MAP stage.

4.2.2 Ferromagnetic track configuration

It has been shown that the magnetic field and force is restricted to a specific location defined by the magnet pole orientation. In order to overcome the low magnetic forces on biological cells, a rectangular ferromagnetic track which is made of NiFe (Permalloy) elements, will be tapered inside the microchannel of the proposed MAP stage. This element allows the bias magnetic field to be locally amplified into the microchannel, thus gives rise to a magnetic force on the cell flowing through the microchannel. The length and height of this track is designated as 14.5mm and 0.5mm, respectively. Meanwhile, its width is fixed to 0.25mm due to the limitation technique available in the foundry. As illustrated in Figure 4.4(A), the enlarging field lines at the magnet extremities has resulted a decrease in the magnetic flux magnitude at the region parallel with the permanent magnet edges. To allow a uniform distribution of magnetic field line to permeate through the ferromagnetic track, the permanent magnet needs to cover the length of the track. A new length of 20mm is therefore designated for the magnet in this study. The schematic of microchannel with ferromagnetic track for the MAP stage is illustrated in Figure 4.7. All dimension used is in millimetres.

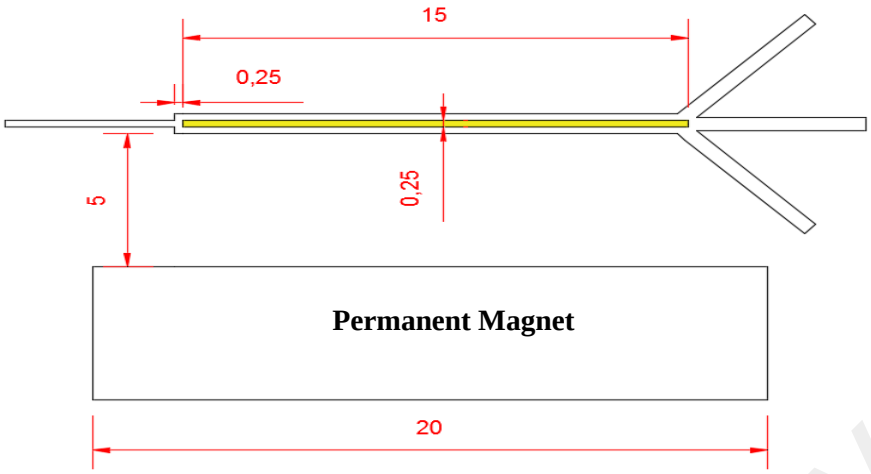

Figure 4.7: Schematic of microchannel with ferromagnetic track (yellow region) in MAP stage.

The distribution of magnetic field for the above geometry is depicted in Figure 4.8. In the presence of magnetic track, the external flux provided by the permanent magnet will magnetize the ferromagnetic track. It has been reported in a previous study that the magnetic domain of a ferromagnetic element will operate linearly with the magnetic flux which permeates through it (Iliescu *et al.*, 2008). Such a condition has caused the magnetic moment to be aligned with one another, thus resulted in the magnetic field lines to be focused through the track. This phenomena is illustrated via the arrow plot in Figure 4.8(A)). Because of these field lines' concentration, a high field pattern (represented by red region) is found within the ferromagnetic track. In spite of it, there is a low field pattern presented in the middle region of the proposed track. The reason for such a condition is caused by the flowing loop of magnetic field lines within the ferromagnetic track. This low field phenomena can be explained by plotting x-component ($\mathbf{B_x}$) and y-component ($\mathbf{B_y}$) of magnetic flux density across the length of the embedded track. The plotted line graphs are showed in Figure 4.8(B) and Figure 4.8(C), respectively.

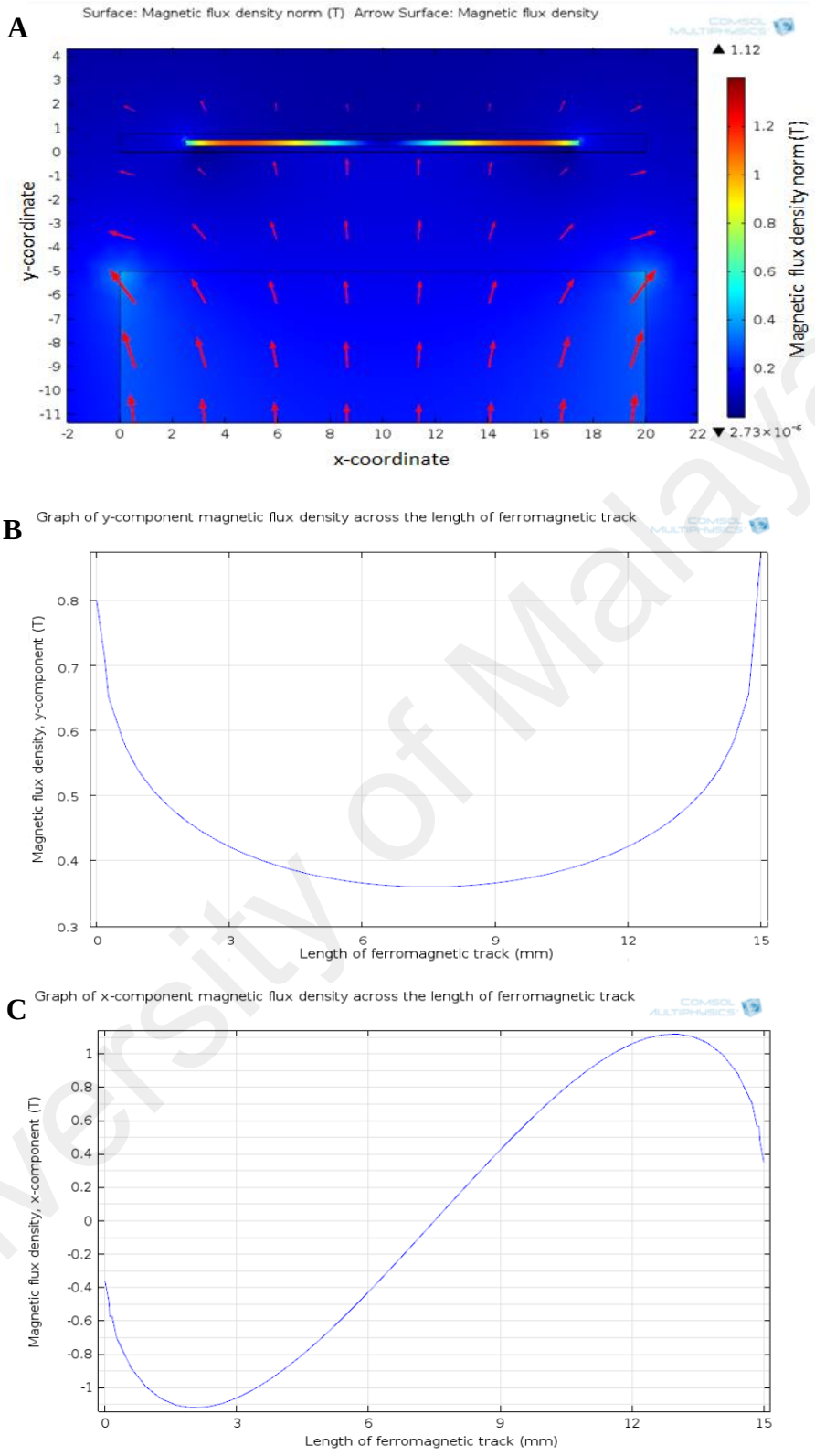

Figure 4.8: Magnetic flux density analysis by (A) Surface plot. Graph of magnetic flux generated within the ferromagnetic track vs the length of the track is plotted for: (B) y-component and (C) x-component.

In Figure 4.8(B), the $\mathbf{B_y}$ is found to be uniform along the length of the ferromagnetic track, with an average of 0.35T. The value is increased to 0.8T towards the edge of the track due to the field concentration effect as a result of the high surface area-to-volume ratio at this coordination. Likewise, Figure 4.8(C) also displays a high $\mathbf{B_x}$ at the edge of the ferromagnetic track. However, centring at the middle point of this track, the magnitude obtained at both edge is opposite to each other. This phenomena can be explained by the magnetic ordering of the atomic moment within the ferromagnetic track, whereby their dipoles will spontaneously align parallel in response to the closed-looped flow direction of magnetic flux from a single permanent magnet (Chen *et al*., 2015). Consequently, the magnetic dipole which is presented at the centre region of magnetic track will be nullified by others dipoles which are aligned antiparallel to it, thus results a zero $\mathbf{B_x}$. Notably, on a cross section of constant z direction, the magnetic flux density, **B** is equal to the square root of the flux density in x and y direction, such that:

$$\boldsymbol{B = \sqrt{B_x^2 + B_y^2}} \qquad \textbf{4-6}$$

By relating this equation to both Figure 4.8(B) and Figure 4.8(C), the surface plot obtained in Figure 4.8(A) can thus be justified.

In order to ensure the acquired MAP force will be sufficient to deviate the cells toward the high and low magnetic flux density region within a continuous flow, the $\mathbf{B_y}$ which is generated across the channel width will be examined. As illustrated in Figure 4.8(B), the distribution of $\mathbf{B_y}$ along the length of the ferromagnetic track is symmetrical to the y-axis. To ease the analysis process, the comparison will only be implemented on $\mathbf{B_y}$ at three surface cross sections, which are labelled with I, II and III (see Figure 4.9(A)). In this case, I refers to the cutline across the microfluidic channel at the edge of

a ferromagnetic track. Meanwhile, II and II represents the cutline at quarter points and midpoints of the track, respectively. A graph of $\mathbf{B_y}$ across channel width at these surface cross-sections is delivered in Figure 4.9(B).

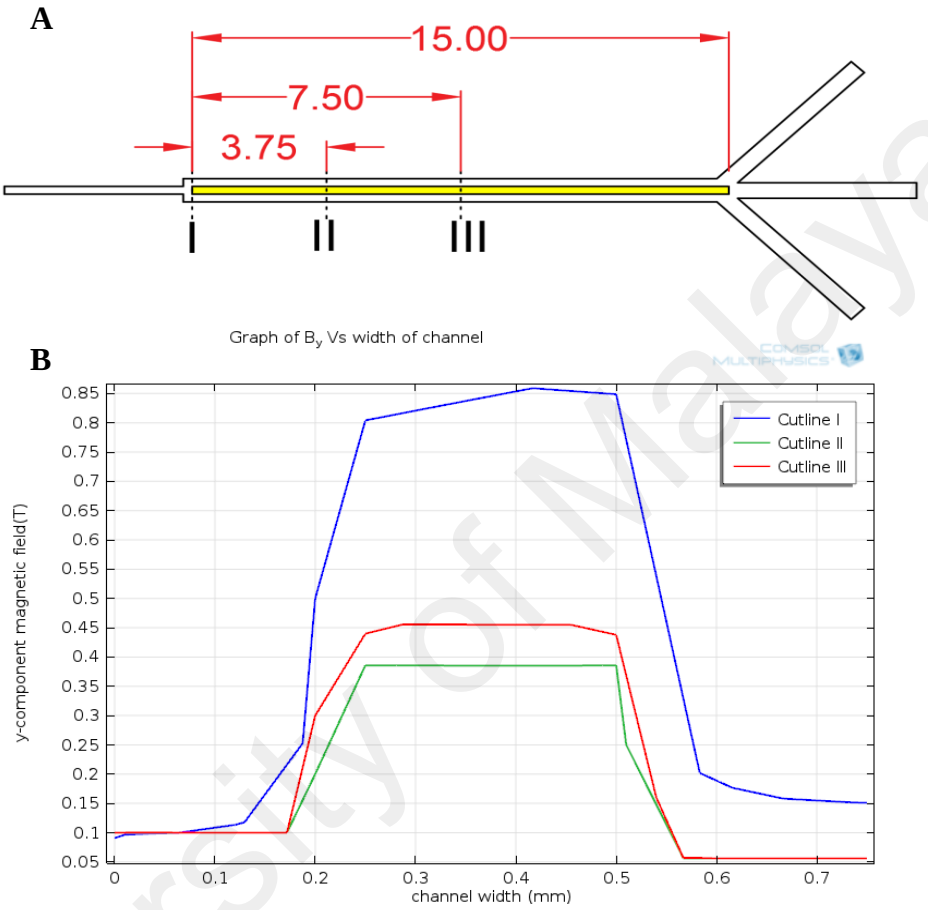

Figure 4.9: Y-component magnetic field analysis at (A) cross section within microfluidic channel labelled with I, II and III. (B) The distribution of B_y is plotted across the channel width.

From the Figure 4.9(B), the three cutlines display a similar trend in the plotted line graph such that a maxima of magnetic field is obtained at the region within the ferromagnetic track and a minima magnetic field is found at the fluid-flowing channels. When an external magnetic field ($\mathbf{B_{ext}}$) is applied toward the microchannel, the difference of net magnetization (**M**) between permanent magnet and the magnetic track will cause the sample in the region bounded by x=0 to x=0.25 to be rotated by the

torque in an equilibrium direction which is along y axis in our study. Consequently, a uniform distributed magnetic field is obtained in this region. Due to the present of strong localized field within the ferromagnetic track, the magnitude of $\mathbf{B_y}$ is then found to increase and reach its maxima value in the region of x=0.25 to x=0.5. Interestingly, a plateau region of magnetic field is presented within the magnetic track. Such a condition can be described through the concept of magnetic anisotropy by Albrecht *et al*. (1992). Their study has stated that the magnetization within a ferromagnetic material ($\mathbf{M_T}$) is uniform whereby its magnetic moments rotates in unison. The equation for $\mathbf{M_T}$ is written as:

$$M_T = \frac{\mu}{V} \qquad \textbf{4-7}$$

where μ and V is the magnetic moment and volume of the ferromagnetic track. As the magnetic field lines exit through the magnet track, the magnitude of **B** will be reduced due to the enlarging of field lines at extremities.

As previously mentioned, the cell separation in a MAP stage is related to magnetic field gradient. To gain an insight on cell deviation path, the y-component of magnetic field gradient ($\left|\nabla \cdot B_y^2\right|$) within the chamber needs to be evaluated. Its mathematical simulation is generated based on Eq (4-5) with data obtained from the surface chart in Figure 4.8(A). The calculated y-component of magnetic field gradient is presented in Figure 4.10(A), whereby the gradient of magnetic field is found to be higher at the region around the wall of the ferromagnetic track. In the process of further validating the result, a graph of $\left|\nabla \cdot B_y^2\right|$ is plotted across the microchannel as illustrated in Figure 4.10(B). The representative of the three cutlines are in accordance to those described in Figure 4.9(A).

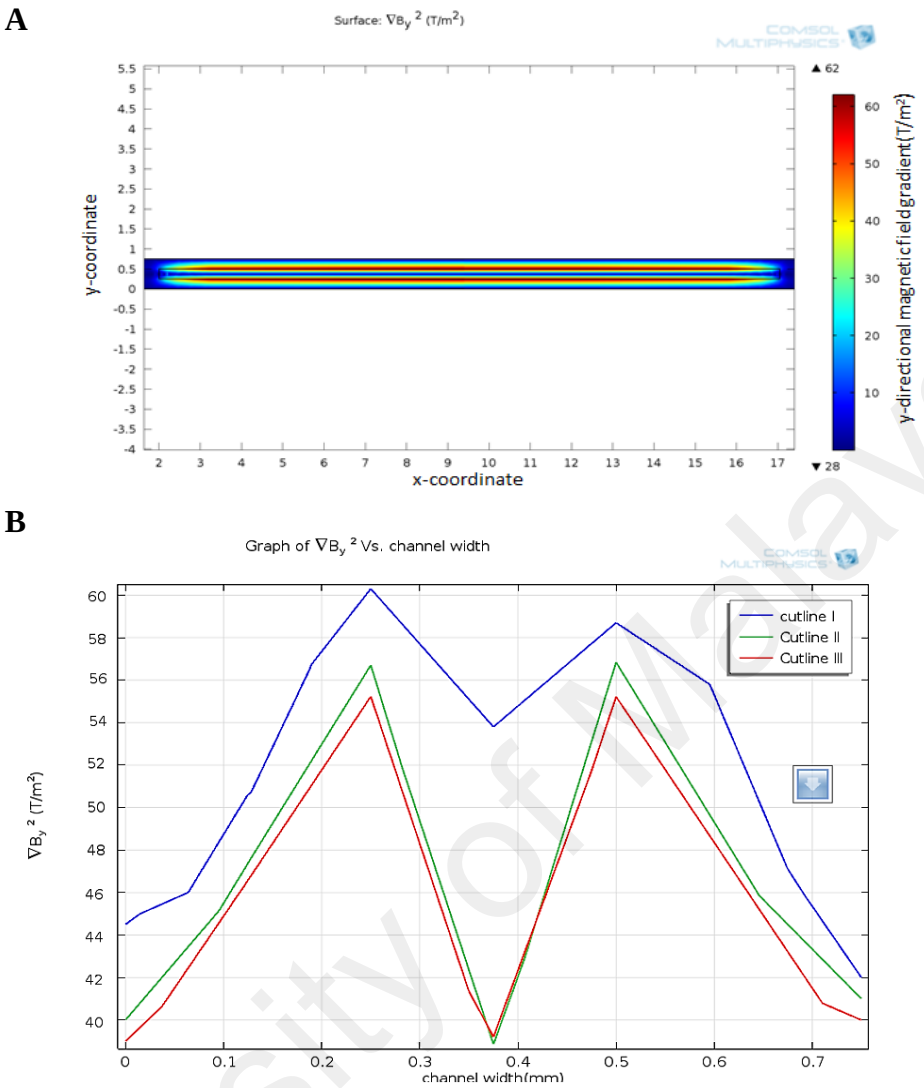

Figure 4.10: Magnetic field gradient analysis of (A) Surface plot and (B) Graph of $\nabla B_y^{\ 2}$ across channel width.

From Figure 4.10(B), ∇B_y^2 is found to gradually reduce towards the channel walls, with coordinates at x=0 and x=0.75. Since the direction of the cell movement is related to the magnetic field gradient, the cells with high magnetic susceptibility such as RBCs will be attracted toward the magnetic track and vice versa for other blood cells with low magnetic susceptibility. In contrast to single permanent magnet configuration as discussed in Figure 4.6, the use of magnetic track in the middle of the chamber has generated a higher value of magnetic field's gradient such that in the range between 40

to 60 T/m^2. Therefore, this configuration fulfilled the magnetic force requirement to separate cells in the proposed MAP system.

4.2.3 Fluid flow parameter

In a continuous cell separating microfluidic system, the positioning of ferromagnetic track in the middle of microchannel can improve separation efficiency from two perspectives. Firstly, as the individual ferromagnetic piece, it will generate extra short-ranged magnetic force within a microchannel to retain target cells (RBC) on its surface. Secondly, by acting as the splitting structure, it directs sample toward the bifurcation channel at both side of magnetic track, thus increases the volumetric flow of a blood sample to be exposed to MAP force per second.

In conjunction with the presence of the ferromagnetic track, a devised schematic of proposed microfluidic channel geometrical design for MAP stage is illustrated in Figure 4.11. All dimension used are in millimetres. The length of microfluidic channel for MAP stage are fixed to 26mm in order to allow some spaces to serve as DEP stage on the 78mm long microfluidic chip. Meanwhile, the width of both bifurcated channels as well as the ferromagnetic track within the MAP microchamber is designated according to the dimension which had been discussed in previous section, such that 0.25mm. To regulate the flow rate distributions to these channels, the inlet channel is proposed to have the same dimension to the bifurcated channel, as suggested by Takagi *et al.* (2005). Noteworthy, when the cell suspension is directed toward the MAP chamber, the cells will be separated into two main stream under the influence of magnetic force. For instance, the RBCs are attracted toward a region next to the ferromagnetic track surface, while other nucleated cell (e.g. WBC, platelet cells and tumour cells) will be repelled toward the channel wall. To collect these cells, three outlet channels are designated at the end of MAP chamber. The central outlet channel which directs RBC toward the

collection port is fixed to 0.5mm. This value is provided based on the effective range of high magnetic field, which is 0.1mm from the wall of magnet track, as shown in Figure 4.9(A). Both lateral outlet channel which carry other nucleated cells (e.g. WBC, platelet cells and tumour cells) toward the DEP stage are at the angle of 55° from central outlet channel. According to Murray's law, the cross section and shape of drain channel at n-th level must be the same to equalize the hydraulic resistance of each part (Emerson *et al.*, 2006). Therefore, these channel would have the same dimension as the outlet channels.

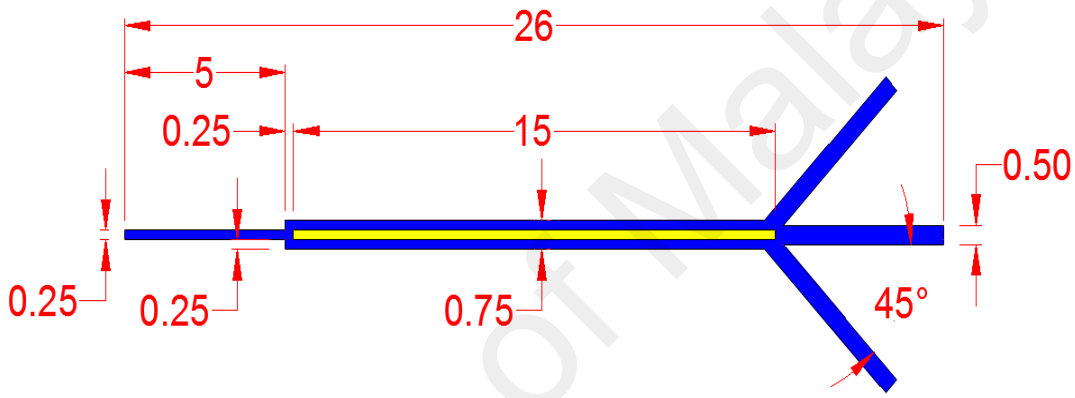

Figure 4.11: Schematic of the proposed microfluidic channel architecture for MAP.

Note that both magnetic and hydrodynamic force will dominate the motion of cells within the channels toward their designated outlets. To adapt the ferromagnet track toward effective continuous cell separation, the flow velocity and dynamic pressure generated within the proposed microfluidic channel (as presented in Figure 4.11) needs to be examined. It has been achieved with Navier-Stokes simulation. For a preliminary evaluation of flow profile within a channel, the inlet flow velocity boundary condition will be determined based on the desired velocity field within a MAP microchamber. As alluded in Section 3.2, a velocity flow generated within MAP chamber should fulfil the range as stated in Eq. (3-14) to ensure that all cells reach their equilibrium positions under $\mathbf{F_{HDY}}$ and $\mathbf{F_{MAP}}$. In pursuance of higher throughput, the optimized velocity field

will be adapted not more than the maximum flow parameter. The Eq. (3-14) can thereby be rewritten as:

$$v_{M\_opt} < \frac{l\,\mu_f\,(\chi_p - \chi_m)\,V_c \frac{\partial H_{ext}}{\partial y}^2}{4\pi\eta\,wR} \qquad \textbf{4-8}$$

In this equation, the *l* and *w*, which refers to the length and width of MAP microchamber, is 15mm and 0.25mm, respectively. Meanwhile, $\frac{\partial H_{ext}}{\partial y}$ can be evaluated through the surface plot in Figure 4.10(A), whereby an average value of 49T/m^2 will be employed for this calculation. It has been known that RBC is the targeted cell in MAP stage. To achieve an optimum flow velocity without compromise its recovery rate, Eq. (4-19) will be determined based on RBC properties (see Table 2-1). By substituting the values into Eq. (4-19), an approximate velocity flow within a MAP chamber can be calculated and represented as below:

$$v_{M\_opt} < \frac{l\,\mu_f\,(\chi_p - \chi_m)\,V_c \frac{\partial H_{ext}}{\partial y}^2}{4\pi\eta\,wR}$$

$$< \frac{l\,(1+\chi_m)(\chi_p - \chi_m)\,V_c \frac{\partial H_{ext}}{\partial y}^2}{4\pi\eta\,wR}$$

$$< \frac{(15\times10^{-3}m)(1-7.7\times10^{-6})(-3.96\times10^{-6}+7.7\times10^{-6})\,(8.86\times10^{-7}m^3)(49\frac{N}{m^3})}{4\pi(2\times10^{-3}\frac{kg}{m\cdot s})\,(0.25\times10^{-3}m)(4\times10^{-6}m)}$$

$$< \frac{2.44\times10^{-11}}{5.03\times10^{-11}}$$

$$< \underline{97\text{mm/s}}$$

Notably, a study conducted by Emerson *et al.* (2006) has shown a volumetric flow rate is halved at each bifurcation, as such the mean velocities of n-folded network can be written as:

$$\frac{V_n}{V_{in}} = 2^{-n}\frac{A_0}{A_n} \quad \textbf{4-9}$$

where A_0 and A_n represents the cross section of an inlet and its drain channels, respectively. To obtain a flow velocity of 90mm/s for our proposed design, the inlet velocity boundary condition (V_{in}) is fixed at:

$$\frac{90\frac{mm}{s}}{v_{in}} = 2^{-1}\frac{0.25mmx0.5mm}{0.25mmx0.5mm}$$

$V_{in} = \underline{0.18m/s}$

The simulation of velocity profile within the channel will be conducted and its result is presented in Figure 4.12.

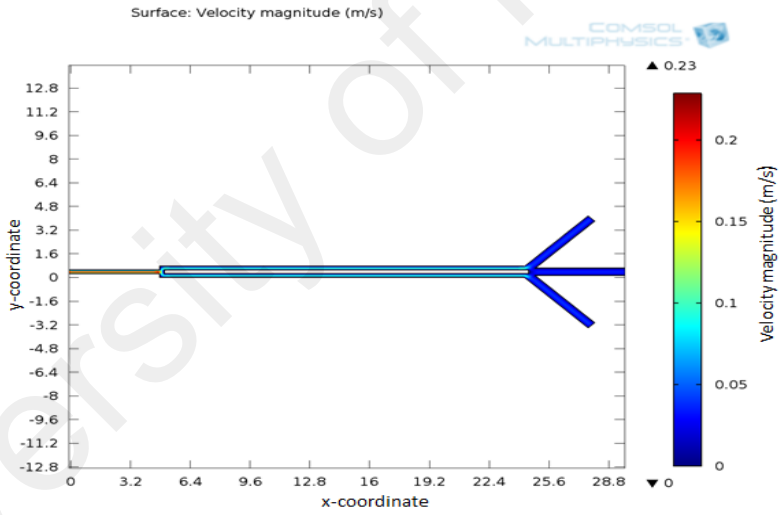

Figure 4.12: Surface velocity plot of the proposed microfluidic channel for MAP stage.

When blood sample is pushed into the inlet, an acceleration meniscus will be formed at the flow centre (Lee *et al.*, 2012). Such a condition has resulted in the flow velocity within an inlet channel to be slightly higher than the specified inlet velocity. It can be proved by a red colour segment in this region which approximates to 0.2 m/s. As the flow transports through the symmetrically-split downstream channel, a downward colour sweep which indicates a decrease in the velocity field is observed in the surface

plot. Such a condition is caused by the increased of hydraulic resistance within the proposed design. It can be explained by considering the flow of fluid within the channel behave akin to the flow of electron in electric circuit (Saliterman, 2006). The equivalent electric analogy with our proposed microfluidic network is showed in Figure 4.13.

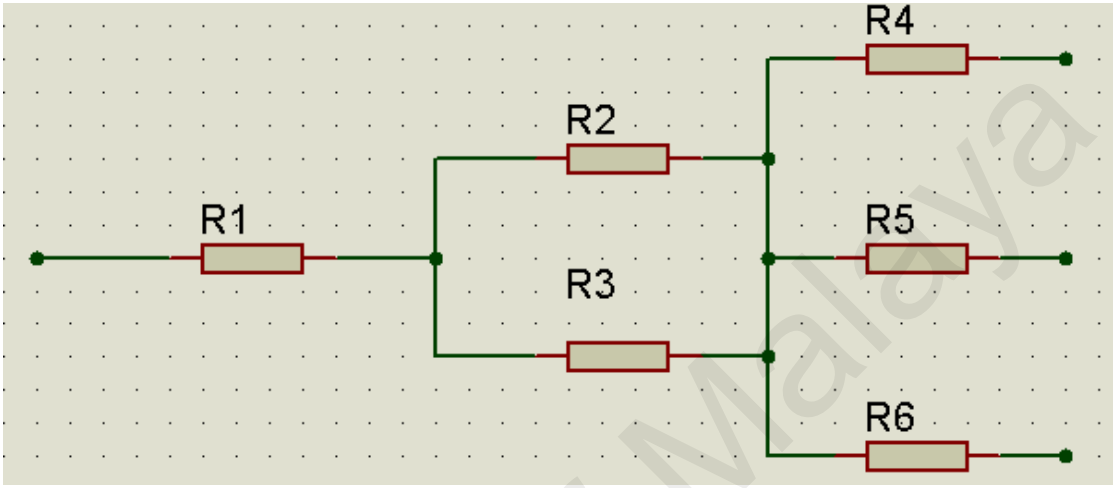

Figure 4.13: Electric analogy configuration of the proposed microfluidic channel for MAP stage.

By referring to Figure 4.13, the hydraulic resistance experienced by cells at the inlet channel (R_{In}), bifurcated channel (R_{birf}) and outlet channel (R_{Out}) can be calculated by summing the reciprocals of R_H within the sub-channel, such that:

$$R_{in} = R_1 \quad \textbf{4-10}$$

$$R_{birf} = R_1 + \frac{R_2 R_3}{R_2 + R_3} \quad \textbf{4-11}$$

$$R_{out} = R_1 + \frac{R_2 R_3}{R_2 + R_3} + \frac{R_4 R_5 R_6}{R_5 R_6 + R_4 R_5 + R_4 R_6} \quad \textbf{4-12}$$

As cross section of bifurcated-channel at n-th level is same, henceforth, the resistance generated within them will be same too (e.g: $R_a = R_2 = R_3$; $R_b = R_4 = R_5 = R_6$). The equation of (4-11) and (4-12) can be then simplified to:

$$R_{birf} = R_1 + \frac{R_a^2}{2R_a} \quad \textbf{4-13}$$

$$R_{out} = R_1 + \frac{R_a^2}{2R_a} + \frac{R_b^3}{3R_b} \quad \textbf{4-14}$$

From these equation, it showed that the presence of sub-channels has resulted in an increased in hydraulic resistance as it flows from inlet toward outlet. The cells can thus be distributed across the sub-channel with a constant velocity. For instance, an evenly colour which represents 0.09m/s is obtained within the bifurcated channel in Figure 4.13.

Interestingly, Berthier *et al.* (2008) pointed out that the hydraulic resistance within the microfluidic channel also corresponds to dynamic fluid pressure. To ensure the continuality of fluid flow, the dynamic fluid pressure generated within the microchannel will be evaluated. Its surface plot is showed in Figure 4.14.

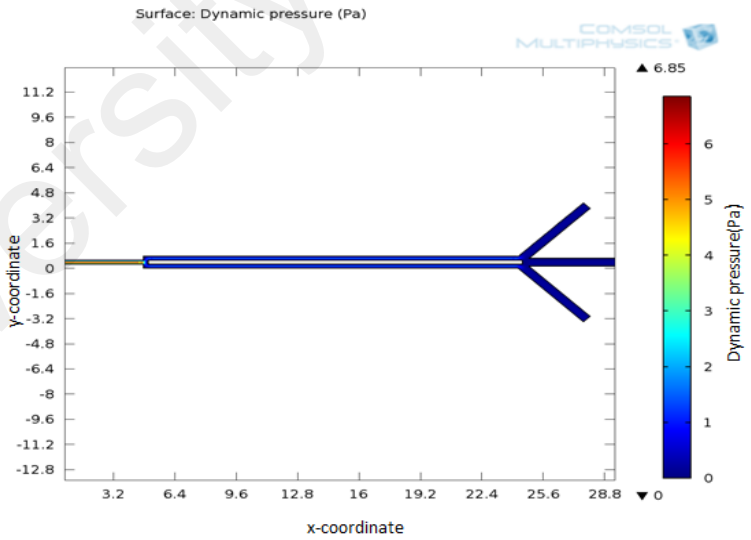

Figure 4.14: Surface plot of fluid dynamic pressure.

From this plot, the flow-driven pressure in microchannel is found to be decreased as the sample flows from inlet toward outlet. This phenomena can be explained by

rewriting Navier Stokes Equation analogously to Classical Ohm law (*V= RI*) (Mortensen, Okkels, & Bruus, 2005). In this context, a fluid pressure corresponds to an electrical voltage (*p~V*); the volumetric flow rate corresponds to the electrical current (*Q~I*) and flow resistance R_H corresponds to an electrical resistor, R. Thus the dynamic pressure drop generated within the microfluidic channel is equaled to:

$$\Delta P = R_H Q \qquad \textbf{4-15}$$

In this equation, ΔP is directly proportional with R_H as Q is held constant. Therefore, the increase of R_H due to the presence of multiple sub-channels will develop a great ΔP. Notably, ΔP in Figure 4.14 can be obtained by subtracting the outlet pressure (P_{out}) from the inlet pressure (P_{in}). As the dynamic pressure obtained at the outlet (P_{out}) of our proposed microfluidic design is approximate to ~0 Pa, ΔP would have similar value with P_{in}. However, such a condition will result in cells not to have sufficient kinetic momentum to be moved toward the DEP stage. To circumvent this problem, P_{out} is needed to be increased. It can be done by reducing the total hydraulic resistance impact on the microfluidic system.

According to Hagen-Poiseuille Law, the theoretical fluidic resistance R_H within each channel can be determined by using geometric parameters, through the summation of a Fourier series, as in Eq. (4-17) below:

$$R_H = \frac{12\mu \cdot L}{wh^3\left(1 - 0.63\frac{h}{w}\left(\sum_n^{\infty} \frac{1}{n^5}\, tanh\left(1.57\, \frac{w}{h}\right)\right)\right)} \qquad \textbf{4-16}$$

where *h* represents a channel cross sections height, *L* is the channel length while *w* refers to the width. Since the aspect ratio (height/width) of inlet and outlet is approximate to 2 and 1 respectively, the hydraulic resistance of the channel within our design can be generalized as:

$$R_H = \begin{cases} \frac{600\mu L}{29wh^3}, & \frac{h}{w} = 2 \text{ (e.g.: } R_1, R_2, R_3) \\ \frac{12\mu L}{wh^3}, & \frac{h}{w} = 1 \text{ (e.g.: } R_4, R_5, R_6) \end{cases} \quad \textbf{4-18}$$

This equation has shown R_H is inversely proportional to w and h, and vice versa for L. Since both length and height are remain constant for each sub-channel, the calculation of R_H will depends on the channel width. Aforementioned, the width for both outlet channels and sub-channel along a magnet track are fixed to 500µm and 250µm respectively in order to enhance the magnetic force exacted on cells. Therefore, R_H within the proposed design can only be reduced by increasing the inlet channel width. An updated microfluidic design is depicted in Figure 4.15.

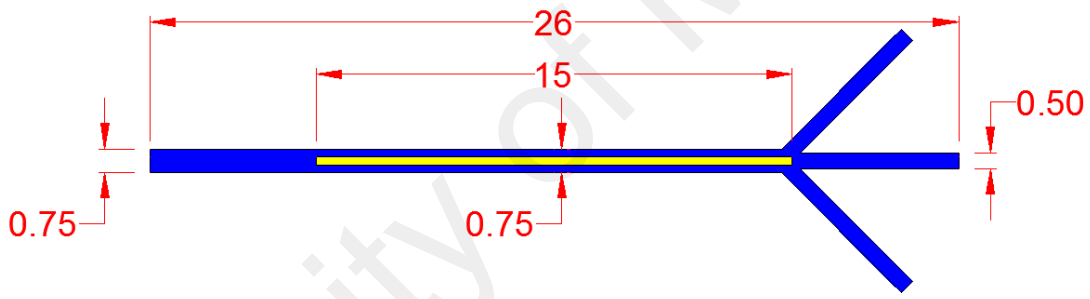

Figure 4.15: Schematic of the updated design for the proposed MAP stage.

As showed in Figure 4.15, the width of the inlet channel is increased from 0.25mm to 0.75mm. Due to this change, there is a need to adjust the inlet velocity (V_{in}) in order to meet the flow velocity requirement within the MAP chamber. According to Bernoulli's Law, in going from a larger channel to a smaller channel will result in an increase in flow velocity. A V_{in} is therefore needed to be decreased by the same factor the area is decreased to acquire the flow velocity of previous design. Using the classical rule explained here before (see eq. (4-9)), the V_{in} value can be obtained, such that:

$$\frac{90\frac{mm}{s}}{v_{in}} = 2^{-1}\frac{0.75mmx0.5mm}{0.25mmx0.5mm}$$

$$\underline{V_{in} = 60mm/s}$$

To test the effectiveness of width alteration on both velocity and dynamic pressure profile, the above channel geometrical design is then examined with COMSOL software, whereby its inlet boundary condition is set according to the calculated V_{in}. Both surface plot of velocity field and fluid dynamic pressure are presented in Figure 4.16.

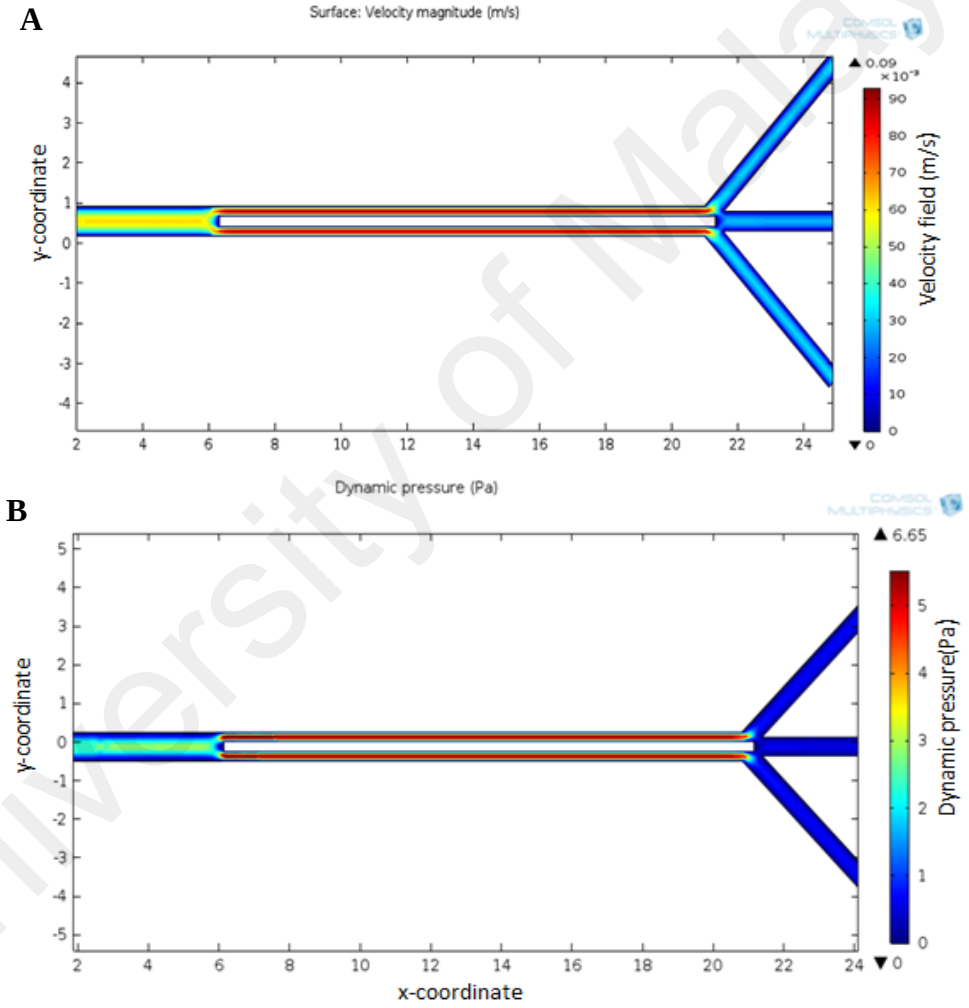

Figure 4.16: Surface plot of (A) velocity field and (B) fluid dynamic pressure.

From Figure 4.16, it is deduced that an increasing width coupled with the decrease of inlet boundary velocity has resulted inlet dynamic pressure to be lower (2.5Pa) than the

previous design (5.5Pa). When the fluid flow from a wide channel to a narrow channel, the dynamic pressure will be increased in corresponding to the increase of flow velocity. As the blood sample flowing toward the outlet, a transition from the profile of the velocity at the entrance to multiple outlets will result in a drop in $P_{out.}$ A P_{out} of 0.5Pa is obtained in the improvised design as depicted in Figure 4.16(B). Because of an improvement in the obtained dynamic pressure value, 0.75mm will be adopted as our inlet width value.

4.2.4 Design Optimization

Generally, the proposed microfluidic structure in Figure 4.15 appears to be the best performance to process flow in a MAP stage. Although the reported rectangular cross-sectional microfluidic channel design is easy to be fabricated, two drawbacks are discovered. Firstly, as alluded in Section 4.2.2, an extremely high magnetic field region is found at the sharp edge of ferromagnetic track. Secondly, when a continuous flow is subjected to the channel, multiple-zero-velocity areas are detected in the sharp corners. Both of these issues can be further evidenced through simulation results as presented in Figure 4.17. A bright cyan colour segment at the edge of the inbuilt ferromagnetic track in Figure 4.17 (A) represents high magnetic field. Meanwhile the dark blue colour segment around the sharp corner in Figure 4.17(B) represents a zero velocity profile. This situation will cause a large number of cells to be accumulated around a sharp corner region. Owing to this, the sharp turns or edges are therefore not optimal for cell separation application.

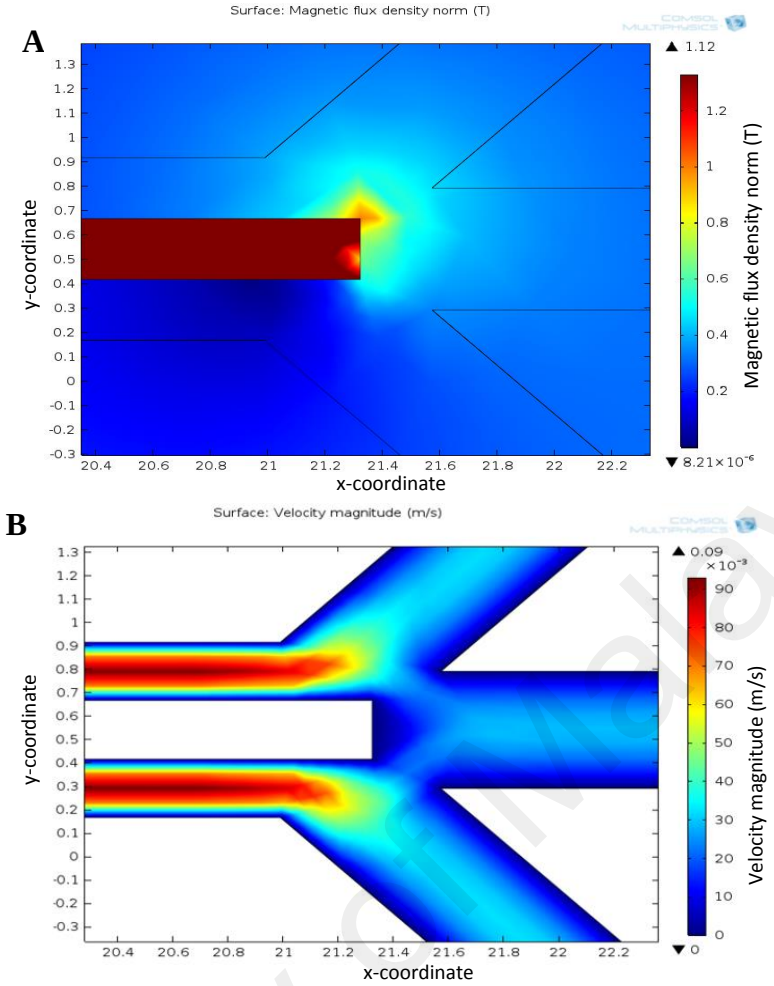

Figure 4.17: Surface plots: (a) Magnetic field and (b) velocity field at sharp corner of the microfluidic channel.

By resorting to the study done by Feng *et al.* (2004) and James *et al.* (2009), a round-shaped turn is identified to generate uniform velocity profiles and cell adhesion within the channel. Thus, the sequence of round-shape turn is used to replace the sharp corner of our original proposed microfluidic channel architecture. The optimized geometrical design is presented in Figure 4.18.

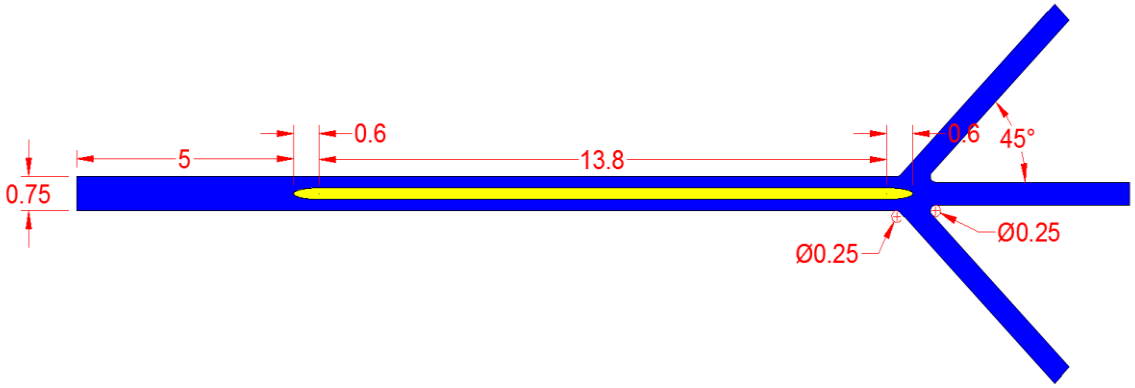

Figure 4.18: Schematic of microfluidic channel layout with rounded corner.

The channel geometrical design is then re-examined with COMSOL software. In contrast to previous design in this study, the surface plots indicate a reduction of high magnetic field (Figure 4.19(A)) and zero velocity field (Figure 4.19(B)) region at the rounded surface of ferromagnetic track. It can be further described through the comparison graph plotted with MATLAB as illustrated in Figure 4.20.

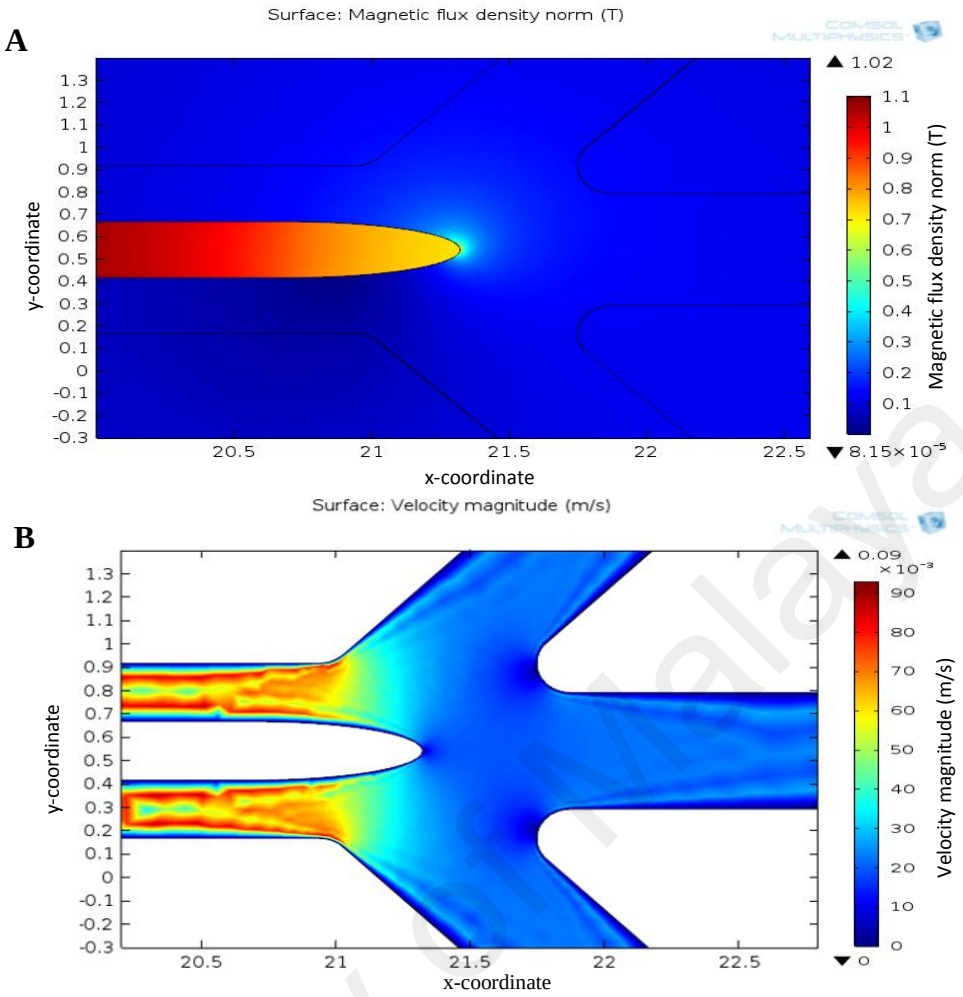

Figure 4.19: Surface plot of (A) magnetic field and (B) velocity field of an optimized MAP stage

A

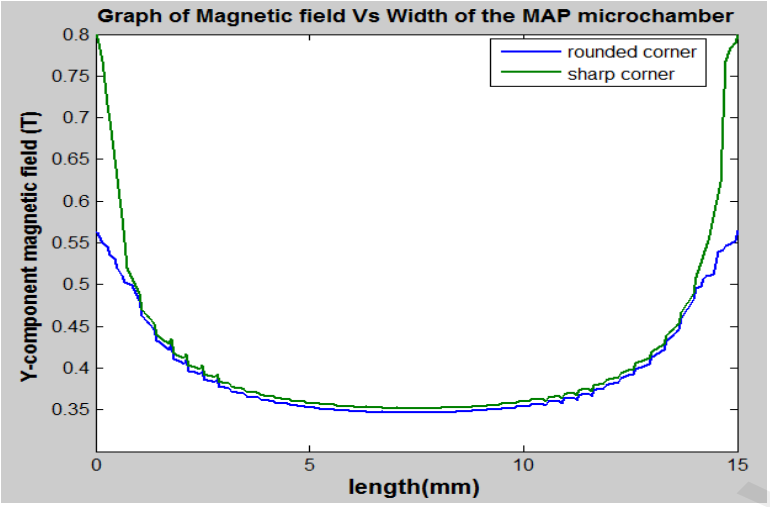

B

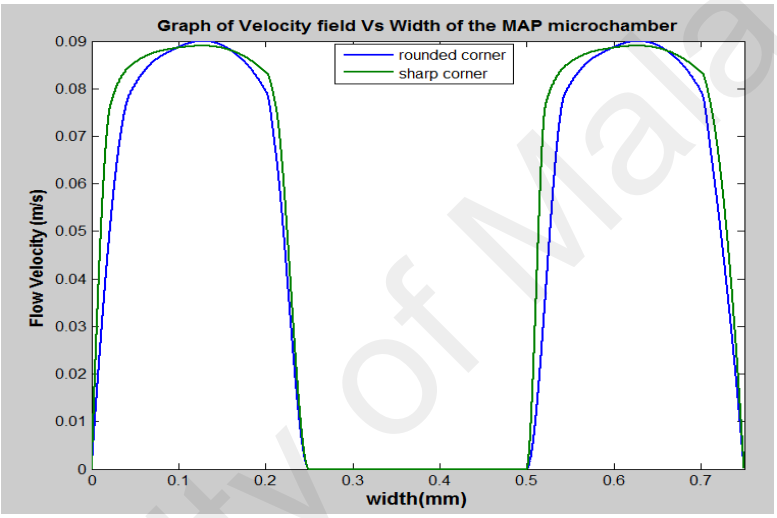

Figure 4.20: Graph of comparison for rounded and sharp corner: (A) Y-component magnetic field across the middle of ferromagnetic track; (B) Average velocity across the width of MAP microchamber.

In Figure 4.20 (A), a magnetic field generated at the edge of ferromagnetic track is observed to be reduced in the rounded ferromagnetic edge in contrast to sharp corner. This reduction can be explained by the fact that the rounding suppresses the pinning fields in the vicinity of a sharp corners and edges (Peeters & Jo, 2002). Meanwhile, when a velocity field is measured across the width of the MAP microchamber, both model showed a reduction in velocity field at the region next to the bifurcated channel wall. Such a condition is caused by the generation of shear stress which acting on the wall surface in the direction of fluid flow. However, comparing to our original design

with the presence of sharp corner, a uniform velocity profile is presented within the improved micro-chamber's bifurcated channel (at distance between 0 to 0.25mm and 0.5 to 0.75mm). Such a profile is thereby encouraging homogenous cell adhesion within it.

Because of the improvement in magnetic and velocity field shown by this design, the improvised geometry will be adopted as the design to be used in the MAP platform.

4.2.5 Cell trajectory

For the proposed MAP device architecture, the cell motion within it can be initially determined by plotting a graph of forces acting on various blood cells. Aforementioned, the deviation of cell within the MAP platform is mainly dependent on y-directional MAP force (forces across the width of MAP microchamber). To examine the force balance between the MAP and hydrodynamic force in this direction, a graph as depicted in Figure 4.21 is plotted.

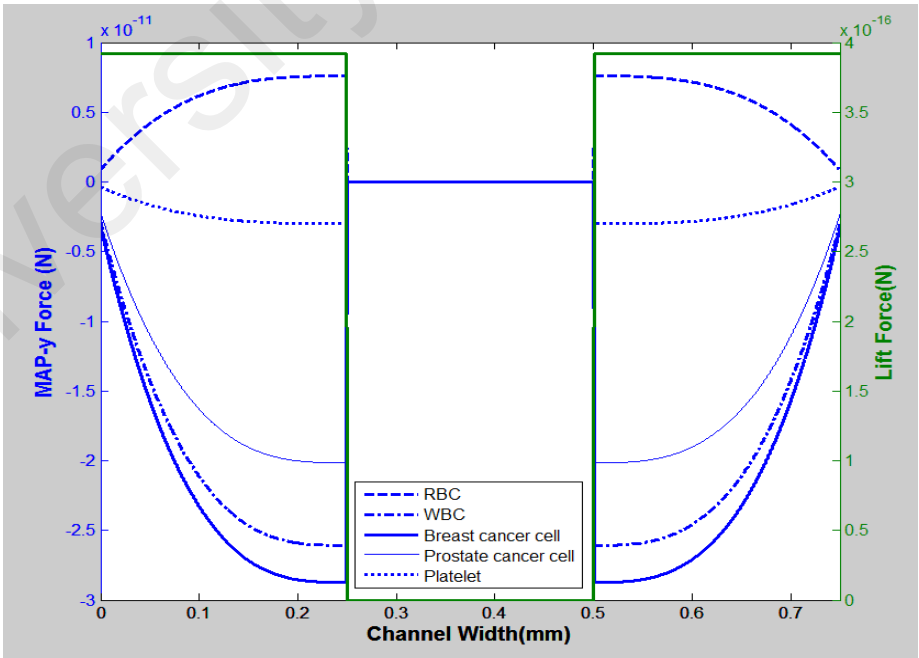

Figure 4.21: Graph of calculated y-directional magnetic and hydrodynamic force.

From the graph, RBCs are found to exhibit positive MAP force and vice versa for other cells. The difference in sign has indicated the forces exacted on cells will be in opposite directions. However, there is a magnitude variation among these cell types. For example, the MAP force which is subjected on the breast cancer cell is stronger in contrast to other cells. Such a condition is caused by the difference in cell volume (see Eq. (2.20)). When the calculated MAP force is compared to the calculated lift force, the lift force showed a lower order of magnitude for the analysed cell types. Under this distribution, a MAP force is dominant across the microchannel and lift force cannot disrupt the lateral motion of cells across the channel.

Notably, the separation efficiency is the ultimate performance evaluation of our propose MAP microchamber design. However, it has been shown that the concentration of cells carried by the fluid flow will affect the number of cells to be delivered toward the designated outlet under a constant velocity. To monitor the proposed MAP stage's functionality, the particle tracing post-processing plots for both whole blood and dilution ratio of 1:10 are generated. For the purpose of reducing both RAM memory usage and computation time, the simulation will be performed with 1mL blood sample. As mentioned in Chapter 2, the presence of CTC is rare in a blood sample, which is 1~10 per 7.5mL. Furthermore, previous studies shown that it exhibit similar response as WBC and platelets within a MAP stage. Considering the purpose of the MAP stage is to separate RBCs from blood sample, therefore, the tumour cell is negligible in this particle simulation. In this context, the initial concentration of cells for various dilution ratio within a 1mL sample is calculated based on Eq. (3-17). The obtained data is summarized in Table 4.1 and the simulation's setting of a particular cell concentration will be assigned accordingly to this table.

Table 4.1: Initial concentration of cells for various dilution ratio per mL

Dilution ratio	RBC	WBC	Platelets
1:0	$5.00x10^{9}$	$1.10x10^{7}$	$3.50x10^{8}$
1:10	$4.54x10^{8}$	$1.00x10^{6}$	$3.18x10^{7}$

The cell trajectories plot for both whole blood and dilution ratio of 1:10 are illustrated in Figure 4.22 and Figure 4.23, respectively. To visualize the cell motion more easily, the particles are labelled according to their magnetic susceptibility. For instance, RBC is represented with red particle. Meanwhile, other nucleated cells are represented with blue particle, as their magnetic susceptibilities are approximated to $-9x10^{-6}$ (refer to Table 2.1).

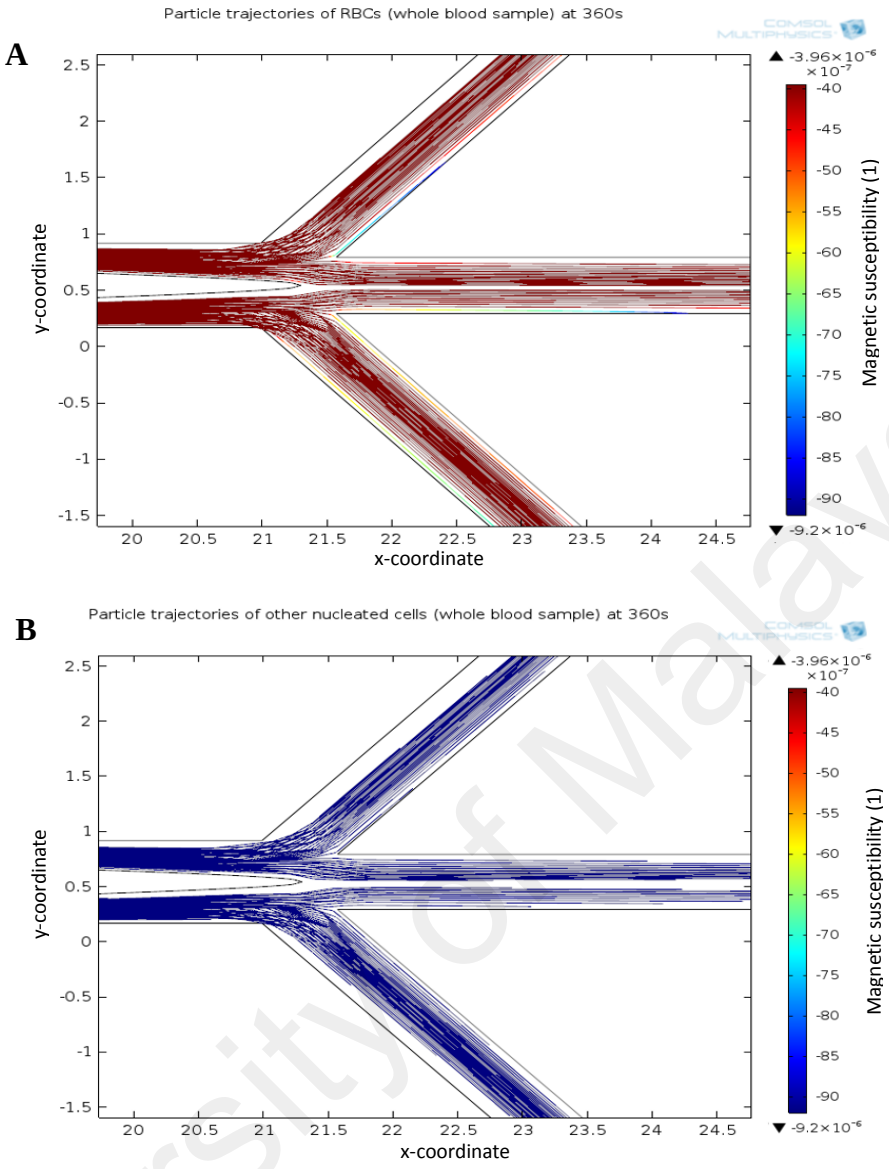

Figure 4.22: Plot of simulated blood cell trajectories within the MAP microchamber for (A) RBC and (B) other nucleated cell from a whole blood sample. The colour spectrum bar indicates the magnetic susceptibilities of cells.

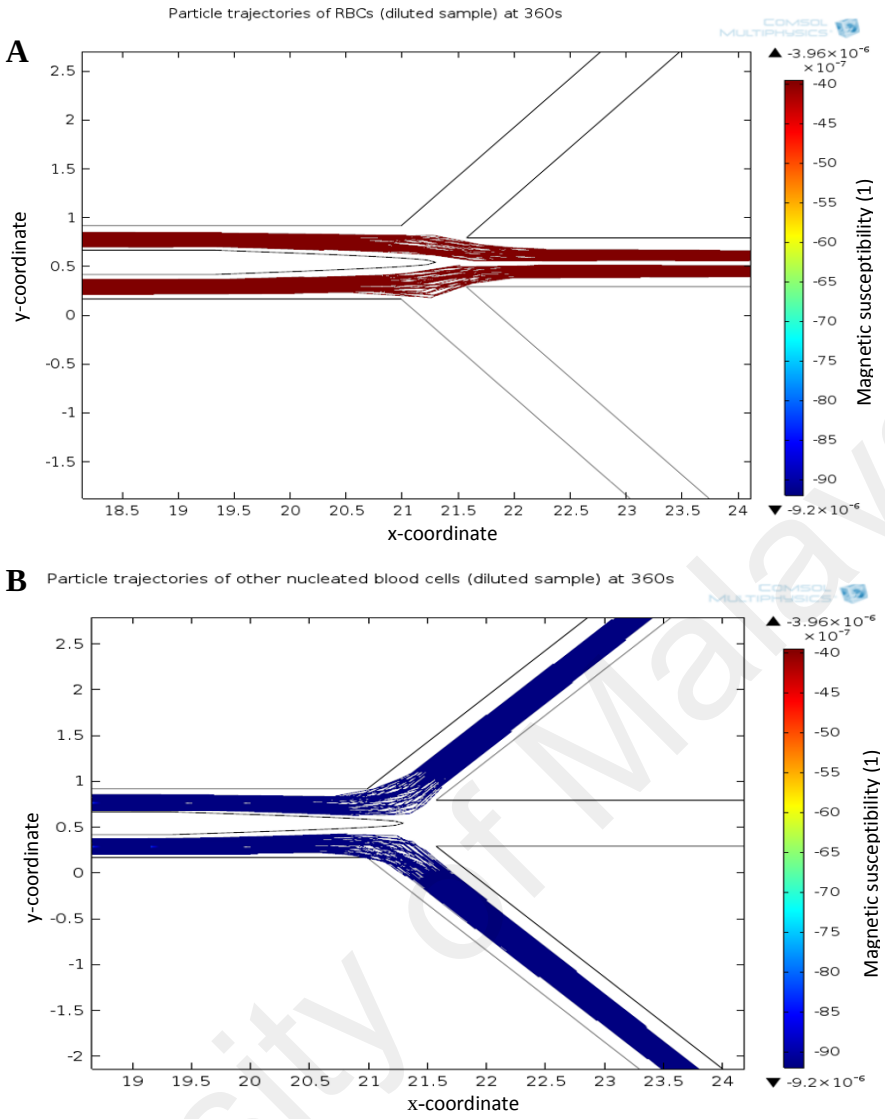

Figure 4.23: Plot of simulated blood cell trajectories within the MAP microchamber for (A) RBC and (B) other nucleated cell from a diluted blood sample. The colour spectrum bar indicates the magnetic susceptibilities of cells.

In Figure 4.22, the separation efficiency of the proposed MAP stage for whole blood sample is found to be low, whereby blood cells are directed toward the three outlets despite their difference in magnetic susceptibilities. In this case, the dense colonies of blood cells per volume concentration have inhibited the MAP force from precisely isolating cells. Meanwhile, when the dilution ratio of 1:10 (whole blood to saline) is employed, a 100% recovery rate is obtained in this simulation. As evidenced in both

Figure 4.22(A) and (B), the RBCs and other nucleated cells are directed toward central and lateral outlet, respectively.

4.3 Evaluation with Dielectrophoresis stage

The previous section has showed the proposed MAP stage to be able to separate RB from a diluted blood sample with high efficiency. Note that the planar electrode developed by Moon *et al.* (2011) will be adopted and integrated with our proposed MAP platform. These electrode are placed at the bottom of microchannel with an angle of 30° to the direction of flow. Both width and spacing of the interdigitated electrodes are 250μm. The overall microfluidic channel for integrated MAP-DEP is illustrated in Figure 4.24.

As the enriched nucleated cells will undergo a second separation at the downstream DEP stage, it is crucial for us to investigate the flow distribution and final isolation performance in this cooperative platforms.

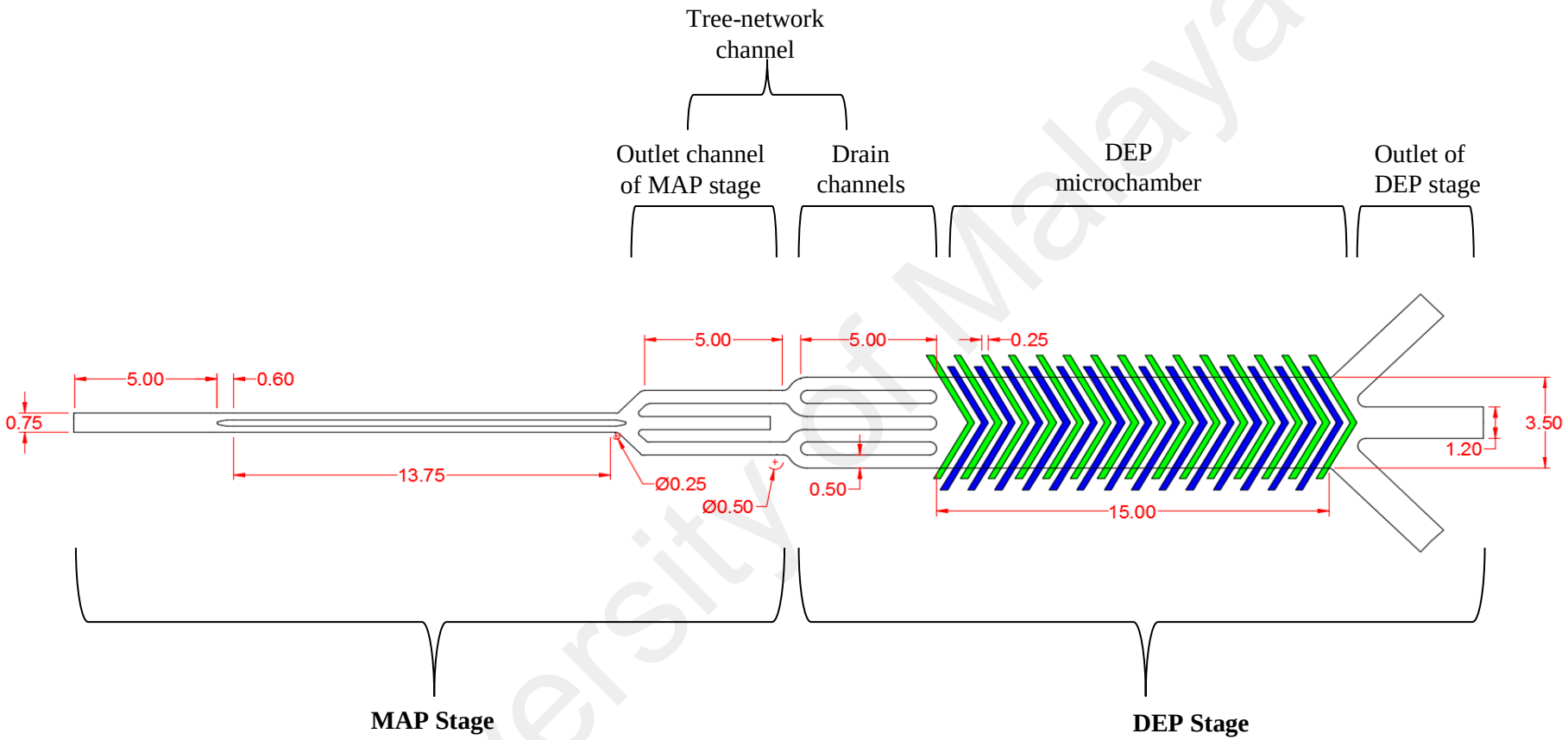

Figure 4.24: Schematic of microchannel architecture of integrated MAP-DEP microsystem.

4.3.1 Flow distribution

In order to achieve an uniform loading capacity for a given chamber size, a tree-network design from our previous study (Low *et al*., 2014) will be resorted into the geometrical design in the DEP stage. It refers to the branched channel geometry in between both MAP and DEP stages. For this particular design, the cross section and the length of a drain channel will be same with the outlet channel of the MAP stage. It is to help equalizing the hydraulic resistance within those channel and thereby generating a uniform flow distribution throughout the whole wide chamber of DEP stage. Such a condition can be defined theoretically through Hagen-Poiseulle's equation, which stated the flow rate, Δp, within the channel is equivalent to:

$$\Delta p = QL \qquad \textbf{4-21}$$

where Q and L represent the volumetric flow and length of each drain channel respectively. Due to both outlet and their bifurcated channel are symmetrical to each other, the equation of volumetric flow in each network can be modelled as:

$$Q_{M\_outlet1} \cdot L_{M\_outlet1} = Q_{D\_inlet1} \cdot L_{D\_inlet1} + Q_{D\_inlet\ 2} \cdot L_{D\_inlet\ 2} \qquad \textbf{4-22}$$

in which subscript M_outlet and D_inlet represents the outlet channel of MAP and its bifurcated drain channels respectively. It has been known that the lengths of all sub-channels are same. Therefore, the equation can be further simplified to:

$$Q_{M\_outlet1} = Q_{D\_inlet1} + Q_{D\_inlet\ 2} \qquad \textbf{4-23}$$

From Eq. (4-23), the presence of tree-network channel will distribute the volumetric flow from a MAP outlet channel into two daughter channels. Consequently the acceleration of meniscus at the outlet zone of MAP and entry zone of DEP will be flattened. Such a condition has been validated through a surface plot of velocity profile as presented in Figure 4.25.

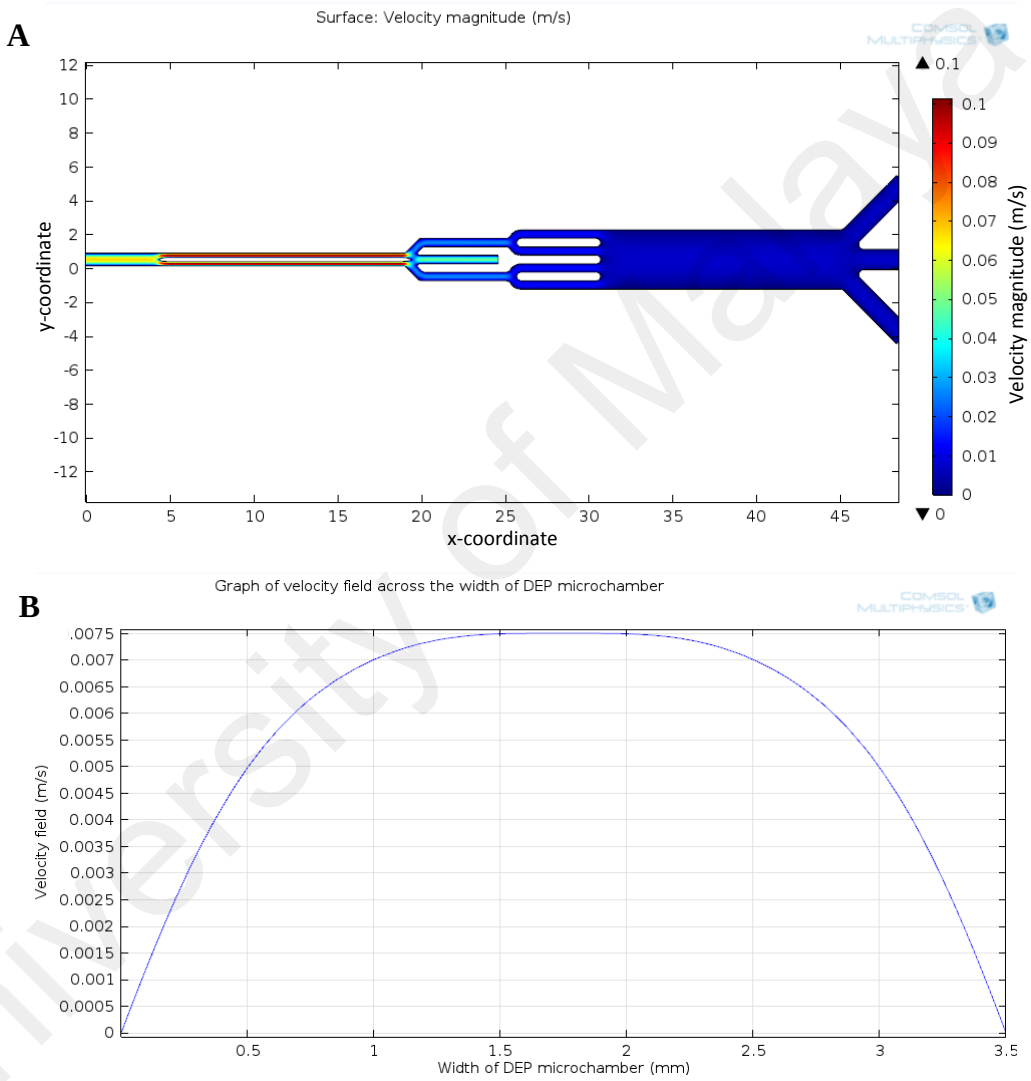

Figure 4.25: (A) Surface plot velocity of microfluidic channel for the integrated DEP-MAP microdevice. (B) Graph of velocity field across the middle width of DEP microchamber.

In Figure 4.25 (A), the presence of tree-network channel is found to enhance a uniform distribution of flow across the DEP chamber, where an evenly blue spectrum is obtained around the microfluidic chamber with COMSOL simulation. Such a condition

can be further proved by the plotted graph in Figure 4.25 (B). A quadratic-shaped velocity profile which indicates a stable uniform flow is detected across the middle width of DEP microchamber. Thus, the non-uniform distribution of particles that are established at the outlet of MAP stages will be removed by these downstream channels.

4.3.2 DEP force and cell trajectories

To initiate the DEP separation, the electrode array will be connected to a 1MHz and 15 Vp-p sinusoidal voltage. From a theoretical perspective, an interdigitated electrode array with an applied voltage can be modelled more simply as line charges placed on edges of the electrode. As such, the electrode array which is coloured with blue and green in Figure 4.24 will be connected to a positive or negative voltage terminal, respectively

Analogously to MAP stage, the DEP force is proportional to the gradient of electric field, as given in Eq. (2-7). The computational method is thereby applied to analyse the distribution of the electric field within the microchannel. Its simulated result is shown in Figure 4.26.

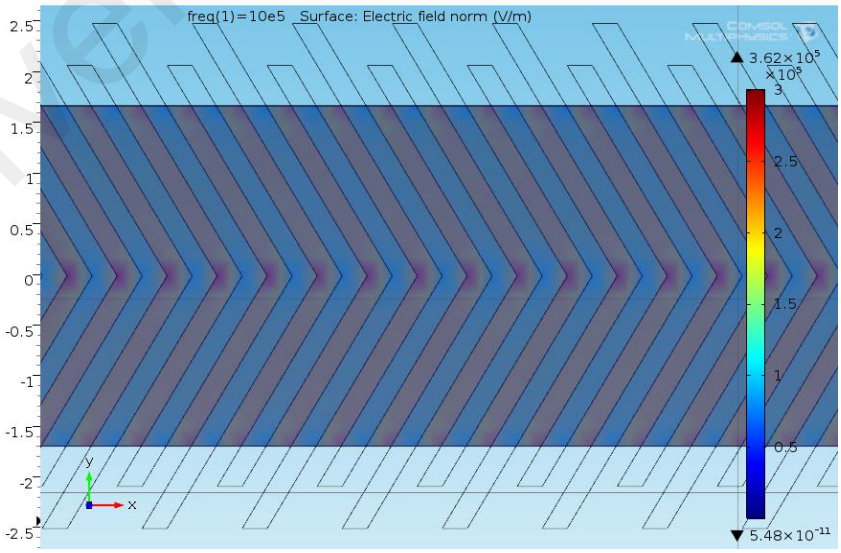

Figure 4.26: Surface plot of electric field**.**

In general, the surface plot shows a high electric field density at the gap between the interdigitated electrodes. The E_{rms} reaches a maximum value of $3.62x10^5$V/m at the middle pointy region of microelectrodes with a total distance of 200µm. Such a condition is in agreement with study conducted by Körge *et al.* (2013). Their study stipulated that the high degree curvature of a sharp point has caused an accumulation of electrons at this region, thus developed a high electric field. Owning to this configuration, the microelectrode creates a difference between the maximum and an average electric field and therefore enable a formation of DEP force.

As fore-mentioned in Chapter 3, both DEP force and hydrodynamic force will dominate the motion of cancer cells within the channels toward their designated outlets. For this reason, a distribution of $\mathbf{F_{DEP}}$ and $\mathbf{F_{HDY}}$ at 100µm off the microchannel centreline along the x-axis (length), y-axis (width) and z-axis (height) had been investigated (see Figure 4.27). The variation of forces along these lines are computed with MATLAB by applying Eq. (2-7) and (3-3) whereby the numerical data for both DEP and hydrodynamic force are respectively imported from the surface plot in Figure 4.25 and Figure 4.26. As shown in Figure 4.26, the inner microelectrode pairs experience similar condition. Henceforth, for the calculation of both DEP and hydrodynamic force, the plotted boundary condition is shortened to an area which houses only three microelectrode pairs. Additionally, both DEP and velocity field is symmetric with respect to the centreline of the microchannel. Therefore, the data obtained from half of the microchannel is analysed. Such a simulation method can help reducing the number of elements thus decreasing the computation time significantly. As for DEP force, previous study has shown that it will decay with distance from microelectrode (Moon *et al.*, 2011). Therefore, these forces will be measured at three additional lines, which lie at height of 0.125mm, 0.25mm and 0.37mm. Nevertheless, it should be noted that the cell motion under DEP field is dependent on the sign of the real

part (Re) of Clausius-Mossotti (CM) factor (see Section 4.1). To ease the analysis for a group of cell with various dielectric phenotypes, this factor will remain neutral and represented with Re in plotted graph. The graph of forces generated along the length, width and height of DEP microchamber is delivered in Figure 4.28.

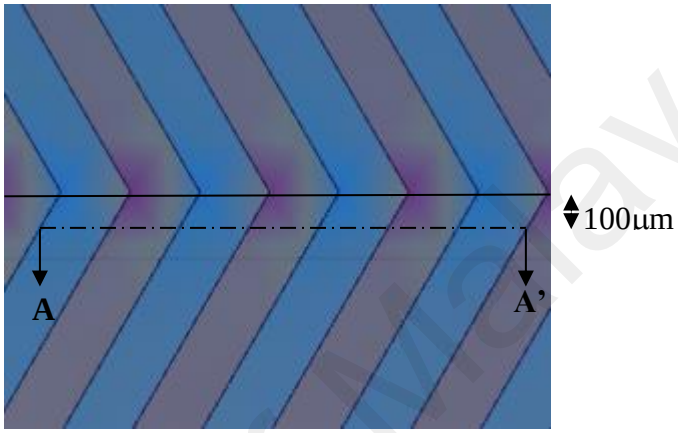

Figure 4.27: Illustration of a DEP device cross-section (A-A') for forces measurement.

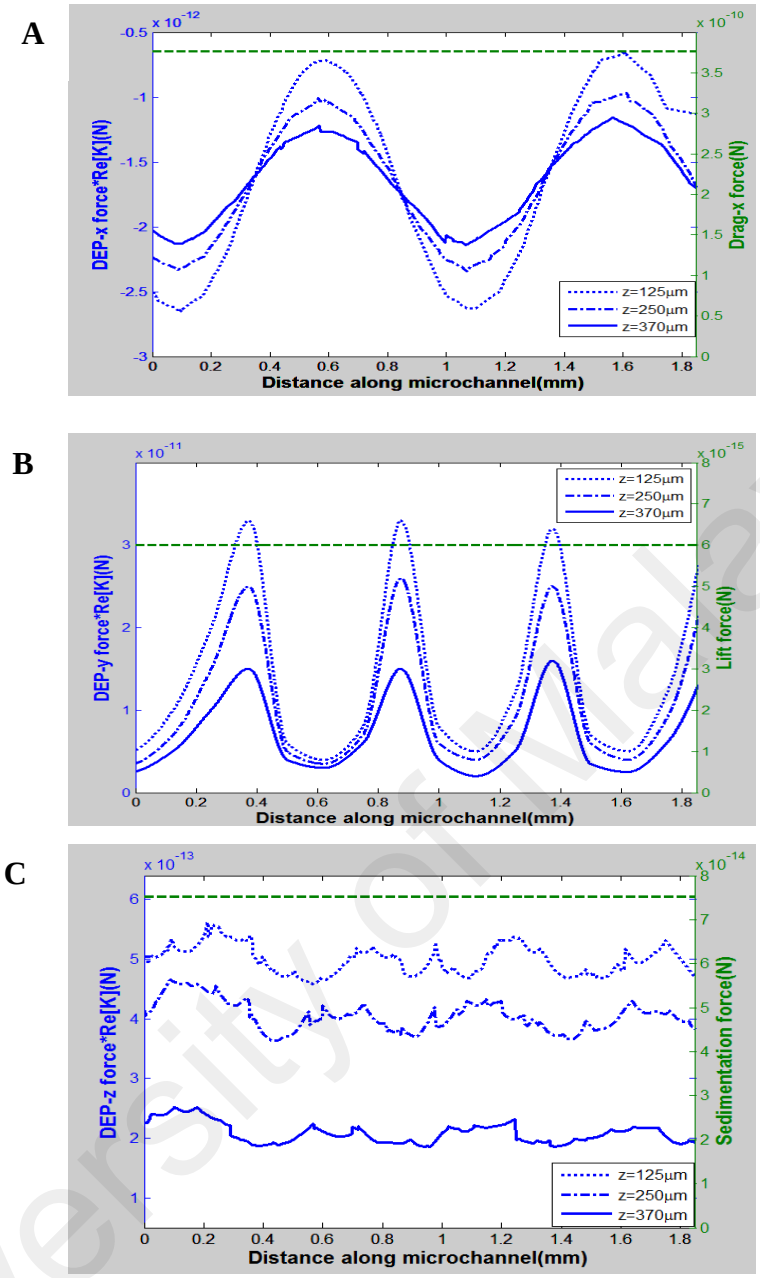

Figure 4.28: Variation of DEP force and hydrodynamic force in (A) x-direction, (B) y-direction and (C) z-direction along the lines that are located 100 µm off the microchannel centreline.

From these graph, it can been seen that the variation of DEP forces are almost similar along the three lines for all plotted graph. For cell with positive CM factor (such as CTC), the generated graph will remain unmodified. Meanwhile, cell with negative CM-factor would have opposite sign of the y-coordinate. Therefore, the induced response will be vice versa in contrast to the target cells. As illustrated in Figure 4.28 (A), the

magnitude of drag force is 3.75×10^{-10} N, which is at least 10 times larger than the DEP force. Such a condition indicates that the hydrodynamic force is the dominant force along the microchannel, and DEP force will not influence the movement of cells along the x-axis. On the other hand, DEP-y force has higher magnitude compared to the lift force. Under this distribution, the flow cannot disrupt the lateral motion of cells across the microchannel. As illustrated in Figure 4.28(B), the DEP-y force will be increased at the inner-gap between microelectrode region and hence accelerating the cell, while it becomes negative after the region thus decelerating the cells. Similar to DEP-y force, DEP z-force (see Figure 4.28(C) is higher compared to a sedimentation force. Such a condition will result in cells with positive CM factor such as CTC to be attracted toward the microelectrode at the bottom surface of microchannel, and vice versa for white blood cells and platelet. As shown in this figure, the force will decrease along the height of the microchannel. This is in line with the results provided by Gascoyne *et al.* (2014) suggesting that a DEP-z force decays exponentially along z-axis. As both DEP-y force and drag force has higher magnitude compare to these forces, the forces along z-direction would have insignificant effect and thus can be ignored.

When a concentrated nucleated cell from MAP stage is directed into DEP stage, the movement of cell passing on these interdigitated electrode array is illustrated in Figure 4.29.

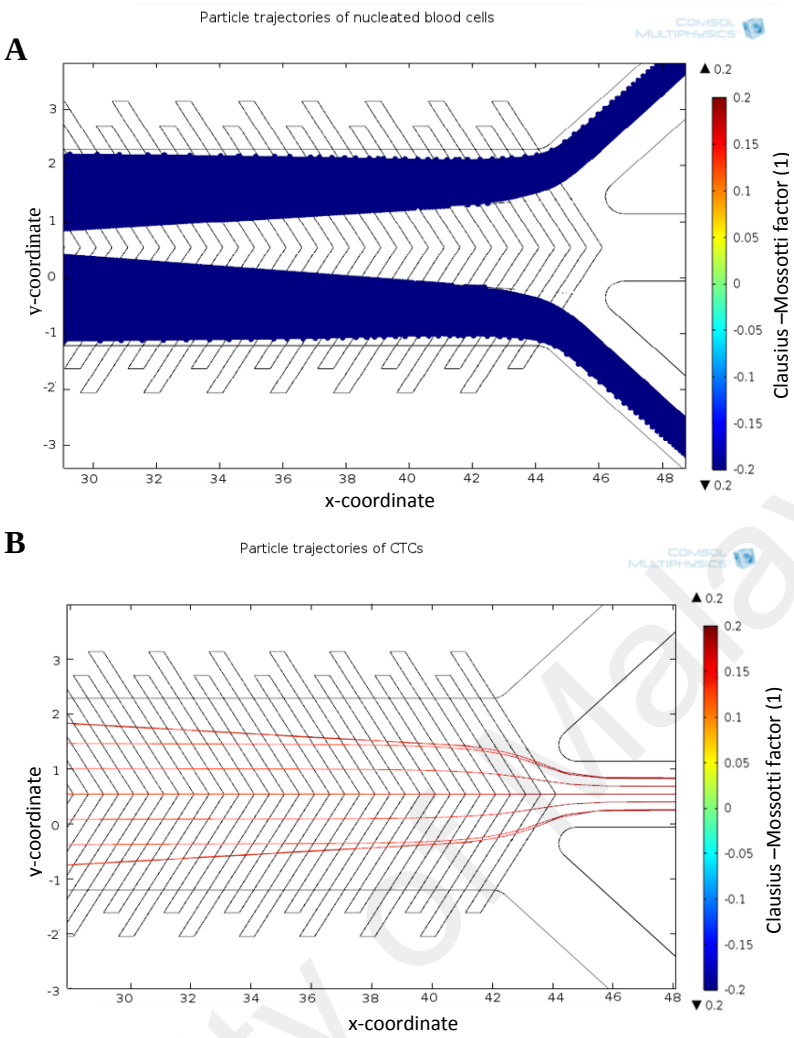

Figure 4.29: Plot of simulated blood cell trajectories within a microchannel in a presence of DEP for (A) concentrated nucleated blood cell and (B) CTCs from MAP stage. The colour spectrum bar indicates the Clausius-Mossotti factor of cells.

In this figure, a CTC is found to manifest opposite response in contrast to other nucleated cells. Aforementioned, the middle part of a DEP stage consists of high electric field region. As a CTC exhibits pDEP (CM factor >0), it will be deviated toward this region and flows into the central outlet. On the contrary, nDEP force (CM factor <0) pushes normal nucleated cell toward the low electric field region along the channel wall.

Comparing to DEP-FFF technique as discussed in literature, the use of MAP as pre-enrichment stage has eliminated the cell overloading problem within the DEP stage,

thus enhance the separation efficiency. By removing the RBCs, it reduces the blood medium's conductivity thus enable a CM factor difference to be present between target cells and blood cells for a DEP device. Therefore, a MAP stage should be adopted as a new integrated technique to be cooperated in a DEP system to isolate CTC from blood cells.

4.4 Limitation of this study

Although the present study has yielded some preliminary findings, its design is not without flaws. A number of caveats need to be noted regarding the present study.

First and foremost, the proposed microfluidic design for DEP application is solely based on numerical analysis. However, this simulation might not reflect the real condition during the experimental platform analysis. For instance, errors which occur during fabrication process of the microfluidic channel will influence cell motion, thus affecting their distribution within the microfluidic chamber. Furthermore, storage-related activity deterioration of blood components might occur during the actual experiment and affect the device's efficiency. These conditions have not been considered in our simulation due to the limited precision of data for cells which have high conductivity or closer bonding. Therefore, there is a need for experimental characterization to verify the design strategy and simulation.

Notably, blood contains a myriad of information about the functioning of a human body. Thus, a complete blood analysis has been a primary diagnostic test in healthcare system. However, due to its massive number and wide diversity of cell types, fractioning various target components from a whole blood sample has been a technical challenge for microfluidics. In this study, the proposed MAP-DEP platform demonstrated a dramatic reduction in capture efficiency when a whole blood sample is employed. The dilution is necessitated prior to the experiment to enhance the separation

efficiency. Nevertheless, for these blood-based separation systems to be realized as true point-of-care (POC) devices, the techniques must be simple, easy to be use and with little or no sample preparation required. Consequently, a MAP-DEP separation platform which capable of unaltered blood cell analysis is needed to be developed for accomplishing the ultimate goal in point-of-care devices.

CHAPTER 5:

CONCLUSION AND FUTURE WORKS

5.1 Conclusion

Overall, the present work was set out with the objective to solve the limitation of dielectrophoresis (DEP) technique in CTC isolation. The general strategy of achieving this aim was by developing a magnetophoresis (MAP) system as a pre-enrichment stage. Using this strategy, RBCs was first be removed from a blood sample in MAP stage, thus allowing DEP stage to focus on isolation of targeted rare cells from the concentrating nucleated cells. Several computational models were employed to demonstrate the proof-of-concept of our proposed method for enhancing the device separation efficiency. These models were discussed in Chapter 3, whereby the partial differential equations that govern each physical process (e.g. electric, magnetic and hydrodynamic forces) were solved with Lagrangian-Eulerian CFD based numerical scheme, A set of design criteria for MAP stage that contributed to its capture performance was investigated, including permanent magnet orientation, magnet track configuration, fluid flow parameter and the separation efficiency.

From the simulation that was carried out (see Chapter 4), the removal of RBC was found to reduce the blood medium's conductivity thus enable a CM factor difference to be present between target cells and blood cells. To enhance the cell separation in a downstream DEP stage, the MAP platform which facilitated the high RBC recovery rate was designed and optimized via computational modelling analysis. Via this study, a single permanent magnet configuration was found to generate desirable magnetic field phenomena within a microfluidic channel, as such a magnetic field was gradually decreased from the channel wall next to a permanent magnet. In order to amplify low magnetic forces on blood cells, a ferromagnetic track with the width of 250μm and a

length of 15mm was tapered in the middle of the MAP microchamber. This strategy has generated a higher value of magnetic field's gradient, averaging 49T/m^2. Besides, from the perspective of Navier-Stokes principle, the positioning of ferromagnetic track in the middle of microchannel created a hydraulic resistance within the bifurcated channel, thus resulting in a uniform flow velocity. In order to improve the uniformity of cell deposition around the sharp turn region, a rounded corner was adapted into our proposed design. The generated surface plot has shown a better flow and magnetic field distribution in contrast to our original proposed MAP platform design. When cell trajectory within a finalized MAP stage was computed with a particle tracing module, a high separation efficiency of RBC was obtained for blood sample corresponded to a dilution ratio of 1:10. Notably, the enriched nucleated cell from MAP stage will undergo second separation in DEP stage. To inspect the overall recovery rate of the integrated platform, the particle motion of cell directed toward the DEP stage (which was adopted from Moon et *al.* (2012) study) has been studied. A tree-network microchannel architecture was implemented onto the DEP stage to generate a uniform loading capacity of a given microchamber size.

In short, the proposed cooperative platform utilising MAP-DEP separation modalities reduced the overloading cell issues within a DEP stage, thus the enhanced capture. Furthermore, the computational model which was portrayed in this paper has offered a rational design of systems in advance of fabrication and should be of considerable interest to researchers in the future development of lab-on-chip system. This study therefore propose that, as the need for more accurate separations in CTC detection, approaches combining DEP stage with a MAP stage will be the optimal means to achieve this metrics.

5.2 Future Works

The result portrayed by the dissertation has offered some interesting directions for future works. A brief summary of recommendation is provided below:

- The COMSOL models in this study mainly employ the coupling of Incompressible Navier-Stokes, electric field and magnetostatics mode. Future models should investigate the use of other physics modes such as multiple-phase flow module. Such a model can simulate the flow of two or more immiscible fluids while taking into consideration of both gravity and surface tension. Furthermore, the suggested module allows cells to be simulated as viscous fluids individually, thus enabling the investigation of dielectric and magnetic force on the targeted cell surface.
- Future work should engage in the fabrication of the proposed device to prove the benefits of its application in CTCs detection. The main challenge of our proposed device fabrication is the technique used to embed the ferromagnetic track in the middle of the microfluidic channel. One potential method for fabrication would be layer-by-layer approach, wherein the ferromagnetic element is formed via a sequence of spin coating, patterning, etching, deposition and planarization followed by the removal of sacrificial material to form the flow channel (Carr *et al.*, 2009). Some challenges with this approach include the time required for the precision in patterning and depositing a ferromagnetic track, the potential for detrimental residual stress in the system, and the ability to etch a flow channel with uniform cross-sectional dimensions with the elements in space (Li *et al.*, 2014). An alternative method would be using 3D printing to form the system and insert the ferromagnetic elements relatively during fabrication.

- Validation of models should be performed to determine their accuracy. Such a validation can be done experimentally in vitro via the use of flow cytometry. Flow cytometry identifies and counts the number of cells passing a certain location or removed from the outlet of microfluidic channel using the particle's fluorescence and an optical detection system. It can be used to monitor the number of cells collected from the outlet of the microfluidic channel when the force exacted in a platform is both present and absent. Noted that the recovery rate of a target cell for the proposed microfluidic platform draws the main concern in this study. Therefore, the cell counts obtained from flow cytometry can be converted to a volume fraction for comparison with the collected sample in simulation. Besides, the trajectory of cell along the chamber can be measured by a CCD type camera to obtain their real time velocity field as well as the deviation route.
- Notably, maintenance of cell viability is an imperative feature of label-cell separation procedure because the captured living cells are needed for downstream phenotypic and genotypic analyses. A systemic investigation of electrical and magnetic field effect that may influence cell integrity and viability should be included in the future experimental study. The viability test can be done by dye exclusion techniques where cells are incubated with a dilute solution of dye which only enter dead cells.
- A velocity field is important in generating uniform cell distribution. It must be noted that the velocity field across the chamber is reliant extensively on the external pressure sources. In this case, a syringe pump is widely practised in most of the research to supply constant fluid flow into microfluidic channel. This device consists a standard injection syringe fitted with an intravenous needle, whereby the flow rate developed by such a system is completely

dependent on the syringe cross-section as well as how fast a user push in the cell suspension. However, the flow developed by such a system do not allow precise velocity control for microfluidic research. To combat this issue, a gear drive mechanism has been invented to replace human hand force in depress the plunger in recent year . Despite of this improvements, a flow pulsation which is generated by this mechanical actuation can be very disturbing, especially for viscous fluids at low flow rates. The response and setting time can be quite long, as such >15 minutes to reach a steady flow (Zhang, Chen, & Huang, 2015). Therefore, for the sake of future research, an independent and constant source needed to be introduced. It can be done by design a pressure generator to help tuning the applied pressure on plunger automatically. This device can be preprogramed for specific experiment setting, with flow rates, volume limits and alarm setting adjusted for each. Besides, the trajectory of cell along the chamber can be measured by a CCD type camera to obtain their real time velocity field as well as the deviation route.

REFERENCES

Abdalla, S., Al-ameer, S. S., & Al-Magaishi, S. H. (2010). Electrical properties with relaxation through human blood. *Biomicrofluidics, 4*(3), 034101.

Abdul Razak, M. A., Hoettges, K. F., Fatoyinbo, H. O., Labeed, F. H., & Hughes, M. P. (2013). Efficient dielectrophoretic cell enrichment using a dielectrophoresis-well based system. *Biomicrofluidics, 7*(6), 64110.

Abdullah, N. A., Mahiyuddin, W. R. W., Muhammad, N. A., Ali, Z. M., Ibrahim, L., Tamim, N. S. I., Mustafa, A. N., & Kamaluddin, M. A. (2013). Survival Rate of Breast Cancer Patients In Malaysia: A Population-based Study. *Asian Pacific Journal of Cancer Prevention, 14*(8), 4591-4594.

Abonnenc, M., Gassner, A. L., Morandini, J., Josserand, J., & Girault, H. H. (2009). Magnetic track array for efficient bead capture in microchannels. *Anal Bioanal Chem, 395*(3), 747-757.

Adams, J., Olson, N., & Rawlins, J. (2015). Microfluidic Final Report: University of Lincoln.

Albrecht, M., Furubayashi, T., Przybylski, M., Korecki, J., & Gradman, U. (1992). Magnetic step anisotropies. *Journal of Magnetism and Magnetic Materials, 113*(1–3), 207-220.

Alix-Panabieres, C., & Pantel, K. (2014). Technologies for detection of circulating tumor cells: facts and vision. *Lab Chip, 14*(1), 57-62.

Andreu, J. S., Barbero, P., Camacho, J., & Faraudo, J. (2012). Simulation of Magnetophoretic Separation Processes in Dispersions of Superparamagnetic Nanoparticles in the Noncooperative Regime. *Journal of Nanomaterials, 2012*, 1-10.

Anoshkina, Y., Costas-Rodriguez, M., & Vanhaecke, F. (2015). High-precision Fe isotopic analysis of whole blood for biomedical purposes without prior isolation of the target element. *Journal of Analytical Atomic Spectrometry, 30*(8), 1816-1821.

Antolovic, D., Galindo, L., Carstens, A., Rahbari, N., Buchler, M. W., Weitz, J., & Koch, M. (2010). Heterogeneous detection of circulating tumor cells in patients with colorectal cancer by immunomagnetic enrichment using different EpCAM-specific antibodies. *BMC Biotechnol, 10*, 35.

Armitage, W. J. (1985). Effect of solute concentration on intracellular water volume and hydraulic conductivity of human blood platelets. *Journal of Physiological, 1986*(374), 374-385.

Arya, S. K., Lim, B., & Rahman, A. R. A. (2013). Enrichment, detection and clinical significance of circulating tumor cells. *Lab Chip, 13*(11), 1995-2027.

Association, M. M. P. (2014). Standard Specifications for Permanent Magnet Materials (Vol. 0100-00, pp. 25). Chicago: International Electrotechnical Commision.

Azaman, Kadri, N. A., & Abu Osman, N. A. (2013). *Electromagnetic flux modeling of AC field over planar microarray dot electrodes used in dielectrophoretic lab on a chip device.* Paper presented at the World Congress on Medical Physics and Biomedical Engineering, IFMBE Proceeding, Beijing.

Baccelli, I., Schneeweiss, A., Riethdorf, S., Stenzinger, A., Schillert, A., Vogel, V., Klein, C., Saini, M., Bauerle, T., Wallwiener, M., Holland-Letz, T., Hofner, T., Sprick, M., Scharpff, M., Marme, F., Sinn, H. P., Pantel, K., Weichert, W., & Trumpp, A. (2013). Identification of a population of blood circulating tumor cells from breast cancer patients that initiates metastasis in a xenograft assay. *Nat Biotechnol, 31*(6), 539-544.

Balasubramanian, P., Wang, L., Lawrence, S. M., Navas, T., Kummar, S., Hollingshead, M., Owusu, F., Parchment, R. E., Tomaszewski, J. E., Doroshow, J. H., & Kinderss, R. J. (2014). Isolation and characteriztion of circulating tumor cells from peripheral blood: specimens of patients with advanced solid tumor malignancies (using ApoStream Instrumentation).

Balic, M. (2013). *Disseminating breast cacner stem cells and their molecular characterization.* (Ph.D Degree of Doctor of Medical Science), Medical University of Graz.

Becker, F. F., Wang, X.-B., Huang, Y., Pethig, R., Vykoukal, J., & Gascoyne, R. C. (1995). Separation of human breast cancer cells from blood by differential dielectric affinity. *Cell Biology, 92*, 860-864.

Bhagat, A., Bow, H., Hou, H., Tan, S., Han, J., & Lim, C. (2010). Microfluidics for cell separation. *Medical & Biological Engineering & Computing, 48*(10), 999-1014.

Bodensteiner, D. C. (1989). A flow cytometric technique to accurately measure post ‐ filtration white blood cell counts. *Transfusion, 29*(7), 651-653.

Broche, L. M., Bhadal, N., Lewis, M. P., Porter, S., Hughes, M. P., & Labeed, F. H. (2007). Early detection of oral cancer – Is dielectrophoresis the answer? *Oral Oncology, 43*(2), 199-203.

Carr, C., Espy, M., Nath, P., Martin, S. L., Ward, M. D., & Martin, J. (2009). Design, fabrication and demonstration of a magnetophoresis chamber with 25 output fractions. *J Magn Magn Mater, 321*(10), 1440-1445.

Chen, D. F., Du, H., & Li, W. H. (2006). A 3D paired microelectrode array for accumulation and separation of microparticles. *Journal of Micromechanics and Microengineering, 16*(7), 1162.

Chen, J., Abdelgawad, M., Yu, L., Shakiba, N., Chien, W.-Y., Lu, Z., Geddie, W. R., Jewett, M. A. S., & Sun, Y. (2011). Electrodeformation for single cell mechanical characterization. *Journal of Micromechanics and Microengineering, 21*(5), 054012.

Chen, J., Li, J., & Sun, Y. (2012). Microfluidic approaches for cancer cell detection, characterization, and separation. *Lab Chip, 12*(10), 1753-1767.

Chen, P., Huang, Y. Y., Hoshino, K., & Zhang, J. X. (2015). Microscale magnetic field modulation for enhanced capture and distribution of rare circulating tumor cells. *Sci Rep, 5*, 8745.

Chen, P., Huang, Y. Y., Hoshino, K., & Zhang, X. (2014). Multiscale immunomagnetic enrichment of circulating tumor cells: from tubes to microchips. *Lab Chip, 14*(3), 446-458.

Chen, X., Cui, D., & Jian, C. (2012). Microfluidic devices targeting blood cell lysis. In C. Xing (Ed.), *On-chip pretreatment of whole blood by using MEMS technology*. USA: Bentham ebook

Cheng, X., Liu, Y., Irimia, D., Demirci, U., Yang, L., Zamir, L., Rodríguez, W. R., Toner, M., & Bashir, R. (2007). Cell detection and counting through cell lysate impedance spectroscopy in microfluidic devices. *Lab Chip*, *7*(6), 746-755.

Chow, A. Y. (2010). Cell cycle control by oncogenes and tumor suppressors: driving the transformation of normal cells into cancerous cells. *Nature Education*, *3*(9).

Cima, I., Wen Yee, C., Iliescu, F. S., Min Phyo, W., Hon Lim, K., Iliescu, C., & Han Tan, M. (2013). Label-free isolation of circulating tumor cells in microfluidic devices: Current research and perspectives. *Biomicrofluidics*, *7*(1), 11810.

Ciprian, I., Guo Lin, X., Poh Lam, O., & Kwong Joo, L. (2007). Dielectrophoretic separation of biological samples in a 3D filtering chip. *Journal of Micromechanics and Microengineering*, *17*(7), S128.

Corchero, J. L., & Villaverde, A. (2009). Biomedical applications of distally controlled magnetic nanoparticles. *Trends in biotechnology*, *27*(8), 468-476.

Cormack, D. H. (2001). *Essential Histology*. Pennsylvania: Lipponcott Williams& Wilkins.

Coumans, F. A., van Dalum, G., Beck, M., & Terstappen, L. W. (2013). Filter characteristics influencing circulating tumor cell enrichment from whole blood. *PLoS One*, *8*(4), e61770.

Culp, L. A., Lin, W. c., Kleinman, N. R., O'Connor, K. L., & Lechner, R. (1998). Earliest Steps in Primary Tumor Formation and Micrometastasis Resolved with Histochemical Markers of Gene-tagged Tumor Cells. *Journal of Histochemistry & Cytochemistry*, *46*(5), 557-567.

Dalum, G. v., Holland, L., & Terstappen, L. W. (2012). Metastasis and circulating tumor cells. *Journal of the International Federation of Clinical Chemistry and Laboratory Medicine*, *23*(3).

Dash, S., & Mohanty, S. (2014). Dielectrophoretic separation of micron and submicron particles: A review. *ELECTROPHORESIS*, n/a-n/a.

Dimitrov, D. S. (1995). Electroporation and electrofusion of membranes. In R. Liposky & E. Sackmann (Eds.), *Handbook of biological physics* (Vol. 1). U.S.A: Elsevier Science B.V

Dobrzynska, I., Skrzydlewska, E., & Figaszewski, Z. A. (2013). Changes in electric properties of human breast cancer cells. *J Membr Biol, 246*(2), 161-166.

Elblbesy, M. A. (2010). Effect of static magnetic field on erythrocytes characterizations. *Journal of Biomedical Science and Engineering, 03*(03), 300-303.

Emerson, D. R., Cieslicki, K., Gu, X., & Barber, R. W. (2006). Biomimetic design of microfluidic manifolds based on a generalised Murray's law. *Lab on a Chip, 6*(3), 447-454.

Esmaeilsabzali, H., Beischlag, T. V., Cox, M. E., Parameswaran, A. M., & Park, E. J. (2013). Detection and isolation of circulating tumor cells: principles and methods. *Biotechnol Adv, 31*(7), 1063-1084.

Fabbri, F., Carloni, S., Zoli, W., Ulivi, P., Gallerani, G., Fici, P., Chiadini, E., Passardi, A., Frassineti, G. L., Ragazzini, A., & Amadori, D. (2013). Detection and recovery of circulating colon cancer cells using a dielectrophoresis-based device: KRAS mutation status in pure CTCs. *Cancer Lett, 335*(1), 225-231.

Fishel, L. A. (2010). Dilution Confusion: Conventions for Defining a Dilution. *Journal of Chemical Education, 87*(11), 1183-1185.

Forbes, T. P., & Forry, S. P. (2012). Microfluidic magnetophoretic separations of immunomagnetically labeled rare mammalian cells. *Lab Chip, 12*(8), 1471-1479.

Frangioni, J. V. (2008). New technologies for human cancer imaging. *J Clin Oncol, 26*(24), 4012-4021.

Friend, J., & Yeo, L. (2010). Fabrication of microfluidic devices using polydimethylsiloxane. *Biomicrofluidics, 4*(2), 026502.

Furiani, E. P. (2007). Magnetophoretic separation of blood cells at microscale. *Journal of Applied Physics, 40*(5), 1313.

Gagnon, Z. (2011). Cellular Dielectrophoresis: Applications to the Characterization, Manipulation, Separation and Patterning of Cells. *Electrophoresis, 32*(18), 2466-2487.

Gagnon, Z., Mazur, J., & Chang, H.-C. (2010). Integrated AC electrokinetic cell separation in a closed-loop device. *Lab on a Chip, 10*(6), 718-726.

Gascoyne. (2002). *Tumor Markers: Physiology, Pathobiology, Technology and Clinical Applications*. U.S.A: Amer. Assoc. for Clinical Chemistry.

Gascoyne, & Shim, S. (2014). Isolation of circulating tumor cells by dielectrophoresis. *Cancers (Basel), 6*(1), 545-579.

Gascoyne, P. R., Wang, X. B., Huang, Y., & Becker, F. F. (1997). Dielectrophoretic Separation of Cancer Cells from Blood. *IEEE Trans Ind Appl, 33*(3), 670-678.

Gassner, A. L., Abonnenc, M., Chen, H. X., Morandini, J., Josserand, J., Rossier, J. S., Busnel, J. M., & Girault, H. H. (2009). Magnetic forces produced by rectangular permanent magnets in static microsystems. *Lab Chip, 9*(16), 2356-2363.

Gaudin, N., & Terrasse, V. (2013). Latest world cancer statistics *Global cancer burden rises to 14.1 milion new cases in 2012: Marked increase in breast cancers must be addressed* (Vol. 2014). Lyon, Geneva: International Agency for Research on Cancer.

Gaw, R. L., Cornish, B. H., & Thosmas, B. J. (2007). *Comparison of a theoretical impedance model with experimental measurements of pulsatile blood flow*. Paper presented at the 13th International Conference on Electrical Bioimpedance and 8th Conference on Electrical Impedance Tomography 2007, Graz, Austria.

Geislinger, T. M., & Franke, T. (2014). Hydrodynamic lift of vesicles and red blood cells in flow--from Fahraeus & Lindqvist to microfluidic cell sorting. *Adv Colloid Interface Sci, 208*, 161-176.

Gerges, N., Rak, J., & Jabado, N. (2010). New technologies for the detection of circulating tumour cells. *Br Med Bull, 94*, 49-64.

Gonzalez, C. F., & Remcho, V. T. (2005). Harnessing dielectric forces for separations of cells, fine particles and macromolecules. *Journal of Chromatography A, 1079*(1–2), 59-68.

Gupta, V., Jafferji, I., Garza, M., Melnikova, V. O., Hasegawa, D. K., Pethig, R., & Davis, D. W. (2012). ApoStream(™), a new dielectrophoretic device for antibody independent isolation and recovery of viable cancer cells from blood. *Biomicrofluidics, 6*(2), 024133.

Han, K. H., & Frazier, A. B. (2006). Paramagnetic capture mode magnetophoretic microseparator for blood cells. *IEE Proc Nanobiotechnol, 153*(4), 67-73.

Han, S.-I., Lee, S.-M., Joo, Y.-D., & Han, K.-H. (2011). *Lateral dielectrophoretic microseparators for detecting hematological disorders*. Paper presented at the 15th International Conference on Miniaturized Systems for Chemistry and Life Sciences, Seattle, Washington, USA.

Harouaka, R. A., Nisic, M., & Zheng, S. Y. (2013). Circulating tumor cell enrichment based on physical properties. *J Lab Autom, 18*(6), 455-468.

Hart, I. R., & Fidler, I. J. (1980). Role of organ selectivity in the determination of metastatic patterns of B16 melanoma. *Cancer Res, 40*(7), 2281-2287.

Hoeppener, A. E., Swennenhuis, J. F., & Terstappen, L. W. (2012). Immunomagnetic separation technologies. *Recent Results Cancer Res, 195*, 43-58.

Hofman, V. J., Ilie, M. I., Bonnetaud, C., Selva, E., Long, E., Molina, T., Vignaud, J. M., Flejou, J. F., Lantuejoul, S., Piaton, E., Butori, C., Mourad, N., Poudenx, M., Bahadoran, P., Sibon, S., Guevara, N., Santini, J., Venissac, N., Mouroux, J., Vielh, P., & Hofman, P. M. (2011). Cytopathologic detection of circulating tumor cells using the isolation by size of epithelial tumor cell method: promises and pitfalls. *Am J Clin Pathol, 135*(1), 146-156.

Hong, B., & Zu, Y. (2013). Detecting circulating tumor cells: current challenges and new trends. *Theranostics, 3*(6), 377-394.

Hou, H. W., Bhagat, A. A. S., Lee, W. C., Huang, S., Han, J., & Lim, C. T. (2011). Microfluidic Devices for Blood Fractionation. *Micromachines, 2*(4), 319-343.

Hu, Y., Fan, L., Zheng, J., Cui, R., Liu, W., He, Y., Li, X., & Huang, S. (2010). Detection of circulating tumor cells in breast cancer patients utilizing multiparameter flow cytometry and assessment of the prognosis of patients in different CTCs levels. *Cytometry A, 77*(3), 213-219.

Huang, Amstislavskaya, T. G., Chen, G.-H., Chang, H.-H., Chen, Y.-H., & Jen, C.-P. (2012). Selectively concentrating cervical carconoma cells from rare blood cells utilizing dielectrophoresis with circular ITO electrodes in stepping electric fields. *Journal of Medical and Biological Engineering, 33*(1), 51-59.

Huang, C., Liu, H., Bander, N. H., & Kirby, B. J. (2013). Enrichment of prostate cancer cells from blood cells with a hybrid dielectrophoresis and immunocapture microfluidic system. *Biomed Microdevices, 15*(6), 941-948.

Husemann, Y., Geigl, J. B., Schubert, F., Musiani, P., Meyer, M., Burghart, E., Forni, G., Eils, R., Fehm, T., Riethmuller, G., & Klein, C. A. (2008). Systemic spread is an early step in breast cancer. *Cancer Cell, 13*(1), 58-68.

Ibrahim, S. N., Murray, L., Nock, V., Evans, J. J., & Alkaisi, M. M. (2012). The quadrupole microelectrode design on a multilayer biochip for dielectrophoretic trapping of single cells. *Microelectronic Engineering, 97*, 369-374.

Ikeda, I., Matsumaru, K., & Watarai, H. (2010, 19-23 Sept. 2010). *Dielectrophoresis of microparticles with planar and capillary quadrupole electrodes.* Paper presented at the World Automation Congress (WAC), 2010.

Iliescu, C., Xu, G., Barbarini, E., Avram, M., & Avram, A. (2008). Microfluidic device for continuous magnetophoretic separation of white blood cells. *Microsystem Technologies, 15*(8), 1157-1162.

Inglis, D. W., Riehn, R., Austin, R. H., & Sturm, J. C. (2004). Continuous microfluidic immunomagnetic cell separation. *Applied Physics Letters, 85*(21), 5093.

Issa, D., Albeldawi, M., Lopez, R., & Alkhouri, N. (2014). Hematocrit levels and red blood cell indices in patients with nonalcoholic fatty liver disease. *European Journal of Gastroenterology & Hepatology, 26*(3), 363-364.

Jin, McFaul, S., Duffy, S., Deng, X., Tavassoli, P., Black, P., & Ma, H. (2014). Technologies for label-free separation of circulating tumor cells: from historical foundations to recent developments. *Lab Chip, 14*(1), 32-44.

Jin, X., Chalmers, J. J., & Zborowski, M. (2012). Iron transport in cancer cell culture suspensions measured by cell magnetophoresis. *Anal Chem, 84*(10), 4520-4526.

Jones, T. B. (2003). Basic theory of dielectrophoresis and electrorotation. *IEEE Engineering in medicine and biology magazine*.

Joon, S. S., Michael, J. R., & Chong, H. A. (2013). A large area nano-gap interdigitated electrode array on a polymer substrate as a disposable nano-biosensor. *Journal of Micromechanics and Microengineering, 23*(3), 035002.

Jung, J., & Han, K.-H. (2008). Lateral-driven continuous magnetophoretic separation of blood cells. *Applied Physics Letters, 93*(22), 223902.

Juratli, M. A., Sarimollaoglu, M., Nedosekin, D. A., Melerzanov, A. V., Zharov, V. P., & Galanzha, E. I. (2014). Dynamic Fluctuation of Circulating Tumor Cells during Cancer Progression. *Cancers (Basel), 6*(1), 128-142.

Kadri, N. A. (2010). *Development of near real-time asessment system for cancer cells.* (Doctor of Philosophy), University of Surrey, U.K.

Kaler, K. V. I. S., Fritz, O. G., & Adamson, R. J. (1986). Quasi-Elastic Light Scattering Studies on Yeast Cells Undergoing Dielectrophoresis. *Industry Applications, IEEE Transactions on, IA-22*(1), 57-62.

Kamholz, A. E., & Yager, P. (2001). Theoretical Analysis of Molecular Diffusion in Pressure-Driven Laminar Flow in Microfluidic Channels. *Biophysical Journal, 80*(1), 155-160.

Kashevskii, B. E., Kashevskii, S. B., Prokhorov, I. V., Aleksandrova, E. N., & Istomin, Y. P. (2006). Magnetophoresis and the magnetic susceptibility of HeLa tumor cells. *Biophysics, 51*(6), 902-907.

Kawano, M., & Watarai, H. (2012). Brownian motion-magnetophoresis of nano/micro-particles. *Analyst, 137*(18), 4123-4126.

Khoo, B. L., Chaudhuri, P. K., Ramalingam, N., Tan, D. S., Lim, C. T., & Warkiani, M. E. (2016). Single-cell profiling approaches to probing tumor heterogeneity. *Int J Cancer*.

Khoshmanesh, K., Zhang, C., Tovar-Lopez, F. J., Nahavandi, S., Baratchi, S., Kalantar-zadeh, K., & Mitchell, A. (2009). Dielectrophoretic manipulation and separation of microparticles using curved microelectrodes. *Electrophoresis, 30*(21), 3707-3717.

Kin, C., Kidess, E., Poultsides, G. A., Visser, B., & Jeffrey, S. (2013). Colorectal cancer diagnostics: biomarkers, cell-free DNA, circulating tumor cells and defining heterogeneous populations ny single-cell analysis. *Expert Rev. Mol. Diagn, 13*(6), 581-599.

Kirby, B. J., Jodari, M., Loftus, M. S., Gakhar, G., Pratt, E. D., Chanel-Vos, C., Gleghorn, J. P., Santana, S. M., Liu, H., Smith, J. P., Navarro, V. N., Tagawa, S. T., Bander, N. H., Nanus, D. M., & Giannakakou, P. (2012). Functional Characterization of Circulating Tumor Cells with a Prostate-Cancer-Specific Microfluidic Device. *PLoS ONE, 7*(4), e35976.

Kortge, A., Elter, P., Lange, R., & Beck, U. (2013). Simulation of the Electric Field Distribution Near a Topographically Nanostructured Titanium-Electrolyte Interface: Influence of the Passivation Layer. *Journal of Nanomaterials, 2013*, 9.

Krawczyk, N., Banys, M., Hartkopf, A., Hagenbeck, C., Melcher, C., & Fehm, T. (2013). Circulating tumour cells in breast cancer. *Ecancermedicalscience, 7*, 352.

Krishnan, K. M. (2010). Biomedical nanomagnetics: a spin through possibilities in imaging, diagnostics, and therapy. *Magnetics, IEEE Transactions on, 46*(7), 2523-2558.

Kuczenski, R. S., Chang, H.-C., & Revzin, A. (2011). Dielectrophoretic microfluidic device for the continuous sorting of Escherichia coli from blood cells. *Biomicrofluidics, 5*(3), 032005-032005-032015.

Lee, A. M., Tormoen, G. W., Kanso, E., McCarty, O. J., & Newton, P. K. (2012). Modeling and simulation of procoagulant circulating tumor cells in flow. *Front Oncol, 2*, 108.

Leu, T.-S., & Liao, Z.-F. (2012). Separating Plasma and Blood Cells by Dielectrophoresis in Microfluidic Chips. *International Journal of Modern Physics: Conference Series, 19*, 185-189.

Levenberg, S., & Shemesh, J. (2014). Microfluidic device and method thereof: Google Patents.

Li, M., Li, W. H., Zhang, J., Alici, G., & Wen, W. (2014). A review of microfabrication techniques and dielectrophoretic microdevices for particle manipulation and separation. *Journal of Physics D: Applied Physics, 47*(6), 063001.

Liao, S. H., Chang, C. Y., & Chang, H. C. (2013). A capillary dielectrophoretic chip for real-time blood cell separation from a drop of whole blood. *Biomicrofluidics, 7*(2), 24110.

Lim, B., Reddy, V., Hu, X., Kim, K., Jadhav, M., Abedini-Nassab, R., Noh, Y.-W., Lim, Y. T., Yellen, B. B., & Kim, C. (2014). Magnetophoretic circuits for digital control of single particles and cells. *Nat Commun, 5*.

Lin Loo, J., Yee Woo, W., Wah Chin, M., Ru Yam, H., Kwang Ang, Y., & Seng Yim, H. (2013). Cancer Awareness of a Sample of Malaysian Undergraduate Students. *American Journal of Cancer Prevention, 1*(1), 9-13.

Liu, B., Li, D., Wang, Y., & Yang, J. (2009, 9-12 Aug. 2009). *The mathematical model and simulation for a micro electromagnetic relay.* Paper presented at the Mechatronics and Automation, 2009. ICMA 2009.

Lo, Y. J., Lin, Y. Y., Lei, U., Wu, M. S., & Yang, P. C. (2014). Measurement of the Clausius-Mossotti factor of generalized dielectrophoresis. *Applied Physics Letters, 104*(8), 083701.

Loutherback, K., D'Silva, J., Liu, L., Wu, A., Austin, R. H., & Sturm, J. C. (2012). Deterministic separation of cancer cells from blood at 10 mL/min. *AIP Adv, 2*(4), 42107.

Low, W. S., Kadri, N. A., & Wan Abas, W. A. B. b. (2014). Computational Fluid Dynamics Modelling of Microfluidic Channel for Dielectrophoretic BioMEMS Application. *The Scientific World Journal, 2014*, 11.

Lu, C.-T., Sue, W.-C., Wei, C.-H., Hsu, Y.-M., & Chen, X.-H. (2008, 18-21 Aug. 2008). *Dielectrophoretic Frequency Effect on Purification and Field Emission of Carbon Nanotubes.* Paper presented at the Nanotechnology, 2008. NANO '08. 8th IEEE Conference on.

Lustberg, M., Balasubramanian, P., Miller, B., Garcia-Villa, A., Deighan, C., Wu, Y., Berger, M., Carothers, S., & Shapiro, C. (2014). Heterogeneous atypical cell populations are present in blood of metastatic breast cancer patients. *Breast Cancer Research, 16*(23), 1-15.

Luzzi, K. J., Varghese, H. J., MacDonald, I. C., Schmidt, E. E., Kohn, E. C., Morris, V. L., Marshall, K. E., Chambers, A. F., & Groom, A. C. (1998). Inhibition of angiogenesis in liver metastases by carboxyamidotriazole (CAI). *Angiogenesis, 2*(4), 373-379.

Lynch, E. C. (1990). Peripheral Blood Smear. In H. K. Walker, W. D. Hall & J. W. Hurst (Eds.), *Clinical Methods: The History, Physical, and Laboratory Examinations*. Boston: Butterworths

Mario, U., & Elisabeth, S. (2008). The design of dielectrophoretic flow-through sorters using a figure of merit. *Journal of Micromechanics and Microengineering, 18*(1), 015001.

Marrinucci, D., Bethel, K., Bruce, R. H., Curry, D. N., Hsieh, B., Humphrey, M., Krivacic, R. T., Kroener, J., Kroener, L., Ladanyi, A., Lazarus, N. H., Nieva, J., & Kuhn, P. (2007). Case study of the morphologic variation of circulating tumor cells. *Hum Pathol, 38*(3), 514-519.

Maryam, F., Hassali, M. A., Knight, A., Shafie, A. A., Farooqui, M. A., & Saleem, F. (2013). A qualitative exploration of Malaysian cancer patients' perceptions of cancer screening. *BMC Public Health, 13*(48), 1-7.

Merrill, E. (1969). Rheology of blood. *Physiological Reviews, 49*, 863-890.

Michaelson, J. S., Cheongsiatmoy, J. A., Dewey, F., Silverstein, M. J., Sgroi, D., Smith, B., & Tanabe, K. K. (2005). Spread of human cancer cells occurs with probabilities indicative of a nongenetic mechanism. *Br J Cancer, 93*(11), 1244-1249.

Miller, M. C., Doyle, G. V., & Terstappen, L. W. M. M. (2010). Significance of Circulating Tumor Cells Detected by the CellSearch System in Patients with Metastatic Breast Colorectal and Prostate Cancer. *Journal of Oncology, 2010*, 1-8.

Miyakoshi, J. (2005). Effects of static magnetic fields at the cellular level. *Prog Biophys Mol Biol, 87*(2-3), 213-223.

Mocellin, S., Keilholz, U., Rossi, C. R., & Nitti, D. (2006). Circulating tumor cells: the 'leukemic phase' of solid cancers. *Trends in Molecular Medicine, 12*(3), 130-139.

Moon, H. S., Kwon, K., Kim, S. I., Han, H., Sohn, J., Lee, S., & Jung, H. I. (2011). Continuous separation of breast cancer cells from blood samples using multi-orifice flow fractionation (MOFF) and dielectrophoresis (DEP). *Lab Chip, 11*(6), 1118-1125.

Morales, F., Humberto, F., Enrique, D., & Joseph, S. (2008). Non uniform electric field induced yeast cell electrokinetic behavior. *Ingeneieria Investigacion, 28*(3), 116-121.

Mortensen, N. A., Okkels, F., & Bruus, H. (2005). Reexamination of Hagen-Poiseuille flow: Shape dependence of the hydraulic resistance in microchannels. *Physical Review E, 71*(5).

Mukhopadhyaya, S. (2005). Novel planar electromagnetic sensors: modeling and performance evaluation. *Sensors, 5*(12), 546-579.

Mulhall, H. J., Labeed, F. H., Kazmi, B., Costea, D. E., Hughes, M. P., & Lewis, M. P. (2011). Cancer, pre-cancer and normal oral cells distinguished by dielectrophoresis. *Anal Bioanal Chem, 401*(8), 2455-2463.

Orfao, A., Rodríguez, C., Adansa, J. C., Gómez-Alonso, A., Ramos, M., Cruz, J. J., Ciudad, J., & Cruz, I. (2005). Evaluation of Multiparameter Flow Cytometry for the Detection of Breast Cancer Tumor Cells in Blood Samples. *American Journal of Clinical Pathology, 123*(1), 66-74.

Paget, S. (1889). The distribution of secondary growths in cancer of the breast. *The Lancet, 133*(3421), 571-573.

Paguirigan, A. L., & Beebe, D. J. (2009). From the cellular perspective: exploring differences in the cellular baseline in macroscale and microfluidic cultures. *Integr Biol (Camb), 1*(2), 182-195.

Pamme, N. (2014). Continuous flow separations in microfluidic devices. *Lab Chip, 7*(12), 1644-1659.

Pamme, N., & Manz, A. (2004). On-chip free-flow magnetophoresis: continuous flow separation of magnetic particles and agglomerates. *Anal Chem, 76*(24), 7250-7256.

Park, Zhang, Y., Wang, H., & Yang, S. (2011). Continous dielectrophoretic bacterial separation and concentration from physiological media of high conductivity. *The Royal Society of Chemistry, 11*(17), 2893-2900.

Park, S., Ang, R. R., Duffy, S. P., Bazov, J., Chi, K. N., Black, P. C., & Ma, H. (2013). Morphological differences between circulating tumor cells from prostate cancer patients and cultuerd prostate cancer cells. *PLoS One, 9*(1), 1-7.

Park, S., Ang, R. R., Duffy, S. P., Bazov, J., Chi, K. N., Black, P. C., & Ma, H. (2014). Morphological differences between circulating tumor cells from prostate cancer patients and cultured prostate cancer cells. *PLoS One, 9*(1), e85264.

Pauline, J. C., Frank, W. C., Michelle, C. Y., Robert, O., & David, A. H. (2014). Force measurements of a magnetic micro actuator proposed for a microvalve array. *Journal of Micromechanics and Microengineering, 24*(3), 034005.

Pauling, L., & Coryell, C. D. (1936). The magnetic properties and structure of hemoglobin, oxyhemoglobin and carbonmonoxyhemoglobin. *Chemistry, 22*, 210-216.

Payen, D. (2003). *Biological cell separation using dielectrophoresis in a microfluidic device*. Bio and Thermal Engineering Laboratory. University of Carlifornia.

Peeters, F. M., & Jo, D. B. (2002). Hybrid magnetic-semiconductor nanostructures. In H. S. Nalwa (Ed.), *Nanostructured Materials and Nanotechnology* (pp. 247-328). California, USA: AcademicPress

Peng, Z. (2011). *Modeling of Particle and Biological Cell Transport in Microchannels.* (Master of Science), The Ohio State University.

Plouffe, B. D., Lewis, L. H., & Murthy, S. K. (2011). Computational design optimization for microfluidic magnetophoresis. *Biomicrofluidics, 5*, 13413.

Pohl, H. A., & Crane, J. S. (1971). Dielectrophoresis of Cells. *Journal of Biophysic, 11*(9), 711-727.

Pohl, H. A., & Hawk, I. (1966). Separation of living and dead cells by dielectrophoresis. *Science, 152*(3722), 647-649.

Pommer, M. S., Zhang, Y., Keerthi, N., Chen, D., Thomson, J. A., Meinhart, C. D., & Soh, H. T. (2008). Dielectrophoretic separation of platelets from diluted whole blood in microfluidic channels. *Electrophoresis, 29*(6), 1213-1218.

Porcher, P. (2005). Elemental Rare Earths: Magnetic Structure and Resistance, Correlation of. In K. H. J. Buschow (Ed.), *Concise Encyclopedia of Magnetic and Superconducting Materials* (pp. 156-164). UK: Elsevier

Pouyssegur, J., Dayan, F., & Mazure, N. M. (2006). Hypoxia signalling in cancer and approaches to enforce tumour regression. *Nature, 441*(7092), 437-443.

Pryor, R. W. (2011). *Multiphysics modeling using COMSOL: a first principles approach*. Boston: Jones and Bartlett Publishers.

Qian, C., Huang, H., Chen, L., Li, X., Ge, Z., Chen, T., Yang, Z., & Sun, L. (2014). Dielectrophoresis for Bioparticle Manipulation. *International Journal of Molecular Sciences, 15*(10), 18281-18309.

Qian, C., Huang, H., Chen, L., Li, X., Ge, Z., Chen, T., Yang, Z., & Sun, L. (2014). Dielectrophoresis for bioparticle manipulation. *Int J Mol Sci, 15*(10), 18281-18309.

Radisky, D. C. (2005). Epithelial-mesenchymal transition. *J Cell Sci, 118*(Pt 19), 4325-4326. doi: 10.1242/jcs.02552

Ramadan, Q., Poenar, D. P., & Yu, C. (2008). Customized trapping of magnetic particles. *Microfluidics and Nanofluidics, 6*(1), 53-62.

Saias, L., Autebert, J., Malaquin, L., & Viovy, J.-L. (2011). Design, modeling and characterization of microfluidic architectures for high flow rate, small footprint microfluidic systems. *Lab on a Chip, 11*(5), 822.

Saliterman, S. S. (2006). *Fundamentals of BioMEMS and Medical Microdevices*. USA: Wiley Interscience.

Schwan, H. P. (1957). Electrical properties of tissue and cell suspensions. *Adv Biol Med Phys, 5*, 147-209.

Shen, F., Hwang, H., Hahn, Y. K., & Park, J.-K. (2012). Label-Free Cell Separation Using a Tunable Magnetophoretic Repulsion Force. *Analytical Chemistry, 84*(7), 3075-3081.

Shim, S., Gascoyne, P., Noshari, J., & Hale, K. S. (2011). Dynamic physical properties of dissociated tumor cells revealed by dielectrophoretic field-flow fractionation. *Integr Biol (Camb), 3*(8), 850-862.

Shim, S., Stemke-Hale, K., Tsimberidou, A. M., Noshari, J., Anderson, T. E., & Gascoyne, P. R. C. (2013). Antibody-independent isolation of circulating tumor cells by continuous-flow dielectrophoresis. *Biomicrofluidics, 7*(1), 011807.

Siegel, A. C., Shevkoplyas, S. S., Weibel, D. B., Bruzewicz, D. A., Martinez, A. W., & Whitesides, G. M. (2006). Cofabrication of electromagnets and microfluidic systems in poly(dimethylsiloxane). *Angew Chem Int Ed Engl, 45*(41), 6877-6882.

Sleijfer, S., Gratama, J. W., Sieuwerts, A. M., Kraan, J., Martens, J. W., & Foekens, J. A. (2007). Circulating tumour cell detection on its way to routine diagnostic implementation? *Eur J Cancer, 43*(18), 2645-2650.

Song, S.-H., Kwak, B.-S., & Jung, H.-I. (2009). Analysis and utilization of Joule heating in an electromagnet integrated microfluidic device for biological applications. *Current Applied Physics, 9*(4, Supplement), e287-e290.

Sun, J., Liu, C., Li, M., Wang, J., Xianyu, Y., Hu, G., & Jiang, X. (2013). Size-based hydrodynamic rare tumor cell separation in curved microfluidic channels. *Biomicrofluidics, 7*(1), 11802.

Tabatabaian, M. (2014). *COMSOL for Engineers*. New Delhi: Mercury Learning and Information.

Takagi, J., Yamada, M., Yasuda, M., & Seki, M. (2005). Continuous particle separation in a microchannel having asymmetrically arranged multiple branches. *Lab Chip, 5*(7), 778-784.

Takaori, M. (1966). Changes of pH of Blood Diluted with Plasma and Plasma Substitutes in Vitro. *Transfusion, 6*(6), 597-599.

Takayasu, M., Kelland, D. R., & Minervini, J. V. (2000). Continuous magnetic separation of blood components from whole blood. *Applied Superconductivity, IEEE Transactions on, 10*(1), 927-930.

The Kuhn Lab. (2014). *Circulating tumor cells (CTCs) for cancer diagnosis and prognosis*. La Jolla, CA.

Thiery, J. P. (2002). Epithelial-mesenchymal transitions in tumour progression. *Nat Rev Cancer, 2*(6), 442-454.

Tibbe, A. G., Miller, M. C., & Terstappen, L. W. (2007). Statistical considerations for enumeration of circulating tumor cells. *Cytometry A, 71*(3), 154-162.

Toner, M., & Irimia, D. (2005). Blood-on-a-chip. *Annu Rev Biomed Eng, 7*, 77-103.

Toner, M., & Irimia, D. (2008). Blood-on-a-chip. *Annual Reviews Biomeical Engineer, 7*, 77-103.

Varshney, M., & Li, Y. (2009). Interdigitated array microelectrodes based impedance biosensors for detection of bacterial cells. *Biosensors and Bioelectronics, 24*(10), 2951-2960.

Visser, K. R. (1989, 9-12 Nov 1989). *Electric conductivity of stationary and flowing human blood at low frequencies.* Paper presented at the Engineering in Medicine and Biology Society, 1989. Images of the Twenty-First Century., Proceedings of the Annual International Conference of the IEEE Engineering in.

Voldman, J., Toner, M., Gray, M. L., & Schmidt, M. A. (2003). Design and analysis of extruded quadrupolar dielectrophoretic traps. *Journal of Electrostatics, 57*(1), 69-90.

Vykoukal, D. M., Gascoyne, P. R., & Vykoukal, J. (2009). Dielectric characterization of complete mononuclear and polymorphonuclear blood cell subpopulations for label-free discrimination. *Integr Biol (Camb), 1*(7), 477-484.

Wang, Flanagan, L. A., Monuki, E., Jeon, N. L., & Lee, A. P. (2007). Dielectrophoresis switching with vertical sidewall electrodes for microfluidic flow cytometry. *Lab Chip, 7*(9), 1114-1120.

Wang, Huang, Y., Wang, X., Becker, F. F., & Gascoyne, P. R. (1997). Dielectrophoretic manipulation of cells with spiral electrodes. *Biophys J, 72*(4), 1887-1899.

Wang, Zheng, G., Cheng, B., Chen, F., Wang, Z., Chen, Y., Wang, Y., & Xiong, B. (2014). Circulating Tumor Cells (CTCs) detected by RT-PCR and its prognostic role in gastric cancer: a meta-analysis of published literature. *PLoS One, 9*(6), e99259.

Wang, L., Flanagan, L. A., Jeon, N. L., Monuki, E., & Lee, A. P. (2007). Dielectrophoresis switching with vertical sidewall electrodes for microfluidic flow cytometry. *Lab on a Chip, 7*(9), 1114-1120.

Wang, L. H., Lawrence, S. M., Navas, T., & Kinderss, R. J. (2014). *Characterization of CTCs from peripheral blood specimens of patients (using ApoSteam Instruments).* Paper presented at the American Society of Clinical Oncolgy Annual Meeting 2014, Chicago, United States.

Wang, Z., Wang, J., Yue, T., Yuan, Y., Cai, R., & Niu, C. (2013). Immunomagnetic Separation Combined with Polymerase Chain Reaction for the Detection of Alicyclobacillus acidoterrestris in Apple Juice. *PLoS ONE, 8*(12), e82376.

Warkiani, M. E., Guan, G., Luan, K. B., Lee, W. C., Bhagat, A. A. S., Kant Chaudhuri, P., Tan, D. S.-W., Lim, W. T., Lee, S. C., Chen, P. C. Y., Lim, C. T., & Han, J. (2014). Slanted spiral microfluidics for the ultra-fast, label-free isolation of circulating tumor cells. *Lab on a Chip, 14*(1), 128-137.

Yafouz, B., Kadri, N. A., Rothan, H. A., Yusof, R., & Ibrahim, F. (2016). Discriminating dengue-infected hepatic cells (WRL-68) using dielectrophoresis. *ELECTROPHORESIS, 37*(3), 511-518.

Yang, J., Huang, Y., Wang, X. B., Becker, F. F., & Gascoyne, P. R. (2000). Differential analysis of human leukocytes by dielectrophoretic field-flow-fractionation. *Biophysical Journal, 78*(5), 2680-2689.

Yavuz, C. T., Mayo, J., William, W. Y., Prakash, A., Falkner, J. C., Yean, S., Cong, L., Shipley, H. J., Kan, A., & Tomson, M. (2006). Low-field magnetic separation of monodisperse Fe3O4 nanocrystals. *Science, 314*(5801), 964-967.

Ying, L., & Wang, Q. (2013). Microfluidic chip-based technologies: emerging platforms for cancer diagnosis. *BMC Biotechnology, 13*(76).

Zabaglo, L., Ormerod, M. G., Parton, M., Ring, A., Smith, I. E., & Dowsett, M. (2003). Cell filtration-laser scanning cytometry for the characterisation of circulating breast cancer cells. *Cytometry A, 55*(2), 102-108.

Zborowski, M. (2008). Maxwell stress and magnetic force. In M. Zborowski & J. J. Chalmers (Eds.), *Magnetic Cell Separation* (pp. 62-78). Netherlands: Elsevier

Zborowski, M., Moore, L. R., Williams, P. S., & Chalmers, J. J. (2002). Separations Based on Magnetophoretic Mobility. *Separation Science and Technology, 37*(16), 3611-3633.

Zborowski, M., Ostera, G. R., Moore, L. R., Milliron, S., Chalmers, J. J., & Schechter, A. N. (2003). Red blood cell magnetophoresis. *Biophys J, 84*(4), 2638-2645.

Zhang, Bottausci, F., Rao, M., Parker, E., Mezic, I., & Macdonald, N. (2008). Titanium-based dielectrophoresis devices for microfluidic applications. *Biomed Microdevices, 10*(4), 509-517.

Zhang, X., Chen, Z., & Huang, Y. (2015). A valve-less microfluidic peristaltic pumping method. *Biomicrofluidics, 9*(1), 014118.

Zhang, Y., Li, J., Cao, L., Xu, W., & Yin, Z. (2012). Circulating tumor cells in hepatocellular carcinoma: detection techniques, clinical implications, and future perspectives. *Semin Oncol, 39*(4), 449-460. doi: 10.1053/j.seminoncol.2012.05.012

Zheng, S., Lin, H. K., Lu, B., Williams, A., Datar, R., Cote, R. J., & Tai, Y. C. (2011). 3D microfilter device for viable circulating tumor cell (CTC) enrichment from blood. *Biomed Microdevices, 13*(1), 203-213.

Zhu, G.-P., Hejiazan, M., Huang, X., & Nguyen, N.-T. (2014). Magnetophoresis of diamagnetic microparticles in a weak magnetic field. *Lab on a Chip, 14*(24), 4609-4615.

LIST OF PUBLICATIONS AND PAPER PRESENTED

Low, W. S., Kadri, N. A., & Wan Abas, W. A. B. b. (2014). Computational Fluid Dynamics Modelling of Microfluidic Channel for Dielectrophoretic BioMEMS Application. *The Scientific World Journal, 2014*, 11.

Low, W.S., & Kadri, N.A. (2014, May). *Design and Simulation of Integrated Dielectrophoretic/Magnetophoretic device for cancer cells separation from blood*. Poster presented at Biosensor Conference 2014. Australia.

Low, W.S., & Kadri, N.A. (2016, March). *Numerical analysis of integrated magnetophoresis/dielectrophoresis device for separation of CTC from blood*. Paper presented at International Postgraduate Research Award Seminar 2016, University Malaya, Malaysia.